

***Fatigue Crack Growth of Carbon Steel
in Gaseous Hydrogen
– An Updated Tri-Linear Predictive Model***

Ning Zhang

Student number: 6073603

Program: M. Sc. Offshore and Dredging Engineering



Abstract

Hydrogen infrastructure will play a critical role in meeting the future demand for decarbonization. Existing pipelines can be potentially repurposed, and new pipelines will be installed to transport hydrogen gas. Pipelines, especially offshore pipelines, are subjected to cyclic loading which can lead to potential fatigue damage and failure. The fatigue resistance of steel deteriorates under prolonged exposure to pressurized hydrogen due to the hydrogen embrittlement effect.

Hydrogen assisted fatigue crack growth rate (HA-FCGR) is investigated in this study. The influences of various test parameters including hydrogen gas pressure, cyclic load ratio and frequency, test temperature, and the yield strength of the steel are reviewed and analyzed. Existing models to predict the HA-FCGR are also assessed.

An updated Tri-Linear model is proposed to predict the HA-FCGR of carbon steel. The key values associated with the two knee points, which define the shape of the HA-FCGR curve, are expressed as functions of the test parameters and the yield strength of the steel. Fatigue test results digitized from existing literature are utilized to optimize the experimental constants required for the Tri-Linear model. The modeled HA-FCGR curves are compared against experimental data to demonstrate the agreement with the test results.

The updated Tri-Linear model directly correlates the hydrogen gas pressure, cyclic load ratio and frequency, test temperature, and the yield strength of the steel to the predicted HA-FCGR. Facilitated by the strong correlations, the number of experiments required to qualify the pipeline steel under the design and operating conditions can be reduced.

Keywords: hydrogen assisted, fatigue crack growth rate, carbon steel, Tri-Linear, knee points, predictive model, test parameters, hydrogen embrittlement, fracture mechanisms

Acknowledgement

It may sound strange, but I thank myself for persevering, no matter how difficult the journey has been. I am grateful to my parents and my loyal companion, Doggy the little mutt, for keeping me grounded.

I deeply appreciate Dr. Carey Walters for generously contributing his time and attention to my project. Dr. Casper Versteyleen and Marije Deul from TNO provided me with invaluable guidance and support throughout this process, for which I am truly thankful. I also thank Dr. Vera Popovich, Dr. Poulumi Dey and Aswin Suresh for taking the time to review my work and for their thoughtful evaluation.

Many thanks to my dear friend Connor, who has consistently been a flashlight to me.

Now, time to cram even more experiences into life.

Contents

1	Introduction.....	12
1.1	Deleterious effect of hydrogen	13
1.2	Expected operating conditions	13
1.3	Motivation	13
1.4	Objective and method	14
1.5	Scope.....	15
2	Background: hydrogen embrittlement.....	16
3	Predictive models	18
3.1	Theoretical EAC model	18
3.2	Phenomenological HA-FCGR model and its application	19
3.2.1	HA-FCGR model.....	20
3.2.2	ASME B31.12 application	24
3.3	Comparison of the EAC model and HA-FCGR model.....	25
3.4	Complementary models	27
3.4.1	Numerical.....	28
3.4.2	Analytical	30
3.4.3	Summary.....	39
3.5	Conclusion.....	39
4	Influencing variables	40
4.1	HE.....	40
4.2	HA-FCG.....	43
4.2.1	Introduction.....	43
4.2.2	Pressure	46
4.2.3	Load frequency	49
4.2.4	Pressure joint with load frequency	52
4.2.5	Temperature	53
4.2.6	Strength.....	55
4.2.7	Microstructure	56

4.2.8	Load ratio R	56
4.2.9	Test method	57
4.2.10	Summary.....	57
4.3	Key threshold values	59
5	A Tri-Linear HA-FCGR model	63
5.1	Handling units.....	63
5.2	A Tri-Linear format.....	64
5.3	Curve fitting to experimental results	65
6	Fracture Mechanisms.....	74
6.1	Region A	74
6.2	Region B	75
6.3	Region C.....	77
6.4	Summary.....	79
7	Onset of hydrogen enhancement	80
7.1	The mechanism of fracture behind ΔK_1	80
7.2	ΔK_1 and K_{TH2}	81
7.3	Verification of EAC model	82
7.3.1	Complete EAC model	82
7.3.2	Curve fitting and verification of the EAC model	83
7.3.3	Summary.....	85
7.4	Quantification of K_{TH2}	85
7.5	Predicted ΔK_1	90
7.6	Discussion.....	92
8	ΔK_2 at hydrogen enhancement saturation	94
8.1	Fracture mechanisms.....	94
8.2	Dislocation velocity affected by hydrogen	94
8.3	Hydrogen-restricted dislocation zone	96
8.4	Predictive model of ΔK_2	99
8.5	Predicted ΔK_2	104

8.6	Discussion.....	104
9	HA-FCGR at hydrogen enhancement saturation	107
9.1	Relation to FPZ and $\Delta\delta_2$	107
9.2	Mechanistic theory.....	109
9.3	Predictive model of $(\frac{da}{dN})_2$	111
9.4	Predicted $(\frac{da}{dN})_2$	113
9.5	Discussion.....	113
10	An updated Tri-Linear predictive model	115
11	Hypotheses of the frequency effect.....	121
11.1	Frequency effect on ΔK_1	121
11.2	Frequency effect on ΔK_2	122
11.3	Frequency effect on $(\frac{da}{dN})_2$	123
11.4	Summary.....	123
12	Conclusion and recommendation.....	125

Glossary:

AIDE: adsorption induced dislocation emission

EAC: environmentally assisted cracking

FCG: fatigue crack growth

FCGR: fatigue crack growth rate

FPZ: fatigue process zone

HA-FCG: hydrogen assisted fatigue crack growth

HA-FCGR: hydrogen assisted fatigue crack growth rate

HE: hydrogen embrittlement

HEDE: hydrogen-enhanced decohesion

HEE: hydrogen environment embrittlement

HEFCG: hydrogen enhanced fatigue crack growth

HELP: hydrogen enhanced localized plasticity

H-RDZ: hydrogen-restricted dislocation zone

IHE: internal hydrogen embrittlement

Nomenclature:

The nomenclature includes only terms directly related to the proposed model, omitting those discussed in Chapter 3.4 and Chapter 4 for context to maintain clarity and focus.

$\frac{da}{dN}$: FCGR per cycle, *mm/cycle*

$\left(\frac{da}{dN}\right)_1$: HA-FCGR at the lower knee point, *mm/cycle*

$\left(\frac{da}{dN}\right)_2$: HA-FCGR at the upper knee point, *mm/cycle*

$\left(\frac{da}{dN}\right)_{aggressive}$: corrosion FCGR, *mm/cycle*

$\left(\frac{da}{dN}\right)_{air}$: FCGR for the material in air, *mm/cycle*

$\left(\frac{d\bar{a}}{dt}\right)_{EAC}$: average environmental crack growth rate over a loading cycle, *mm/cycle*

$\left(\frac{da}{dt}\right)_{EAC}$: environmental crack growth rate over a loading cycle, *mm/cycle*.

$\left(\frac{da}{dN}\right)_H$: HA-FCGR assisted by hydrogen, *mm/cycle*

$\left(\frac{da}{dN}\right)_{inert}$: crack growth per cycle due to fatigue of the material in an inert environment, *mm/cycle*

$\left(\frac{da}{dN}\right)_{PH}$: HA- FCGR dominated by stress enhanced hydrogen accumulation within the FPZ, *mm/cycle*

$\left(\frac{da}{dN}\right)_{TP}$: FCGR at the pivot point, *mm/cycle*

$\left(\frac{da}{dN}\right)_{tr}$: $\frac{da}{dN}$ corresponding to ΔK_{tr} , *mm/cycle*

$\left(\frac{da}{dN}\right)_{Total}$: total FCGR, *mm/cycle*

$\left(\frac{da}{dN}\right)_{\Delta K}$: HA- FCGR dominated by crack tip deformation, *mm/cycle*

$\left(\frac{da}{dN}\right)_{data_i}$: the i^{th} observed crack growth rate in the fatigue test, *mm/cycle*

$\left(\frac{da}{dN}\right)_{model_i}$: the i^{th} modeled crack growth rate, *mm/cycle*

$\frac{da}{dt}$: crack growth per unit time, *mm/s*

ΔK : range of stress intensity, *MPa \sqrt{m}*

ΔK_0 : initiation threshold stress intensity range, *MPa \sqrt{m}*

ΔK_1 : stress intensity range at lower knee point, *MPa \sqrt{m}*

ΔK_2 : stress intensity range at upper knee point, *MPa \sqrt{m}*

ΔK_{max}^T : lower threshold stress intensity range, *MPa \sqrt{m}*

ΔK_{TP} : stress intensity range at the pivot point, *MPa \sqrt{m}*

ΔK_{tr} : upper threshold stress intensity range, $MPa\sqrt{m}$
 A_{EAC} , B_{EAC} and C_{EAC} : fitted constants,
 B_{air} : exponent of FCGR in air
 C_{11} : fitted constant, $9.4235199 \times 10^{-8}m$
 C_{12} : fitted constant, $776.99309 MPa$
 C_{21} : fitted constant, 1.9723103×10^{-1}
 C_{22} : fitted constant, $10.931076 MPa\sqrt{m}$
 C_{31} : fitted constant, 0.08065590
 C_{32} : fitted constant, 278766.00
 C_s : concentration of hydrogen at the crack surface, $1/m^2$
 D : inclusion spacing, mm
 D_a : dilatation amplification factor
 D_H : hydrogen diffusivity coefficient, m^2/s
 E : Young's modulus, GPa
 ER : total residual error of the Nonlinear Least Square optimization
 E_b : binding energy of a trap site, $47 kJ/mol$,
 F : geometric parameter
 F_u : fugacity, MPa
 G_c : fracture toughness, GPa
 G_{IC} : strain energy release rate, J/m^2
 G_s : shear modulus, GPa
 H_D : activation energy for the diffusion of hydrogen into α -iron, $27000 J/mol$
 K : stress intensity factor, $MPa\sqrt{m}$
 K_I : stress intensity for Mode I loading, $MPa\sqrt{m}$
 K_{IEAC} : static loading threshold stress intensity for environmental cracking, $MPa\sqrt{m}$
 K_{ISCC} : apparent threshold stress intensity for stress corrosion cracking, $MPa\sqrt{m}$
 K_{max}^T : threshold stress intensity, $MPa\sqrt{m}$
 K_{max} : maximum applied stress intensity, $MPa\sqrt{m}$
 K_{min} : minimum applied stress intensity, $MPa\sqrt{m}$
 K_r : reference stress intensity, $MPa\sqrt{m}$
 K_{TH2} : threshold stress intensity for hydrogen induced crack growth, $MPa\sqrt{m}$
 MAE : mean absolute error of the model
 N_{data} : number of data points in the fatigue test results

P_H : hydrogen pressure, *MPa*
 $P_{H_{th}}$: threshold hydrogen pressure, 0.02 *MPa*
 P_{max} : maximum internal pressure, *MPa*
 P_{min} : minimum internal pressure, *MPa*
 P_{re} : reference hydrogen pressure, 0.7 *MPa*
 Q : activation energy for hydrogen diffusion, 2.71×10^{-4} *MJ/mol*
 Q_f : crack shape specific function
 R : cyclic load ratio
 R_0 : original void size, *m*
 R_{av} : average inclusion size, *m*
 R_g : universal gas constant, 8.314×10^{-6} *MJ/(mol·K)*
 R_I : inclusion radius, *m*
 R_V : void radius, *m*
 \dot{R}_0 : average radial velocity on the void boundary, *m/s*
 T : absolute temperature, *K*
 T_{period} : period of one cycle, *s*
 V : partial molar volume of hydrogen, 2.0×10^{-6} *m³/mol*
 X_0 : average inclusion spacing, *mm*
 a : crack depth, *m*
 a_{air} : multiplier of FCGR in air
 aH, BH, mH, dH, aK and BK : fitted parameters
 $a1, a2, a3, b1, b2$ and $b3$: constants
 a_{EAC} and b_{EAC} : fitted constants
 b_{AN} : Abel-Noble parameter, 1.584×10^{-5} *m³/mol*
 b_v : Burger's vector
 c : half length of the crack where it intersects the surface, *m*
 d : critical distance in front of the crack tip, *m*
 d_i : inclusion diameter, *m*
 d_0 : hole size, *m*
 e_D : experimentally determined material constant
 f : loading frequency, *Hz*
 l_0 : the ligament height, *m*
 m_{Schmid} : Schmid factor
 n_i : exponent of multi-linear Paris' relation

r_H : characteristic length of H-RDZ, m
 r_p : size of the FPZ, m
 r_y : plastic zone size, m
 t : time, s
 t_H : hydrogen diffusion period, s
 t_w : wall thickness, m
 v_0 : dislocation velocity at stress τ_0 , m/s
 v_D : dislocation velocity, m/s
 α_T : constant
 δ : crack tip opening displacement, mm
 δ_H : Heaviside function
 δ_{IC} : critical crack tip opening displacement, mm
 δ_i : crack tip opening displacement at initiation, mm
 $\Delta\delta$: crack tip opening displacement range, mm
 ν : Poisson ratio
 ξ : ratio of the crack depth over the wall thickness
 ρ : average radius of the vessel or pipe, m
 ρ_d : dislocation density, $1/m^3$
 σ_0 : yield stress, MPa
 σ_y : yield strength of the material, MPa
 σ_{y_local} : local yield strength of the steel within H-RDZ, MPa
 σ_∞ : mean normal stress, MPa
 σ_h : hydrostatic stress at a critical distance $6r_p$ in front of the crack tip, MPa
 τ : applied shear stress, MPa
 τ_0 : experimentally determined material constant, MPa
 τ_i : intrinsic strength of a material independent of dislocation interactions, MPa
 θ_L : lattice site occupancy of hydrogen
 θ_x : trap site occupancy of hydrogen
 θ_{xm} : modified trap site occupancy of hydrogen
 ϕ : acceleration factor
 $\dot{\epsilon}$: strain rate, $1/s$

1 Introduction

The historic Paris Agreement in 2015 set long-term goals to substantially reduce global greenhouse gas emissions to hold global temperature increase to well below 2°C above pre-industrial levels and pursue efforts to limit it to 1.5°C above pre-industrial levels, recognizing that this would significantly reduce the risks and impacts of climate change. Presently, the demand is high to shift towards environment-friendly fuel consumption. Hydrogen, with its versatility, has the potential to decarbonize multiple industries in multiple ways. High pressure hydrogen can be used to power heavy transport. Natural gas can be replaced by hydrogen for heating. Hydrogen can also be a key part of the process of methanol and ammonia production. All these applications of hydrogen lead to reduction of carbon emission. Hydrogen is broadly regarded as the energy carrier of the future, and its widespread use is expected to support economies' efforts to decarbonize.

Hydrogen is an efficient energy carrier, and the losses created in transmitting energy as gaseous hydrogen through pipelines are incomparably less than those in transmitting energy as electricity [1]. An extensive network of natural gas pipelines are safely and efficiently delivering natural gas from the collection fields to the refineries then to millions of homes. One possible means to rapidly expand the hydrogen delivery infrastructure is to adapt the existing natural gas pipelines to accommodate hydrogen transportation. The comprehensive European Hydrogen Backbone initiative aims to accelerate Europe's decarbonization journey by defining the critical role of hydrogen infrastructure – based on existing and new pipelines – in enabling the development of a competitive and pan-European renewable and low-carbon hydrogen market. Below map of European gas pipeline network in Figure 1 demonstrates the extensive existing natural gas pipelines in Europe that can be potentially re-purposed to transport hydrogen.

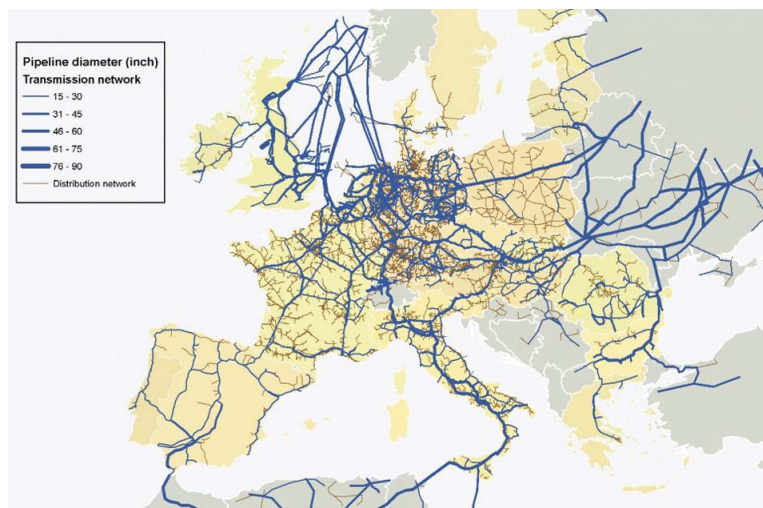


Figure 1 European gas pipeline network [2]

1.1 Deleterious effect of hydrogen

The damaging effect of hydrogen in iron and steel was first recognized in the early 1870s. Since then, there have been intensive efforts to characterize and understand Hydrogen Embrittlement (HE) [3] of steel which refers to the phenomenon in which the mechanical properties of the steel deteriorate due to the presence of atomic hydrogen in the steel. Fatigue resistance of steel also deteriorates under extended exposure to pressurized hydrogen, due to the HE effect. Pipelines, especially offshore pipelines, are subjected to pressure and temperature fluctuation, internal equipment, flow and external load induced vibration, and operational variation. The repeated or fluctuating stress that occurs over time causes cyclic loading on the pipeline steel. The cyclic loading leads to potential fatigue damage and failure.

1.2 Expected operating conditions

Currently, a typical operating condition for hydrogen transmission and distribution pipelines is not fully established. Natural gas transmission pipeline system can be operated up to a pressure of 15.2 MPa [4] and temperature of 50°C. The volumetric energy density of hydrogen is about one third that of natural gas at standard conditions. There is therefore a general consensus that the hydrogen economy needs higher pressure hence higher temperature hydrogen to be viable.

For onshore natural gas pipelines, the frequency of the cyclic load during operation can be as low as 10^{-5} Hz [5]. For offshore natural gas pipelines, the frequency of the prevalent cyclic load due to vortex induced vibration can be calculated as $Str \cdot U/Dia$, with Str , U and Dia being the Strouhal Number, flow velocity, and pipe outside diameter. Strouhal Number is approximately 0.2 for a subcritical flow [6]. Assuming a flow velocity of 2 m/s, and pipe outside diameter of 0.168 m, the vortex induced vibration frequency equals 2.38 Hz.

The existing natural gas pipeline operating conditions can be viewed as a reference benchmark for future hydrogen pipeline operating conditions, making them key factors to guide this research work.

1.3 Motivation

Extensive experiments were carried out by scientists to investigate the fatigue response of steel in hydrogen. Multiple numerical and analytical models were proposed to predict the fatigue crack growth assisted by the presence of hydrogen as a function of material properties and test parameters. Such models are reviewed in Chapter 3 Predictive models of this document. Calibrations to the experimental data are usually required to complete the models.

A phenomenological model is presented by Amaro et al. [7] to predict the fatigue crack growth of pipeline steel in pressurized gaseous hydrogen. ASME B31.12 2023 Hydrogen Piping and Pipelines [8] utilizes an upper-bound simplification of this model, which leads to the safest course of action, for performance-based fatigue design. This generalized approach is preferred for a design code; however, this typically results in designs that are less economical due to the increased material usage and over-engineering required to mitigate all potential risks.

The phenomenological model [7], however, includes eight empirical parameters that require calibrations to fatigue test results. Fitted parameters are commonly seen included in the predictive models. Minimizing the number of empirical parameters in a predictive model offers significant potential benefits. By reducing the number of parameters that require calibration through testing, the number of required experiments can be reduced, because the results from the experiments can be accurately correlated to the desired design or operating conditions. There is a clear opportunity to refine a predictive model with the aim of maintaining the necessary accuracy while reducing complexity and testing requirements, subsequently to enhance the efficacy of the model predicting the fatigue life of the steel of interest.

Furthermore, for practical reasons, fatigue tests are mostly performed under cyclic loading with a relatively high frequency, that is 1 Hz or above. The frequency of the cyclic load due to pressure or temperature variation during operation can be as low as 10^{-5} Hz. If the frequency of the cyclic load can be effectively incorporated into one or more of the empirical parameters, the response obtained from a fatigue test conducted in a laboratory under a relatively high frequency can be subsequently converted to a predicted fatigue response under the forecasted frequency of the cyclic load given the pipeline operating conditions. Accurately and effectively bridging the gap between the practical cyclic load frequency applied in a laboratorial environment, and the actual frequency of the cyclic load that pipelines undergo, is of great interest among researchers and the commercial energy sectors.

This balance between safety, efficiency, and cost-effectiveness is crucial in industrial applications. Refining a predictive model to achieve this balance could represent a significant advancement in the field of engineering practice, providing engineers with an efficient tool to accurately predict material behavior while optimizing the cost-effectiveness of the design.

1.4 Objective and method

The findings of this work aim to facilitate the design and qualification of new pipelines for transporting pure hydrogen gas or a mixture of natural gas and hydrogen, as well as the repurposing of existing natural gas pipelines for hydrogen gas transport.

This study investigates a collection of available test results from literature to determine the influence of various test parameters on the fatigue crack growth (FCG) response of carbon steel exposed to pressurized gaseous hydrogen. First principle based formulations can be then proposed to represent the empirical parameters included in the fatigue crack growth rate (FCGR) predictive models as functions of test parameters. The modified models with reduced number of empirical parameters can be evaluated to establish the level of accuracy and efficacy. The objective of this work is to present a refined FCGR predictive model with reduced quantity of empirical parameters by incorporating test parameters.

1.5 Scope

Carbon steel is the most common type of steel used in pipelines. The primary attention of this work is given to carbon steel specimens tested in pressurized hydrogen gas. Tests involving specimens pre-charged by the means of immersion charging or electrochemical charging, subsequently fatigue tested in air, are included but differentiated from the in-situ gaseous hydrogen tests.

2 Background: hydrogen embrittlement

Lynch [3] classified HE into two categories, namely Internal Hydrogen Embrittlement (IHE) and Hydrogen Environment Embrittlement (HEE) based on the source of the hydrogen. The primary sources of hydrogen leading to IHE are the solutions used to clean and apply protective coatings, whereas pressurized gaseous (or liquid) hydrogen in energy transportation is the main cause of HEE. This study aims to investigate the FCG behavior of carbon steel in a hydrogen environment, with a particular focus on the phenomenon of HEE.

The microstructures of steels vary significantly, but there is substantial evidence to suggest that carbon steels for commercial pipelines regardless of the microstructures are susceptible to HE [3]. Hydrogen atoms are small compared with metallic atoms. As a result, hydrogen atoms can fit within the interstitial sites in a metallic crystal and at grain boundaries, then readily diffuse through metals even at room temperature [9]. HE caused by gaseous hydrogen initially requires the physical adsorption of hydrogen gas, in which the hydrogen molecule dissociates in order to assume the energetically more favorable state at sliding stages or surface defects. The atomically present hydrogen can then be absorbed by the steel at the surface [10]. Figure 2 illustrates the mechanism.

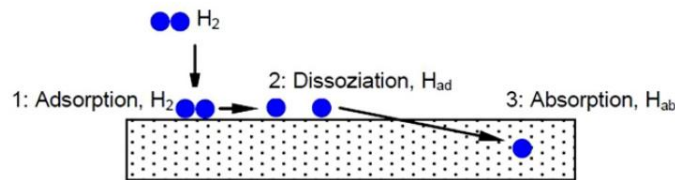


Figure 2 Mechanism of absorption of hydrogen via the gas phase[10]

Subsequently, the formation of atomic hydrogen on the surface is followed by the stress-assisted hydrogen diffusion to the region of high triaxial stresses, such as the stress field immediately in front of a crack tip [11]. This phenomenon is contributed to the high degree of stress triaxiality near the crack tip causing the crystal lattices to expand, which subsequently raises hydrogen solubility locally [9].

The mechanisms of HE summarized by Lynch [3] below are widely accepted and adopted.

1. **Hydrogen-Enhanced Decohesion (HEDE)** is a decohesion theory that postulates hydrogen reduces the cohesive strength of the lattice, so that bonds rupture at lower applied stresses [12]. Oriani and Josephic [13] developed the hypothesis that the chemical potential of dissolved hydrogen is lowered due to the higher elastic stresses at crack fronts. The dissolved hydrogen subsequently attains higher concentration than the equilibrium hydrogen concentration given

ambient hydrogen fugacity. The high hydrogen accumulation at the crack tip lowers the maximum resistive cohesive force between the atoms so that the applied tensile stress can equal to the maximum lattice cohesive force.

2. **Hydrogen-Enhanced Localized Plasticity (HELP)** is a theory that proposes localized deformation at a crack tip is due to dislocation activity facilitated by solute hydrogen. It is once again believed that the concentration of hydrogen is localized near crack tips due to hydrostatic stresses or entry of hydrogen at crack tips. A more localized micro-void coalescence process in turn induces subcritical crack growth. Hydrogen diffusion to local regions ahead of crack tips is required. Depending on whether high hydrogen concentration is localized within grain interiors or adjacent to grain boundaries, the crack path can be trans-granular or inter-granular [3].
3. The **Adsorption-Induced Dislocation Emission (AIDE)** mechanism suggests that the nucleation of a dislocation is facilitated by the hydrogen adsorption at crack tips. Once nucleated, the dislocations move rapidly away from the crack tip under applied stress. The nucleation stage is facilitated by the weakening of interatomic bonds over several atomic distances by the adsorbed hydrogen. Crack growth primarily is contributed to dislocation emission from crack tips.

AIDE is more complex than HEDE and HELP. The occurrence of combinations of AIDE, HELP, and HEDE mechanisms depends on the material, microstructure, environment, temperature, stress-intensity factor, and other variables. For example, when the crack growth is predominantly promoted by AIDE, void nucleation ahead of cracks could be promoted at slip-band intersections by HELP or by HEDE at particle-matrix interfaces [3].

The mechanical properties of the steel such as elongation to failure, reduction of area, strain hardening rate, tensile strength, fracture toughness, and time to failure [14] deteriorate with the extended exposure to hydrogen especially under pressure. It has been well documented that hydrogen can greatly reduce fracture toughness of some steels by promoting brittle failure, and the exposure to hydrogen can greatly increase the FCGR [15]. This study is to further investigate how hydrogen assists the FCGR of carbon steel in a pressurized gaseous hydrogen environment, reflected in predictive models.

3 Predictive models

Existing models that predict hydrogen assisted fatigue crack growth (HA-FCG) response provide valuable insights on how the influencing variables can be integrated into the models. Fick's law is commonly utilized to calculate hydrogen diffusion, that is a substantial process for HE. Sieverts' law is crucial for determining the hydrogen concentration in the material. The Arrhenius equation can be applied when it is deemed appropriate to represent the process of hydrogen surface reaction and transport. Paris' law is employed to calculate the crack growth rate per cycle, $\frac{da}{dN}$, incorporating the relevant influencing variables. The HA-FCG is modeled as a superposition of FCG in air and FCG assisted by hydrogen, in some research studies. Some models such as the Cohesive Zone Model [16], the Phase Field Model [17], and the Quantum-Mechanically Informed Continuum Model [18] presented in the literature combine the physical models with numerical simulations. Each of these models is grounded in a specific theory of HE mechanisms, making them particularly well-suited for analyzing the specific scenarios of HE.

In Chapter 3, a theoretical environmentally assisted cracking (EAC) model proposed by Anderson [9] is firstly reviewed. A phenomenological hydrogen assisted fatigue crack growth rate (HA-FCGR) model developed by Amaro et al. [7] and its application in ASME B31.12 2023 Hydrogen Piping and Pipelines [8] are followed. A comparison is made between these two models in conjunction with additional test data available, intending to draw a more complete HA-FCGR predictive model. Lastly, a review is conducted on additional numerical models and analytical models to complement the first two models investigated. Closed form analytical models provide quantifiable visibility of the effects of material properties and testing parameters on the hydrogen enhanced fatigue crack growth rate; therefore, are investigated in more detail.

3.1 Theoretical EAC model

Anderson [9] models the EAC in three types of corrosion fatigue, that are cycle dependent corrosion fatigue, time dependent corrosion fatigue, and a combination of both.

Cycle dependent corrosion fatigue is represented is Equation (1) as:

$$\left(\frac{da}{dN}\right)_{aggressive} = \phi \left(\frac{da}{dN}\right)_{inert}, \quad (1)$$

where $\left(\frac{da}{dN}\right)_{aggressive}$ is the corrosion fatigue crack growth rate, $\left(\frac{da}{dN}\right)_{inert}$ is the inert growth rate, and ϕ is an acceleration factor.

Time dependent corrosion fatigue is modeled as a superposition of the inert fatigue crack growth rate and the environmental cracking rate, shown in Equation (2) as:

$$\left(\frac{da}{dN}\right)_{aggressive} = \left(\frac{da}{dN}\right)_{inert} + \frac{1}{f} \left(\frac{d\bar{a}}{dt}\right)_{EAC}, \quad (2)$$

where $\left(\frac{d\bar{a}}{dt}\right)_{EAC}$ is the average environmental crack growth rate over a loading cycle, and f is the loading frequency.

Combining Equation (1) and Equation (2) yields a general expression, Equation (3), for corrosion fatigue accounting for both cycle dependent and time dependent material-environment behaviour as follows:

$$\left(\frac{da}{dN}\right)_{aggressive} = \phi \left(\frac{da}{dN}\right)_{inert} + \frac{1}{f} \left(\frac{d\bar{a}}{dt}\right)_{EAC}, \quad (3)$$

Figure 3 illustrates the three types of corrosion fatigue behaviour.

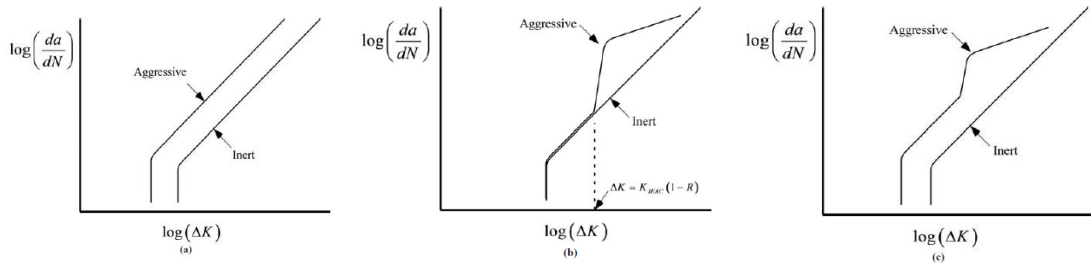


Figure 3 Corrosion fatigue behaviour (a) cycle dependent (b) time dependent (c) cycle and time dependent [9]

At high frequencies, the corrosion fatigue is dominated by the inert growth rate term, represented by Equation (1). At low frequencies, the environmental crack growth rate dominates over the corrosion fatigue with a rate proportional to $1/f$, represented by Equation (2).

This superposition model by Anderson [9] is theoretical. No specific values are provided for the acceleration factor ϕ . This model will be assessed in conjunction with the available fatigue test data in Chapter 3.3.

3.2 Phenomenological HA-FCGR model and its application

ASME B31.12 2023 [8] PL-3.7.1 Steel Piping Systems Design Requirements utilizes an upper bound simplification of a phenomenological model proposed by Amaro et al. [7], in the Performance-Based Design Method for Fracture Control and Arrest. The phenomenological model by Amaro et al. [7] is hereby investigated to predict the fatigue response of carbon steel in pressurized gaseous hydrogen environment. This model is of particular interest due to the increasing application of ASME B31.12 in the design of hydrogen pipelines within the energy sector. Chapter 3.2 details this predictive model and its application in ASME B31.12.

3.2.1 HA-FCGR model

Amaro et al. [19] present a coupled constitutive HA-FCG model to predict FCGR of pipeline steel exposed to high pressure gaseous hydrogen. Calibrations are required for the constitutive model and the HA-FCG model. Amaro et al. [7] further illustrate this phenomenological model that correlates the applied loading conditions, geometry, and hydrogen pressure with the resultant HA-FCG response in steel, based on extensive fatigue tests conducted in the pressurized gaseous hydrogen environment. Typical HA-FCG test results are categorized into three regions, namely A, B and C, when plotting $\frac{da}{dN}$ versus the range of stress intensity, ΔK , as shown in Figure 4.

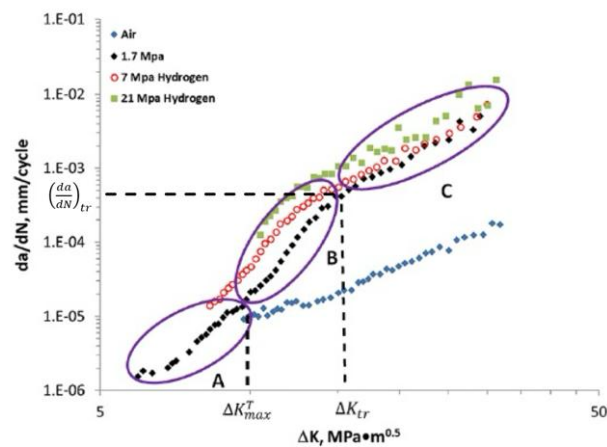


Figure 4 Typical HA-FCG results of API X100 steel delineated into three regions: A, B and C. All data is generated at a frequency of 1 Hz and load ratio R of 0.5 [7]

Region A is presumed to be dominated by a fatigue-only mechanism, as the produced fatigue surface in region A resembles that of tests conducted in air when ΔK is below a threshold stress intensity range, ΔK_{max}^T . It is hypothesized by Suresh and Ritchie [20] that hydrogen does not affect the FCG response of steels below a threshold stress intensity value, K_{max}^T . Region A is due to the stress intensity factor falling below K_{max}^T . In region B, the fatigue surface exhibits a more brittle FCG response with some hydrogen attack at grain boundaries. In contrast, the fatigue surface produced in region C suggests a transition to a more ductile fatigue behavior. The failure surface morphology produced in region C indicates that the effect of hydrogen has effectively saturated, resulting in a damage that consists of maximum hydrogen-induced damage (region B) and an additional ductile-type character similar to that found in region A. It is understood that the combined HA-FCG response results from the superposition of an FCG response unaffected by hydrogen (region A) and an FCG response assisted by hydrogen (region B and region C).

This categorization of region A, B, and C in HA-FCG response is consistent with the results from many other fatigue tests performed by other scientists. This model combines the constitutive stress-strain relation

and the HA-FCG model including several fitted empirical parameters. Furthermore, the simplified upper bound version of the model is implemented in the design code ASME B31.12 Hydrogen Piping and Pipelines [8].

The fatigue-only mechanism that dominates region A is bounded on one end by the threshold ΔK_{max}^T . The fatigue process zone (FPZ) size r_p needs to be introduced to further distinguish region B and C. It is hypothesized that when the value of $\frac{da}{dN}$ is smaller than $6r_p$, the HA-FCG response is dominated by the increased hydrogen accumulation, exponentially proportional to the hydrostatic stress, within the FPZ. This stress enhanced FCG response in hydrogen falls in region B that is the transient HA-FCG regime. On the other hand, when the value of $\frac{da}{dN}$ exceeds $6r_p$, the crack extension is affected primarily by the far-field hydrogen accumulation in the material, leading to an HA-FCG response dominated by traditional fatigue mechanisms in region C termed the steady-state regime. Figure 5 displays the notion of this hypothesis.

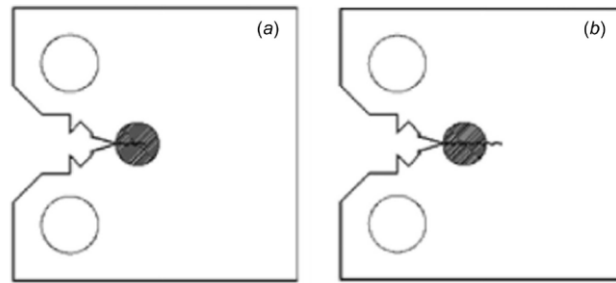


Figure 5 Exaggerated view of a single cycle da/dN occurring within the FPZ (a), and extending beyond the FPZ (b) [7]

The FPZ is the region ahead of the crack tip associated with high hydrostatic stresses and large plasticity as a result of cyclic loading. The FPZ size r_p is given in Equation (4) as:

$$r_p = \frac{(K_{max})^2}{6\pi\sigma_y}, \quad (4)$$

where σ_y is the yield strength of the material, and K_{max} is the maximum applied stress intensity factor given in Equation (5) as:

$$K_{max} = \frac{\Delta K}{1-R}, \quad (5)$$

where ΔK is the range of stress intensity factor, and R is the load ratio that is given in Equation (6) as:

$$R = K_{min}/K_{max}, \quad (6)$$

where K_{min} is the minimum applied stress intensity factor.

r_p is the first order estimate of plastic zone size, by the Irwin approach. The Irwin plastic zone correction is smaller by a factor of three due to suppressed yielding by the triaxial stress state under plain strain condition [9].

The initial $\frac{da}{dN}$ occurring within the FPZ nonetheless indicates an accelerated HA-FCGR in region C. Nibur et al. [21] suggest that if the crack extension rate exceeds the rate of hydrogen uptake and transport from the external environment to the crack tip process zone or FPZ, the effect of hydrogen on the crack growth is substantially weakened. The fatigue crack growth per cycle at the transition point between region B and region C, $\left(\frac{da}{dN}\right)_{tr}$, corresponds to a threshold value of ΔK_{tr} .

Based on the understanding that the FCG response in hydrogen is a superposition of a fatigue-only component and a hydrogen-assisted component, a predictive model presented in Equation (7) is proposed by Amaro et al. [7] as follows:

$$\left(\frac{da}{dN}\right)_{Total} = \left(\frac{da}{dN}\right)_{air} + \delta_H(P_H - P_{Hth}) \left(\frac{da}{dN}\right)_H, \quad (7)$$

where $\left(\frac{da}{dN}\right)_{Total}$ is the resultant FCG response, $\left(\frac{da}{dN}\right)_{air}$ is the FCG response for the material in air, and $\left(\frac{da}{dN}\right)_H$ is the FCG response assisted by hydrogen.

The Heaviside function δ_H turns the hydrogen FCG response on when the ambient hydrogen pressure P_H is above the threshold value of P_{Hth} . P_{Hth} is 0.02 MPa, due to the lack of available published HA-FCG results below this value.

$\left(\frac{da}{dN}\right)_{air}$ is given in Equation (8) as:

$$\left(\frac{da}{dN}\right)_{air} = a_{air} \cdot \Delta K^{B_{air}}, \quad (8)$$

$\left(\frac{da}{dN}\right)_H$ is understood to result from the interaction between two hydrogen-assisted mechanisms: one dominated by stress enhanced hydrogen accumulation at the crack tip, and the other dominated by the traditional fatigue-in-air damage mechanism though still aided by hydrogen. The cumulative damage model is employed to incorporate the interaction between the hydrogen dominated damage mechanism (transient regime) and the crack tip deformation dominated damage mechanism (steady-state regime). The two interacting HA-FCG mechanisms are therefore modeled as springs in parallel in Equation (9), as follows:

$$\left(\frac{da}{dN}\right)_H = \left[\left(\frac{da}{dN}\right)_{PH}^{-1} + \left(\frac{da}{dN}\right)_{\Delta K}^{-1} \right]^{-1}, \quad (9)$$

where $\left(\frac{da}{dN}\right)_{PH}$ is the HA-FCG response dominated by stress enhanced hydrogen accumulation within the FPZ (transient regime), and $\left(\frac{da}{dN}\right)_{\Delta K}$ is the HA-FCG response dominated by crack tip deformation (steady-state regime). They are expressed in Equation (10) and Equation (11) respectively as follows:

$$\left(\frac{da}{dN}\right)_{PH} = aH \cdot \Delta K^{BH} \cdot \left(P_H^{mH} \cdot \exp\left(\frac{-Q+V \cdot \sigma_h}{R_g T}\right)\right)^{dH}, \quad (10)$$

$$\left(\frac{da}{dN}\right)_{\Delta K} = aK \cdot \Delta K^{BK}, \quad (11)$$

where T is the absolute temperature, and σ_h is the hydrostatic stress at a critical distance $6r_p$ in front of the crack tip, Q is the activation energy for hydrogen diffusion that is equal to $2.71 \times 10^{-4} \text{ MJ/mol}$, V is the partial molar volume of hydrogen that is equal to $2.0 \times 10^{-6} \text{ m}^3/\text{mol}$, and R_g is the universal gas constant that is equal to $8.314 \times 10^{-6} \text{ MJ}/(\text{mol} \cdot \text{K})$.

Amaro et al. [19] [22] estimate the stress field in the FPZ using the Hutchinson, Rice, Rosengren (HRR) model [23] [24], which require several empirically fitted parameters. For the purpose of this study, expressions of the singular stress fields ahead of a crack tip for Mode I loading in a linear elastic isotropic material are adopted [9]. It leads to the expression of σ_h as follows:

$$\sigma_h = \frac{2(1+\nu)}{3\sqrt{2\pi}d} K_I, \quad (12)$$

where K_I is the stress intensity factor for Mode I loading, d is the critical distance in front of the crack tip, and ν is the Poisson ratio.

Amaro et al. [22] detail how $\left(\frac{da}{dN}\right)_{PH}$ is modeled. $\left(\frac{da}{dN}\right)_{PH}$ is correlated to the stress assisted hydrogen concentration, which is positively influenced by the far field equilibrium hydrogen concentration and the level of hydrostatic stress in the FPZ. Sievert's law predicts that the non-stressed hydrogen concentration is proportional to the square root of the hydrogen pressure $\sqrt{P_H}$. The eight parameters, a_{air} , B_{air} , aH , BH , mH , dH , aK and BK , are fitted parameters, meaning that this predictive model must be calibrated for each material of interest. Full model calibrations require a minimum of one test in air and one test at three different hydrogen gas pressures for each pipeline steel of interest.

A closed-form stress intensity solution is required for the model. Amaro et al. [19] apply the ΔK relationship from Anderson [9] shown in Equation (13) for a part through-crack on the interior of a pressurized pipe shown below:

$$\Delta K = (P_{max} - P_{min}) \left(\frac{\rho}{t} \sqrt{\frac{\pi a}{Q_f}}\right) F, \quad (13)$$

where P_{max} and P_{min} are the maximum and minimum internal pressure, ρ is the average radius of the vessel or pipe, t_w is the wall thickness, a is the crack depth, Q_f is the crack shape specific function, and F is a dimensionless geometric parameter. Q_f and F are determined by Equation (14) and Equation (15) respectively as follow:

$$Q_f = 1 + 1.464\left(\frac{a}{c}\right)^{1.65}, \quad (14)$$

$$F = 1.12 + 0.053\xi + 0.0055\xi^2 + (1 + 0.02\xi + 0.019\xi^2) \times \frac{(20 - \frac{\rho}{t_w})^2}{1400}, \quad (15)$$

where c is the half length of the crack where it intersects the surface, and ξ is the ratio of the crack depth over the wall thickness as shown in Equation (16):

$$\xi = 2c/t_w, \quad (16)$$

It should be noted that different forms of stress-intensity solutions result in vastly different predictions in this model. Amaro et al. [19] further demonstrate this phenomenon.

3.2.2 ASME B31.12 application

ASME B31.12 2023 [8] PL-3.7.1 Steel Piping Systems Design Requirements provides two options of design for Fracture Control and Arrest. Option A is a Prescriptive Design Method, and Option B is a Performance-Based Design Method. In the Performance-Based Design Method, FCGR properties determined by below Equation (17) may be used for fatigue analysis per Article KD-10 of ASME BPVC, Section VIII, Division 3 [25]. Equation (17) is expressed as:

$$\frac{da}{dN} = a1 \cdot \Delta K^{b1} + \left[(a2 \cdot \Delta K^{b2})^{-1} + (a3 \cdot \Delta K^{b3})^{-1} \right]^{-1}, \quad (17)$$

where $\frac{da}{dN}$ is the crack growth rate, and $a1$, $a2$, $a3$, $b1$, $b2$ and $b3$ are constants with values given in Table 1.

Table 1 Table PL-3.7.5-1 from ASME B31.12 [8]

Material Constants for Fatigue Crack Growth Rate, da/dN		
Material Constant	Values	
	SI	U.S. Customary
$a1$	4.0812 E-09	2.1746 E-10
$b1$	3.2106	3.2106
$a2$	4.0862 E-11	2.9637 E-12
$b2$	6.4822	6.4822
$a3$	4.8810 E-08	2.7018 E-09
$b3$	3.6147	3.6147

The units of $a1$, $a2$, $a3$, $b1$, $b2$ and $b3$ are not explicitly provided in ASME B31.12, therefore are summarized in SI as follows:

$b1$: dimensionless

$b2$: dimensionless

$b3$: dimensionless

$$a1 : 10^{-3} MPa^{-b1} m^{1-\frac{b1}{2}}$$

$$a2 : 10^{-3} MPa^{-b2} m^{1-\frac{b2}{2}}$$

$$a3 : 10^{-3} MPa^{-b3} m^{1-\frac{b3}{2}}$$

Equation (17) is applicable for carbon steel materials with a design pressure not exceeding 20 MPa. R ratio is required to be less than 0.5 for the application of Equation (17). The design also requires the minimum specified yield strength of the material not to exceed 550 MPa.

Equation (17) implemented in ASME B31.12 is the single, upper-bound simplification of the model developed by Amaro et al. [7] described in Chapter 3.2.1. Subsequently, the FCG response predicted by ASME B31.12 is intended to be conservative and safe.

3.3 Comparison of the EAC model and HA-FCGR model

The predictive model by Amaro et al. [7] resembles the time dependent corrosion fatigue model by Anderson [9], demonstrated in Figure 6. As shown in Figure 3, above a threshold value of ΔK , the time dependent corrosion fatigue is unique to the cycle and time dependent corrosion fatigue behaviour, if the acceleration factor ϕ is set to be equal to 1. Amaro et al. do not implicate a unit value acceleration factor but define region A as the fatigue only regime where the total da/dN is equal to the da/dN in air. Therefore, the model by Amaro et al. can also be interpreted as the cycle and time dependent corrosion fatigue model with a unit ϕ , demonstrated in Figure 7.

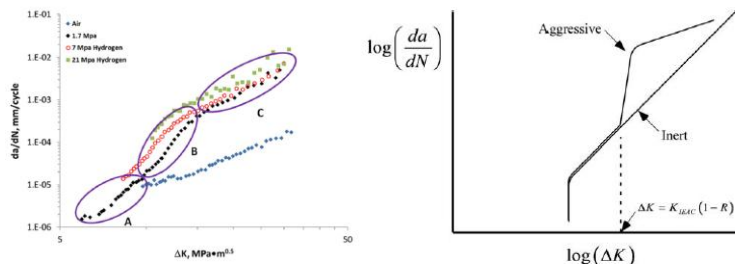


Figure 6 Comparison of the HA-FCGR model by Amaro et al. [7] and the time dependent EAC model by Anderson [9]

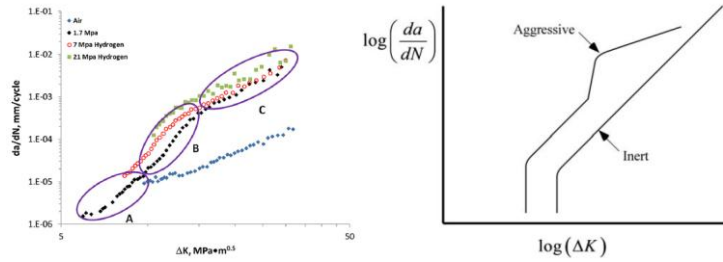


Figure 7 Comparison of the HA-FCGR model by Amaro et al. [7] and the cycle and time dependent EAC model by Anderson [9]

The model by Amaro et al. does not include the very low growth rates that are below 10^{-6} mm/cycle. Suresh and Ritchie [20] present corrosion fatigue at very low growth rates (lower than 10^{-6} mm/cycle) approaching a so-called threshold stress intensity range ΔK_0 , below which cracks grow at experimentally undetectable rates. Representative results are shown in Figure 8.

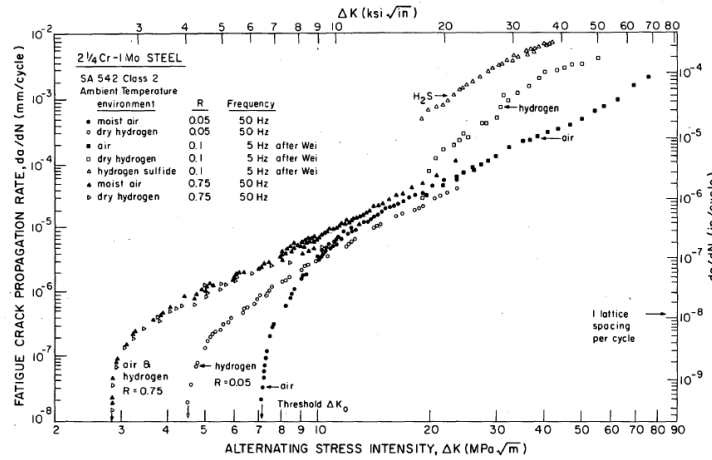


Figure 8 Fatigue crack propagation [20]

When the load ratio R is 0.05, the threshold ΔK_0 in air is close to 50% higher than that in dry hydrogen, and the near-threshold crack propagation rates are up to two orders of magnitude lower in air. Suresh and Ritchie contribute this phenomenon primarily to crack closure effects promoted by the formation of crack surface corrosion deposits. When ΔK reaches approximately $20 \text{ MPa}\sqrt{\text{m}}$, there is an abrupt enhancement of fatigue crack propagation due to the presence of hydrogen. This ΔK corresponds to the threshold ΔK_{max}^T in the model by Amaro et al., at which the fatigue-only mechanism dominated region A transitions to region B that is the transient stress enhanced FCG response regime. Suresh and Ritchie conclude that the difference of threshold ΔK_0 in air and hydrogen is only prevalent at low load ratios, and ΔK_{max}^T is sensitive to frequency, load ratio and pressure.

A schematic from Suresh and Ritchie [20] summarizes above findings, shown in Figure 9.

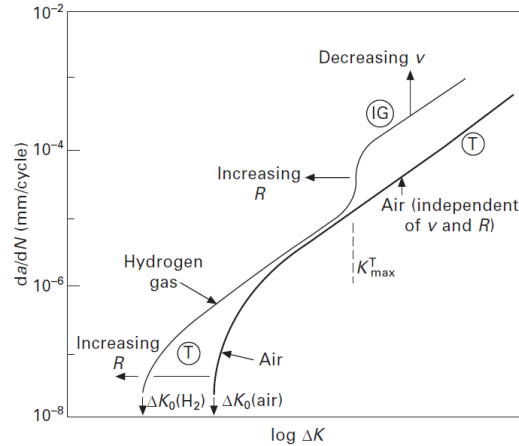


Figure 9 Schematic diagram of effect of dry gaseous hydrogen on fatigue-crack growth in lower strength steel [20], with ν representing the cyclic load frequency

The stress intensity range where the abrupt enhancement of crack growth rate due to hydrogen appears in Figure 3 (b) is determined as $\Delta K = K_{IEAC}(1 - R)$ by Anderson [9]. This is based on the assumption that K_{max} corresponding to this ΔK value equals to K_{IEAC} , that is the static loading threshold stress intensity for environmental cracking. Suresh and Ritchie [20] mark this same location of abrupt enhancement as K_{max}^T , shown in Figure 9, which in high strength steels is often coincident with the sustained-load (non-cyclic loading) threshold stress intensity, but in lower strength steels can be considerably less. Nevertheless, the theoretical model by Anderson and the test data by Suresh and Ritchie propose and confirm a correlation between the fatigue crack growth rate per cycle in a corrosive environment over alternating stress intensities, and the static-load threshold stress intensity.

The shapes of the hydrogen enhanced da/dN vs ΔK curves achieved by Suresh and Ritchie [20] are consistent with the ones from Amaro et al. [7], above the near-threshold levels. Additionally, the da/dN vs ΔK curves achieved by Suresh and Ritchie align with the EAC model by Anderson [9]. Although Anderson does not explicitly discuss the corrosion fatigue behaviour in steels at near-threshold levels, Figure 3 illustrates different ΔK_0 values for aggressive crack growth and crack growth in an inert environment.

3.4 Complementary models

Chapter 3.4 presents a review of additional predictive models that complement the two previously discussed. These models are categorized as either numerical or analytical, and the review aims to further explore how the effects of influencing variables on the HA-FCGR are incorporated into these models.

3.4.1 Numerical

3.4.1.1 Models

1, Martinez-Paneda et al. [26] implement a coupled large-strain Finite Element Analysis-Strain Gradient Plasticity framework to analyze the crack tip stress in combination with hydrogen enhanced decohesion mechanism based models. These models predict the threshold and kinetics properties of hydrogen environment assisted cracking propagation. Model assessment is based on measurements of da/dt versus the stress intensity factor for model I (K_I). Hardening due to the plastic strain gradient is incrementally captured through the generalized plastic strain rate.

2, Busto et al. [27] present a finite element framework to model hydrogen assisted fatigue by means of a hydrogen and cycle-dependent cohesive zone formulation. The scheme appropriately captures the sensitivity of fatigue crack growth rates to the loading frequency and the environment. Mechanical loading and hydrogen transport are coupled through lattice dilatation due to hydrostatic stress and the generation of traps by plastic straining.

3, Fernández-Sousa et al. [28] present a new formulation combining multi-trap stress assisted diffusion mechanism based strain gradient plasticity and a hydrogen and fatigue dependent cohesive zone model. The results show that the fatigue crack growth behaviour is governed by the ratio of loading frequency to effective diffusivity.

4, Moriconi et al. [16] implement a cohesive zone model in which the cohesion energy of the metallic lattice in the presence of hydrogen is reduced, in the finite element code ABAQUS. A specific traction separation law suitable for cyclic loadings and dependent on local hydrogen concentration is developed. Hydrogen diffusion influenced by hydrostatic stress and trapping is considered. The cyclic stress-strain behavior of the bulk material is described by an elasto-plastic constitutive law which is insensitive to the presence of hydrogen.

The hydrogen concentration in lattice (C_L) and traps (C_T) are considered as the product of hydrogen (θ_L/θ_T) occupancy and hydrogen lattice and trap sites density per unit volume (N_L/N_T), as follows:

$$C_L = \theta_L N_L , \tag{18}$$

$$C_T = \theta_T N_T , \tag{19}$$

The overall hydrogen coverage rate, θ , is a function of local hydrogen concentration in the material C_H and the Gibbs free energy difference between any microstructural interface in the bulk material Δg_b^0 , as follows:

$$\theta = \frac{C_H}{C_H + \exp\left(\frac{-\Delta g_b^0}{R_g T}\right)}, \quad (20)$$

The diffusion of hydrogen in stress fields in the bulk material is described as the following diffusion equation:

$$\frac{\partial C_L}{\partial t} + \frac{\partial C_T}{\partial t} - \vec{\nabla} \cdot (D_L \vec{\nabla} C_L) + \vec{\nabla} \cdot \left(\frac{D_L C_L \bar{V}}{R_g T} \vec{\nabla} \sigma_h \right) = 0, \quad (21)$$

where D_L is the lattice diffusivity coefficient, and \bar{V} is the mean molar volume of hydrogen.

This equation is originally proposed by Sofronis and McMeeking [14] and subsequently modified by Krom et al. [29] adding a strain rate factor. The results of the numerical modeling by Sofronis and McMeeking demonstrate that hydrogen accumulates mainly in traps near the crack surface during plastic straining, and the hydrogen concentration at normal interstitial lattice sites is only mildly elevated at peak hydrostatic stress site near the notch. This leads to the conclusion that the areas of high hydrogen concentration are determined predominantly by the plastic strain due to its role in creating traps. Krom et al. modified the equation by adding a strain rate factor to provide a hydrogen balance, concluding that an increasing strain rate reduces the hydrogen concentration in lattice sites due to the filling of trap sites.

5, Golahmar et al. [17] present a theoretical and numerical phase field based model for predicting hydrogen-assisted fatigue. The coupled deformation-diffusion-damage model enables predicting fatigue crack nucleation and growth. The drop in fracture resistance of metals exposed to hydrogen is captured by a quantum mechanically informed degradation law. Fatigue damage is also captured by a fatigue degradation function. Hydrogen transport is characterized by the definition of the chemical potential. Cracking is predicted with an energy-based criterion grounded on the thermodynamics of crack growth. The model adequately captures the sensitivity of fatigue crack growth rates to hydrogen content, and finds the crack tip hydrogen distribution is very sensitive to the loading frequency and the material diffusivity. ΔK is normalized by a reference stress intensity factor K_r that is expressed as $\sqrt{\frac{G_c E}{(1-\nu)^2}}$, where G_c is the material toughness.

6, Lee et al. [30] study the ultrasonic vibration fatigue life of Body Centered Cubic steel with a ferrite pearlite microstructure pre-charged with hydrogen at different concentrations. At concentrations above and below the critical hydrogen concentration, hydrogen enhanced decohesion and hydrogen enhanced localized plasticity mechanism dominate the embrittlement process respectively. Modeling is based on the unified mechanics theory which requires analytical derivation of the thermodynamic fundamental equation of the material. The entropy generation mechanisms due to mechanical loading are composed of

temperature gradient induced thermal conduction, fast-moving dislocation, motion-induced internal friction, and stress concentration induced micro-plasticity. The entropy generation mechanisms due to electrochemical corrosion resulting from the activation overpotential are also introduced.

7, Hosseini et al. [31] present a model for fatigue crack propagation induced by alternating crack tip plastic blunting and re-sharpening, accelerated by hydrogen enhanced dislocation motion and generation. The Chaboche constitutive model, a nonlinear kinematic hardening model, is used for the calculation of the stress and strain fields at the propagating crack tip. The predicted crack propagation in the presence of hydrogen is based on the hydrogen effect on the plastic dissipation as governed by the hydrogen interaction with the plastic deformation, hence the approach does not rely on a phenomenological superposition of separate effects in the presence and absence of hydrogen.

3.4.1.2 Summary

The purpose of the present study is to predict the fatigue crack growth rate of pipeline steel in pressurized gaseous hydrogen given the steel properties and the expected operating conditions. This study seeks to develop a refined prediction model for hydrogen assisted crack growth that directly quantifies the effect of the steel properties and pipeline operating parameters on the crack growth rate. To achieve this, crack growth prediction models that rely on numerical simulations in finite element analyses are not preferred.

3.4.2 Analytical

3.4.2.1 Models

1, Xing et al. [32] explore the hydrogen diffusion effect on crack propagation under cyclic loading using fracture mechanics. H potential, hydrogen diffusivity, hydrostatic stress near crack tip, and the loading frequency are considered. This model provides physical meanings to rationalize the empirical Paris' Law.

The hydrogen concentration near the crack tip considering the equilibrium condition can be expressed as:

$$c_H = c_0 \exp\left(\frac{\sigma_h \Omega}{k_B T}\right), \quad (22)$$

where c_0 is the atomic ratio of H/Fe away from the crack tip, Ω is the partial volume of hydrogen, k_B is the Boltzmann constant, T is the temperature, and σ_h is the hydrostatic stress.

Employing the criteria that the crack propagates when the atomic ratio reaches 1, the length of the saturated zone is estimated as:

$$L(K_I) = \left(\frac{4(1+\nu)\Omega}{3\pi k_B T \sqrt{2\pi} \ln(1/c_0)}\right)^2 K_I^2, \quad (23)$$

The maximum crack growth rate due to hydrogen enhanced decohesion $\left(\frac{da}{dN}\right)_{HEDE}^{max}$ can be written as:

$$\left(\frac{da}{dN}\right)_{HEDE}^{max} = L_{max} - L_{min} = \left(\frac{4(1+\nu)\Omega}{3\pi k_B T \sqrt{2\pi} \ln(1/c_0)}\right)^2 \left(\frac{1+R}{1-R}\right) \Delta K^2, \quad (24)$$

A critical load frequency $f_{critical}$ is introduced, below which the crack propagation rate reaches the maximum and stays as a constant. $f_{critical}$ is $1/(2t_{critical})$ and $t_{critical}$ equals to the ratio of the size of the zone that supplies or depletes hydrogen atoms over the average velocity. $f_{critical}$ is hence given as:

$$f_{critical} = \frac{(1+\nu)\Omega D(K_{max}+K_{min})((1/\sqrt{r_{in}})-(1/\sqrt{R_{eq}}))}{\pi(R_{eq}-r_p)^2 k_B T 3\sqrt{2\pi}}, \quad (25)$$

where r_{in} and R_{eq} are the inner radius and outer radius of the annulus region that supplies or depletes the exchange of hydrogen atoms in the plastic zone, and D is the hydrogen diffusivity.

When the load frequency f is above $f_{critical}$, $\left(\frac{da}{dN}\right)_{HEDE}$ varies with f , as shown below:

$$\left(\frac{da}{dN}\right)_{HEDE} = \left(\frac{da}{dN}\right)_{HEDE}^{max} \left(\frac{f_{critical}}{f}\right)^\gamma, \quad (26)$$

where γ is a fitted parameter.

The hydrogen enhanced decohesion crack propagation rate based on hydrogen diffusion and critical loading frequency is related to the Paris' law from experimental results as follows:

$$\log\left(\frac{da}{dN}\right)_{tot} / \log\left(\frac{da}{dN}\right)_{HEDE} = n_p, \quad (27)$$

where n_p is a fitted parameter.

A crack propagation model in the form of Paris' law is simplified as follows:

$$\left(\frac{da}{dN}\right)_{Total} = A \left(\left(\frac{1+R}{1-R}\right) \frac{\Delta K^2}{(f/f_{critical})^\gamma}\right)^{n_p}, \quad f > f_{critical} \quad (28)$$

$$A = \left(\frac{4(1+\nu)\Omega}{3\pi k_B T \sqrt{2\pi} \ln(1/c_0)}\right)^{2n_p}, \quad (29)$$

In this model, the phenomenon of frequency effect adopted is contrary to the peculiar frequency effect observed by Yamabe et al. [33], Yoshikawa et al. [34] and Wei et al. [35], in which the fatigue crack growth rate increases with a decreasing f , reaches a maximum value, and begins to decrease while f continues to decrease. However, an equation is provided to determine $f_{critical}$, based on first principles. Fig 2(c) from Yamabe et al. [33] shows that the value of $f_{critical}$ decreases with the increase of hydrogen gas pressure. The hydrogen partial volume Ω is proportional to $1/P_H$, according to the ideal gas equation that is $P_H V = n_m R_g T$, where n_m is the number of mole of gas. Through Ω , $f_{critical} \propto 1/P_H$.

In this model, γ and n_p are fitted parameters. Ω and far field hydrogen concentration c_0 are unknown. Ω can be written as $n_m RT/P_H$ through the ideal gas equation, and c_0 can be expressed by Sievert's law as $K_H \sqrt{P_H}$, where K_H is the Sievert's constant.

2, Hołobut [36] propose a method of predicting fatigue crack growth in hydrogen-charged thin steel plates. Stress intensity factors are modified to reflect the presence of hydrogen. The modification accounts for hydrogen embrittlement of crack tips and hydrogen induced residual stresses in the plate.

The growth of linear cracks under uniaxial fatigue takes the following form:

$$\frac{da}{dN} = f(K_{max}, K_{min}, m_1, \dots, m_n), \quad (30)$$

where m_i are sample specific parameters.

Hydrogen enhanced decohesion mechanism is employed. It is assumed that hydrogen, through promoting decohesion, affects the way in which the material perceives the external loading. Hence, hydrogen is regarded as a source of additional loading inside the material.

The Forman equation is selected as the guiding fatigue law, that is

$$\frac{da}{dN} = \frac{\alpha' \Delta K^\mu}{K_c / K_{max} - 1}, \quad (31)$$

where K_c is the material fracture toughness, and α' and μ are empirical constants.

$K_{max/min}$ thus ΔK are expressed as follows:

$$K_{max/min} = \frac{(\sigma_0 + \bar{\sigma})(S_{max/min} + \bar{\sigma})}{\sigma_0 + \bar{\sigma} - \gamma' \bar{C}} \sqrt{\pi c}, \quad (32)$$

$$\Delta K = \frac{(\sigma_0 + \bar{\sigma})(S_{max} - S_{min})}{\sigma_0 + \bar{\sigma} - \gamma' \bar{C}} \sqrt{\pi c}, \quad (33)$$

where σ_0 is the cohesive force in absence of hydrogen, $\bar{\sigma}$ is an approximate, constant σ along the crack, S_{max} and S_{min} are the maximum and minimum external cyclic loading, γ' is the coefficient of hydrogen enhanced decohesion, \bar{C} is the approximate, constant hydrogen concentration in cohesive zone, and c is the half crack length

This prediction model fundamentally follows Paris' law. The K_c / K_{max} term in the prediction model reflects the fatigue cracking behaviour near the fracture roughness of the material. The stress intensity range in this model is increased due to the presence of hydrogen reducing the cohesive force in the material. The cohesive stress in the cohesive zone with the presence of hydrogen is approximated as $\sigma_0 - \gamma' \bar{C}$.

3, Ronevich et al.[37] present fatigue crack growth rate by two Paris' law relationships as shown below:

$$\left(\frac{da}{dN}\right)_{high} = 1.5 \times 10^{-11} \left(\frac{1+2R}{1-R}\right) \Delta K^{3.66}, \quad (34)$$

$$\left(\frac{da}{dN}\right)_{low} = 3.5 \times 10^{-14} \left(\frac{1+0.43R}{1-R}\right) \Delta K^{6.5} g(P), \quad (35)$$

where $(\frac{da}{dN})_{high}$ represents the pressure independent regime at high ΔK , and $(\frac{da}{dN})_{low}$ represents the pressure dependent regime at low ΔK , with the $g(P)$ term capturing the pressure dependence of fatigue crack growth in gaseous hydrogen. $g(P)$ is derived from the gas physics assuming non-ideal gas behaviour and a regular solution model for gas blends, as follows:

$$g(P) = (\frac{f_H}{f_r})^{1/2} = [(\frac{P_{Hp}}{P_r}) \exp(\frac{b}{R_g T} (P_T - P_r))]^{1/2}, \quad (36)$$

where f_H and f_r are the fugacity of hydrogen and reference condition, P_{Hp} and P_r are the hydrogen partial pressure and reference condition, P_T is the total pressure, and b is the co-volume constant from the Abel Noble equation of state for hydrogen.

This model acknowledges that the pressure dependence of hydrogen assisted fatigue crack growth appears at low ΔK . The pressure dependence is directly reflected in the $g(P)$ term. Load ratio R is also incorporated in the Paris' relationship. The input parameters in the $g(P)$ term can be attained. This model is comparable to the prediction model by Amaro et al. [7], in which the transient regime at medium ΔK is dependent on pressure and the steady state regime at high ΔK is independent of pressure, as shown in Equation (10) and Equation (11).

4, McEvily and Wei [38] provide an expression of crack growth rate per cycle for $R=0$ loading as follows:

$$\frac{\Delta a}{\Delta N} = \frac{4A}{\pi \sigma_y E} (K_{max}^2 - K_{TH}^2), \quad (37)$$

where K_{TH} is the threshold stress intensity factor for fatigue loading, and for tests in vacuum, A follows:

$$A = 2\sigma_y / E, \quad (38)$$

A corrosive environment increases A and decreases K_{TH} . A simple linear superposition of stress corrosion effects upon mechanical fatigue process is provided as follows:

$$(\frac{\Delta a}{\Delta N})_c = (\frac{\Delta a}{\Delta N})_r + \int \frac{da}{dt} k(t) dt, \quad (39)$$

where $(\frac{\Delta a}{\Delta N})_c$ is the fatigue crack growth rate in an aggressive environment, $(\frac{\Delta a}{\Delta N})_r$ is the fatigue crack growth rate in an inert environment, $\frac{da}{dt}$ is the crack growth rate per unit time, and $k(t)$ is not specified.

A related approach to account for the frequency effects on the corrosion fatigue behaviour is expressed as:

$$\frac{\Delta a}{\Delta N} = \frac{8}{\pi} [(\frac{K_{max}}{E})^2 - (\frac{K_{TH}}{E})^2] + b(f), \quad (40)$$

where $b(f)$ is the amount of tarnish formed per cycle, that is a function of frequency f .

The threshold value of the stress intensity amplitude as a function of the threshold value of the stress intensity amplitude at $R=0$ loading, load ratio R , and fracture toughness K_C , is given by:

$$K_{ATH} = \frac{K_{ATH0}}{1 + \left(\frac{2R}{1+R}\right)^{\frac{K_{ATH0}}{K_C}}}, \quad (41)$$

R directly influences the threshold K value, which agrees with the experimental results from Suresh and Ritchie [20].

This model includes the fatigue cracking behaviour near the crack initiation threshold K . For the model to be adopted, $k(t)$ and $b(f)$ should be firstly defined.

5, Wei and Shim [39] infer that environmentally assisted crack growth is the result of a number of different processes operating in sequence, and the rate of crack growth is controlled by the slowest process in this sequence. This agrees with the competing model from Amaro et al. [40].

The fatigue crack growth in a gaseous environment that is deleterious is modeled as:

$$(da/dN)_e = (da/dN)_r + (da/dN)_{cf} + (da/dN)_{scc}, \quad (42)$$

where $(da/dN)_r$ is the fatigue crack growth rate in an inert environment, $(da/dN)_{cf}$ is the cycle dependent contribution that requires the synergistic interaction of fatigue and environmental attack, and $(da/dN)_{scc}$ is the contribution by sustained load growth.

Comparing to the theoretical EAC model proposed by Anderson [9], this model does not accelerate $(da/dN)_r$ but includes a cycle dependent contribution $(da/dN)_{cf}$.

Based on the assumptions of Knudsen (or molecular) flow and simple first-order reaction kinetics, the following relationships are presented for transport controlled and surface-reaction controlled fatigue crack growth respectively:

$$(da/dN)_{cf} = (da/dN)_{cf,s}(P_o/2f)/(P_o/2f)_s = (da/dN)_{cf,s}(P_o/P_{o,s}), \quad (43)$$

$$(da/dN)_{cf} = (da/dN)_{cf,s}[1 - \exp(-k_c P_o/2f)], \quad (44)$$

where $(da/dN)_{cf,s}$ is the maximum enhancement recognizing the surface reaction is limited, P_o is the external gas pressure, k_c is the reaction rate constant.

It is assumed that $(da/dN)_{cf}$ is proportional to the amount of hydrogen produced by the surface reaction during each cycle. In this model $(da/dN)_r$ and $(da/dN)_{cf,s}$ are experimentally measured limits. $P_o/2f$ is investigated as an input parameter for the crack growth response curves, which is comparable to the $\sqrt{P_H f}$ term from Yoshikawa et al. [34].

6, Wei and Simmons [41] further provide the governing differential equations for flow and surface reactions, and the relationship for $(da/dN)_{cf}$, to demonstrate expressions of $(da/dN)_{cf}$ controlled by transport and surface reaction. Significantly, $(P_o/2f)_s$ is provided as follows:

$$(P_o/2f)_s = (4.36 \times 10^2 \frac{\beta}{\alpha'' N_o R_g T E^2} (\sigma_{ys}^2 (T/M_g)^{1/2})^{-1}, \quad (45)$$

where β is an empirical quantity, α'' is an empirical constant for surface roughness and crack geometry, N_o is the density of the surface sites, M_g is the molecular weight of the gas.

Figure 10 by Wei and Simmons [41] is presented below to illustrate the fatigue crack growth controlled by gas transport and surface reaction, in terms of $P_o/2f$.

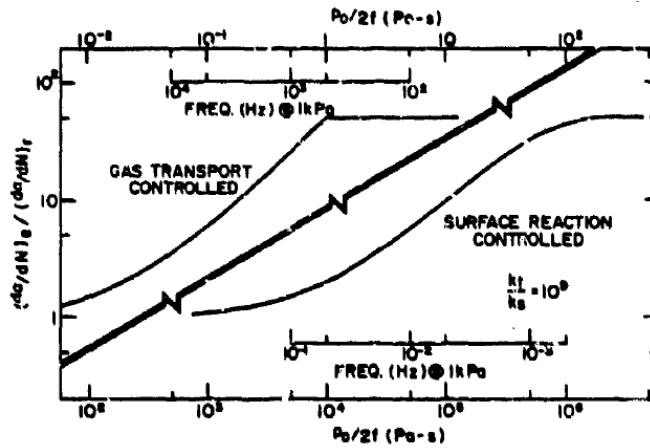


Figure 10 Schematic illustration and comparison of gas transport and surface reaction controlled fatigue crack growth [41]

To adopt this model, sustained load growth contribution $(da/dN)_{SCC}$ needs to be formulated, and the maximum enhancement $(da/dN)_{cf,s}$ needs to be measured. Additionally, α'' and β in the $(P_o/2f)_s$ term are empirically fitted constants.

7, Thomas and Wei [42] provide a heuristic modeling of the hydrogen enhanced fatigue crack growth process, including:

$$(da/dN)_{cf} = (da/dN)_s \phi', \quad (46)$$

where $(da/dN)_s$ is the saturation crack growth rate, and ϕ' is the fractional amount of “pure corrosion” fatigue.

To account for the frequency and temperature response, the followings are proposed:

$$(da/dN)_{cf} = (da/dN)_s (1 - \exp(-\frac{\kappa}{f})), \quad (47)$$

$$\kappa = C_k \Delta K^{n_x} \exp\left(-\frac{\Delta E_a}{R_g T}\right), \quad (48)$$

where C_k , n_x , and ΔE_a are estimated values via multi least squares linear regression.

$(da/dN)_s$ in this model needs to be determined separately.

This model resembles the surface reaction controlled model by Wei and Simmons [41], in which the reaction rate constant and the external gas pressure effects are considered. This model introduces κ to account for the temperature response, which includes three estimated parameters by regression.

8, Barsom [43] investigate the corrosion fatigue crack growth of structural steels at stress intensity ranges ΔK below the stress corrosion cracking threshold stress intensity factor K_{ISCC} . The primary factor affecting fatigue crack growth rate in the environment-material system is shown to be the applied energy release rate, $\Delta \mathcal{G}$ in psi-in, which is related to the stress intensity factor K . Below expression is proposed to predict the corrosion fatigue crack growth rate for ΔK values below K_{ISCC} :

$$\frac{da}{dN} = D(t)(\Delta \mathcal{G}), \quad (49)$$

where $D(t)$ is a time or frequency dependent function.

$D(t)$ decreases with increasing cyclic stress frequency. At very high frequencies, the rate of fatigue crack growth outpaces the environmental effects, $D(t)$ approaches a constant value that can be predicted from fatigue crack growth data in air. It is also suggested that $D(t)$ reaches a maximum at a low frequency which may be characteristic of the environment-material system.

The model developed by Xing at al. [32] applies this conclusion, which is not in full agreement with the peculiar frequency effect observed by Yamabe et al. [33] and Yoshikawa et al. . Further investigation of frequency effect is necessary.

9, Nelson and Williams [44] provide the overall crack growth rate as follows:

$$\left(\frac{da}{dt}\right)_{overall} = \left[\frac{1}{\left(\frac{da}{dt}\right)_I} + \frac{1}{\left(\frac{da}{dt}\right)_{II}}\right]^{-1} + \left(\frac{da}{dt}\right)_{III}, \quad (50)$$

In Stage I, da/dt is strongly dependent on K at low K values; in Stage II, da/dt becomes relatively independent of K at intermediate K values. da/dt increases rapidly in Stage III when K approaches the crucial value of stress intensity K_c . Stage I and II are sequential processes with the slower process controlling the overall rate, and Stage III is parallel to the operation of Stage I and II. The structure of this model resembles the springs in parallel structure of the prediction model by Amaro et al. [7], in which the transient regime and steady state regime are the sequential processes, parallel to fatigue in air mechanism.

A quantitative understanding of the chemical and mechanical influences involved in Stage I and Stage II crack growth is initiated. Quantitative relationships between da/dt and stress intensity factor, temperature, pressure, and yield strength of the material, for Stage I and Stage II crack growth in hydrogen and water are developed. An attempt is made to separate the kinetic and mechanistic aspects of the embrittlement process.

The mechanism by which the energy adsorbing ability of a metal lattice is reduced by the presence of a chemical species and the kinetic processes involved in getting the chemical species from the environment to the point where it can interact with the metal lattice, are both considered in the environmental embrittlement. The study adopted the equilibrium theory by Oriani and Josephic [13] which combines the mechanistic and kinetic aspects of environmental hydrogen embrittlement into what could be considered a semi-quantitative theory of hydrogen-induced cracking. The following two equations describe the theory:

$$c'(\sigma'_Z, f_H, da/dt)_M \geq c'' , \quad (51)$$

$$\sigma'_Z = 2\sigma(L/\rho)^{1/2} \geq n_b F_m(c''), \quad (52)$$

The first equation indicates that hydrogen-induced cracking only proceeds when the concentration of the hydrogen near the crack tip, c' , reaches a critical value, c'' . c' is a dynamic function of the tensile stress across the plane of the crack, σ'_Z , the hydrogen fugacity, f_H , and the crack velocity, da/dt , as determined by the rate controlling mechanism, M . The second equation states that decohesion occurs when the local tensile stress, σ'_Z , a function of applied stress, σ , crack length, L , and crack-tip radius, ρ , is greater than, or equal to, the product of the reduced cohesive force of the metal-metal bond, $F_m(c'')$, and the number of such bonds at the crack tip, n_b .

Considering the stress intensity factor is proportional to the limiting value of the elastic stress concentration factor, as the root radius approaches zero, and to account for the dependence of fracture toughness on crack tip radius, below equation is provided:

$$K \geq f(\rho)nF_m(c'') , \quad (53)$$

where $f(\rho)$ is a proportionality constant, that is an undefined function of ρ .

The study suggests that Stage II crack growth is a result of some surface reaction that is stress dependent.

The $\frac{da}{dt}$ over K curve exhibits a finite slope for the ANSI-4130 steel.

In Stage I, the crack initiation threshold K_{TH} was not observed in the investigation. For the ANSI-4130 steel, the Stage I curve exhibits a finite and constant slope for stress intensities down to the lowest at which

crack growth rates could be reliably measured ($\approx 10^{-8}m/s$). In gaseous hydrogen environment, for ANSI-4130 steel, crack growth velocity in Stage I and II are approximated as follows:

$$\left(\frac{da}{dt}\right)_I \propto \exp(K), \quad (54)$$

$$\left(\frac{da}{dt}\right)_{II} \propto \exp(0.1K), \quad (55)$$

Taking into account of the influence of test parameters, combined with the relations observed and fitted from the test data, below equations are provided:

$$K \propto T^{n_T}, \left(\frac{da}{dt}\right)_I \propto \exp(K/T^{n_T}), \quad (56)$$

$$K \propto P_H^{-0.2}, \left(\frac{da}{dt}\right)_I \propto \exp(P_H^{0.2}), \quad (57)$$

$$K \propto \sigma_y^{-5}, \left(\frac{da}{dt}\right)_I \propto \exp(\sigma_y^5 K), \quad (58)$$

where n_T equals 2 at higher strength levels and decreases as yield strength decreases.

This model is included to represent the possible $\frac{da}{dt}$ relation with K . Equations of $\frac{da}{dt}$ in Stage I and II are proposed. Temperature, pressure, and yield strength are incorporated into the $\frac{da}{dt}$ equations in Stage I as well. The proposed separate kinetic and mechanical mechanisms in embrittlement, can also be used to explain the frequency effect, even though the dynamic function of c' is not explicitly provided.

3.4.2.2 Summary

Xing et al. [45] propose an expression to determine the critical load frequency incorporated $f_{critical}$, and include the term of $f_{critical}/f$ in the predictive model to account for the frequency effect. McEvily and Wei [38] propose to add a $b(f)$ term that is a function of frequency. The applied energy release rate is multiplied by a $D(t)$ term that is frequency dependent to predict the corrosion fatigue crack growth by Barsom [43].

Ronevich et al. [37] propose a model that resembles the phenomenological model by Amaro et al. [7]. Instead of the multiplier in Equation (10), Ronevich et al. introduce a $g(P)$ term as shown in Equation (35) that accounts for the effect from hydrogen pressure.

Wei and Shim [39], Wei and Simmons [41], and Thomas and Wei [42] propose a superposition model for fatigue crack growth in a deleterious environment counting fatigue crack growth in an inert environment, cycle dependent contribution, and time dependent contribution. The concepts of maximum enhancement

and saturation crack growth are introduced. A fraction is then applied to account for the effects of pressure, frequency, and temperature.

Nelson and Williams [44] hypothesize that hydrogen induced cracking is attributed to both the mechanistic and kinetic aspects of environmental hydrogen embrittlement. The concentration of the hydrogen near the crack tip reaching a critical value, combined with the local tensile stress exceeding the reduced cohesive force, is required for the hydrogen induced cracking to occur.

3.4.3 Summary

Below Table 2 summarizes above described prediction models in Chapter 3.4.

Table 2 Summary of additional prediction models from literature

Reference	Core theory	Model type	Fitted parameters	Measured or estimated parameters
Martinez-Paneda et al. [26]	Strain gradient plasticity	Numerical	N/A	N/A
Busto et al. [27]	Cohesive zone for fatigue	Numerical	N/A	N/A
Fernández-Sousa. [28]	Cohesive zone for fatigue and strain gradient plasticity	Numerical	N/A	N/A
Moriconi et al. [16]	Cohesive zone for fatigue	Numerical	N/A	N/A
Golahmar et al. [17]	Phase field	Numerical	N/A	N/A
Lee et al. [30]	The unified mechanics theory	Numerical	N/A	N/A
Hosseini et al. [31]	Crack tip plastic blunting and re-sharpening	Numerical	N/A	N/A
Xing et al. [46]	Fracture mechanics	Analytical	Yes	Yes
Holobut [36]	Modified stress intensity factor to account for hydrogen	Analytical	Yes	Yes
Ronevich et al. [37]	Pressure dependence term	Analytical	Yes	Yes
McEvily and Wei [38]	Fracture mechanics	Analytical	Unknown	Yes
Wei and Shim [39]	Fracture mechanics	Analytical	Yes	Yes
Wei and Simmons [41]				
Thomas and Wei [42]	Fracture mechanics	Analytical	Yes	Yes
Barsom [43]	Fracture mechanics	Analytical	Unknown	Unknown
Nelson and Williams [44]	Fracture mechanics	Analytical	N/A	N/A

3.5 Conclusion

The Paris' relationship reasonably remains the core equation in the predictive models. A superposition structure with a multiplying term or an additive term to account for the effects of test parameters are adapted repeatedly. This study intends to refine an analytical model predicting hydrogen assisted fatigue crack growth by reducing the number of empirical parameters required for the prediction, grounded to first principles and the evidence presented in the previous test results.

4 Influencing variables

One of the primary factors that affects the FCGR of steel in hydrogen is the amount of hydrogen that a material absorbs under certain conditions. Generally, with the increasing concentration of hydrogen at the crack tip, the FCGR increases. Once hydrogen saturation is reached, the hydrogen enhancement on the crack growth is weakened. The influences of the hydrogen gas pressure, load frequency, temperature, load ratio R , strength and microstructure of the steel on the FCGR of the steel are evaluated in this chapter. The hydrogen gas pressure, load frequency, stress intensity range, temperature and load ratio are test parameters that can be measured and controlled in a fatigue test. The strength and microstructure of the steel are input material properties. These variables are therefore key variables that can be available to be investigated while refining the predictive model. The influences of above-mentioned variables on the HA-FCGR are categorized based on findings from previous experiments in Chapter 4.1 and Chapter 4.2. Some key threshold stress intensity values observed in typical HA-FCGR predictive models are investigated in Chapter 4.3.

4.1 HE

The risk of HE is estimated by the stress-strain curve obtained for the material of interest, accompanied by the hydrogen permeation test. A higher hydrogen concentration in the material leads to a higher risk of HE. A critical hydrogen concentration is reached when the steel begins to exhibit brittle behavior due to HE.

Alvarez et al. [47] pre-charged specimens with gaseous hydrogen in a high pressure reactor, with a pressure of 19.5 MPa, for 21 hours at 450°C. Hydrogen permeation tests and fracture toughness tests were performed at room temperature. S355 steel exhibited higher effective diffusion coefficient, lower apparent subsurface hydrogen concentration and lower initial hydrogen concentration, comparing to H8 steel. As a result, the risk of HE for the lower strength steel S335 is lower. For the two steels tested, specimens with pre-charged hydrogen showed an approximately 50% reduction of fracture toughness J_{IC} (kJ/m^2) comparing to non-charged specimens. Additionally, a lower displacement rate led to a lower fracture toughness J_{IC} .

Eichinger et al. [48] performed electrochemical permeation measurements. Constant load tests were conducted at 90% of the yield strength. The test duration was chosen to be three days to achieve complete hydrogen saturation and provide sufficient time for hydrogen diffusion. Under the same hydrogen partial pressure, the hydrogen uptake increased with the test temperature (25°C, 200°C). Under the same test temperature, the hydrogen uptake increased with the hydrogen partial pressure (100 bar, 300 bar, 1000 bar). For L80 steel, the loading of 90% yield strength did not increase hydrogen uptake. For L110 steel, the loading of 90% yield strength increased hydrogen uptake at hydrogen partial pressure of 100 bar and 300

bar. At 1000 bar, the loading of 90% yield strength increased hydrogen uptake at 25°C but not at 200°C. No specimen failed at a load of 90% yield strength, but P110 steel could behave brittle when it was plastically deformed under gaseous hydrogen partial pressure of 1000 bar or more, at 25°C.

A summary of the properties of the specimens tested, and the test environment parameters collected from literature is provided in Table 3. The material properties and test parameters provide the domains of validity for the influences of relevant variables summarized.

Table 3 Properties of specimens tested and test environment parameters collected from literature for demonstrating HE

Steel Type	Brinell Hardness Number (MPa)	Yield strength (MPa)	Ultimate Tensile strength (MPa)	Microstructure	Hydrogen gas pressure (MPa)	T (°C)	Loading	Strain rate mm/min	Reference
S355	145	390	540	Ferritic-pearlitic	--	--	--	0.001 to 0.1	Alvarz et al. [47]
H8	285	790	860	Tempered martensite					
L80	--	632	736	--	10	25	90% yield strength	--	Eichinger et al. [48]
L110	--	901	1001		30				

Note:

“--”: not available

Hydrogen uptake thus the risk of HE is positively influenced by temperature and hydrogen pressure. Steel with a lower strength and lower hardness experiences a lower level of HE, through higher diffusion coefficient therefore less hydrogen concentration. High strength steel under high pressure in a low temperature could become brittle. A lower displacement rate provides more time for hydrogen to diffuse which leads to a higher level of HE. Increased loading may increase the hydrogen uptake, however the limiting conditions are not clear.

Table 4 summarizes the influences of relevant variables on the risk of HE. The summarized relation between the relevant variable and resulting risk of HE, is limited within the valid domain of the variable specified in the respective reference shown in Table 3.

Table 4 Summary of influences of relevant variables on the risk of HE

Reference	Strength	H ₂ pressure	T	Strain rate
Alvarz et al. [47]	Positive			Negative
Eichinger et al. [48]	Positive	Positive	Positive	

Note:

█ :not available

The strength of the steel, hydrogen gas pressure and operating temperature all contribute to an increased risk of HE in the material. Given the lower volumetric energy density of hydrogen compared to natural gas, the industry requires and favors higher design pressures and temperatures, necessitating the use of higher strength steel. As a result, HE is a critical challenge in hydrogen pipeline design.

4.2 HA-FCG

4.2.1 Introduction

The HA-FCG response in carbon steel can be affected by the test parameters and the material properties. The influences of the relevant variables on the HA-FCG response are analyzed and concluded from the literature reviewed in the following. Each conclusion is drawn based on the valid domain of the specific variable provided in the corresponding reference. Determined by the availability of the literature data, hydrogen gas pressure, load frequency, temperature, material strength and microstructure, load ratio R and test method are evaluated to draw conclusions of the relation between the influencing variables and the resulting HA-FCGR.

Table 5 summarizes the properties of the specimens tested, as well as the test environment parameters collected from literature. The material properties and test parameters provide the domains of validity for the influences of relevant variables summarized afterward.

Table 5 Properties of specimens tested and test environment parameters collected from literature for demonstrating HA-FCG

Steel Type	Grade	Yield strength (MPa)	Tensile strength (MPa)	Microstructure	Hydrogen gas pressure (MPa)	R	f (Hz)	T (K)	Purity of gaseous hydrogen (%)	Reference
Lower strength pipeline steel	SA 542 Class 2	568	820	martensitic	0.14	0.05 0.75	50	296	--	Suresh and Richie [20]
	SA 542 Class 3	400	610	bainitic	0.14	0.1	5	--		
						0.05 0.3 0.5 0.75	50	296		
	SA 516 Grade 70	327	496	ferritic-pearlitic	0.14	0.05 0.75	50	296		
6.9						0.15	0.1 to 10	--		
Pipeline	X 90	592	654	Ferrite and bainite	--	--	--	273 to 333	--	Xing et al. [45]
AISI-SAE	4130	1130	1600	--	0.0773	--	--	200 to 380	--	Nelson and Williams [44]
		1190	1310							
Pipeline	X46 to X80	400 to 565	531 to 600	Ferritic-pearlitic	0.6 21	0.1 0.5 0.7	1	Room	99.9999	Ronevich et al. [49]
Pressure vessel	SCM435	760 to 1158	947 to 1287	Quenched and tempered martensite Upper, lower bainite	20.7					
	SA372Gr. J				55					
	A372Gr. N				106					
	4340									
API	X52 vintage	490	643	Ferrite and pearlite	Mixed nitrogen with 3% hydrogen by volume at pressure of 3.45 MPa 20.7 MPa	0.1	1	Room	--	León-Cázares et al. [50]
API	5L X60	--	--	--	7 15	0.1	8	--	--	Faucon et al. [51]
Pipeline	X 80	595	705	--	0.2 MPa partial over total pressure 12 MPa of hydrogen and nitrogen 1.0 MPa over 12 MPa 8.0 MPa over 12 MPa	0.1	1	--	99.9999% hydrogen with 99.9999% nitrogen	An et al. [52]
API	5L X65	478	564	Banded ferrite-pearlite	21	0.5	1	295	99.9999	Ronevich et al. [53]
API	X52 vintage (1964)	325	526	--	5.5 34	0.5	0.01 0.1 1	--	99.9999	Slifka et al. [15]
	X52 modern (2011)	487	588							
	X70A (early 2000s)	509	609							
	X70B (early 2000s)	553	640							

API 5L	X52 Longitudinal	426	491	--	--	7 21 48	0.5	1	Room	99.999	Slifka et al. [54]
	X52 Transverse	436	504			1.7 7 21		0.1 1			
	X100 Longitudinal	705	803								
	X100 Transverse	794	827								
API	X52	--	--	--	--	21	0.5	1	295	99.9999	Ronevich et al. [55]
Type 304 austenitic stainless steel	--	--	--	Medal stable face-centered cubic	--	0.7	0.1	0.001 0.01 0.1 1 5	Room	99.9999	Matsunaga et al. [56]
Ductile cast iron	--	--	--	Ferrite/pearlite	--						
Low carbon steel	SM490B	360	540	--	--	0.1 0.7 10 45 90	0.1	0.001 0.01 0.1 1 10	--	99.9999	Yoshikawa et al. [34]
Low carbon steel	42CrMo4	622	710	Tempered martensite	--	35	0.1	0.1 1	Room	99.9999	Zafra et al. [57]
Low carbon steel	JIS-SM490B	360 537	--	--	--	0.7 90	0.1	1	298 to 423	--	Matsuoka et al. [58]
Low alloy steel	JIS-SCM435	767	--	--	--	0.7	0.1	0.001 0.01 0.1 1 5	Room	--	Matsuo et al. [59]
Annealed, low-carbon steel	JIS-SM490B	360	540	Ferrite and pearlite	--	0.1 to 90	0.1	0.001 to 10	363 and 423	99.999	Yamabe et al. [33]
API 5L	X52	--	--	Ferrite and pearlite	--	6.89 20.68	0.5	1	--	99.999	Amaro et al. [19]
	X100			Bainite and acicular ferrite	--	1.72 6.89 20.68					

Note:

--: not available

4.2.2 Pressure

An et al. [52] conclude that the presence of hydrogen accelerates the fatigue crack growth which subsequently reduces the total fatigue life of the tested X80 pipeline steel, at as low as 0.2 MPa hydrogen partial pressure over a total pressure of combined hydrogen and nitrogen that is 12.0 MPa. Figure 11 displays the test results. Crack initiation plays a more important role in fatigue lifetime reduction, when increasing the hydrogen partial pressure.

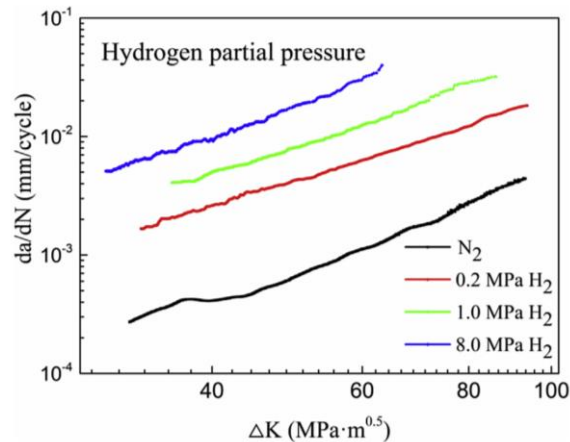


Figure 11 FCGR of X80 pipeline steel under different hydrogen partial pressure, with a total pressure of 12.0 MPa [52]

Slifka et al. [54] conducted fatigue tests according to ASTM E647-08 in load control. The hydrogen enhanced FCGR appear to correlate to pressure for the X100 steel but the correlation is not clear for the X52 steel.

All the tests carried out by Slifka et al. [15] were load controlled where ΔK increased as the crack grew. The results show sensitivity of FCGR to pressure and the X52 vintage steel shows the most sensitivity. It is determined that increasing hydrogen gas pressure increases the driving force for hydrogen diffusion. Sensitivity of FCGR to pressure appears to reach the maximum at the highest slope of $\frac{da}{dN}$ versus ΔK plots.

Ronevich et al. [49] conclude that partial pressure of hydrogen gas has a measurable effect on the FCGR at the lower crack growth rate, whereas the FCGR is independent of pressure at higher crack growth rate (close to $30 \text{ MPa}\sqrt{\text{m}}$), as illustrated in Figure 12. When $\frac{da}{dN}$ is high, the stress intensity perhaps becomes dominant.

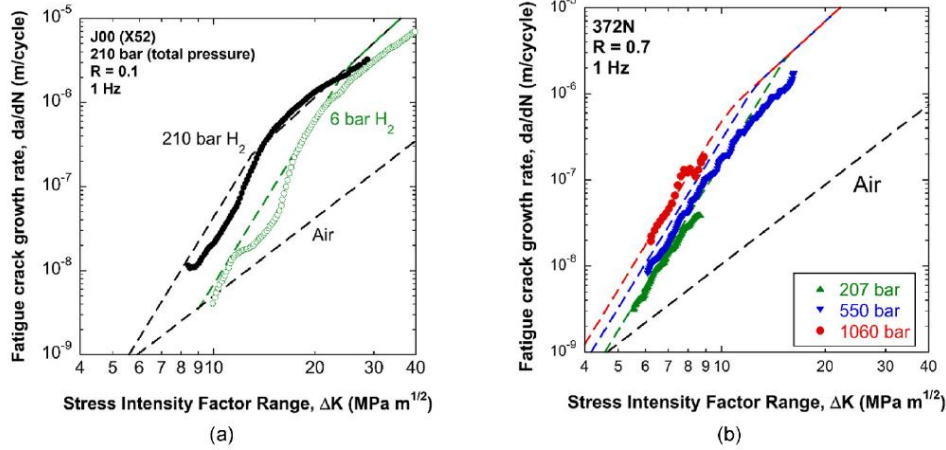


Figure 12 FCGRs determined from different experiments [49]

Yoshikawa et al. [34] and Yamabe et al. [33] discovered that the relative FCGR (RFCGR), $(da/dN)_{H_2}/(da/dN)_{air}$, obtained at $\Delta K = 30 \text{ MPa}\sqrt{\text{m}}$ under $f = 1 \text{ Hz}$, was nearly a constant at the pressure of gaseous hydrogen P_H (p_{H_2}) = 0.7 to 90 MPa. This finding effectively agrees with Ronevich et al. [49]. The curve obtained from the test results is shown in Figure 13.

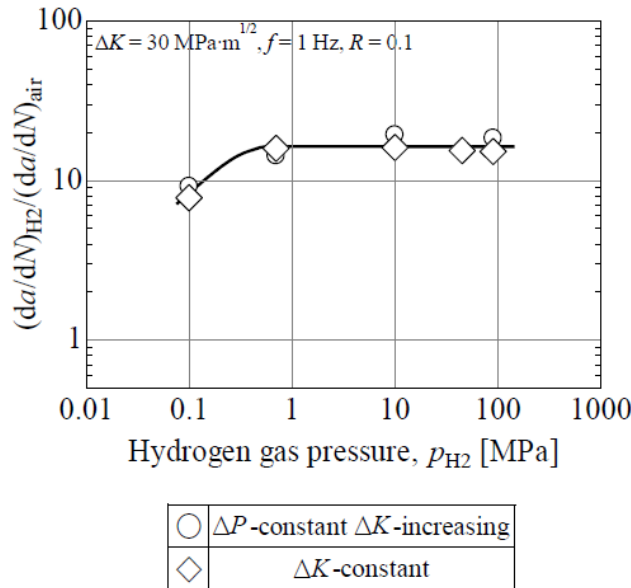


Figure 13 Relationship between the RFCGR and PH2 [34] [33]

Leon-Cazares et al. [50] observed faster crack growth rates under the higher pressure condition. It should be noted that ΔK only reached to approximately $27 \text{ MPa}\sqrt{\text{m}}$, as shown in Figure 14. It is possible that this level of stress intensity is not sufficient to become dominant, hence the FCGR is still dependent on the pressure of the gaseous hydrogen.

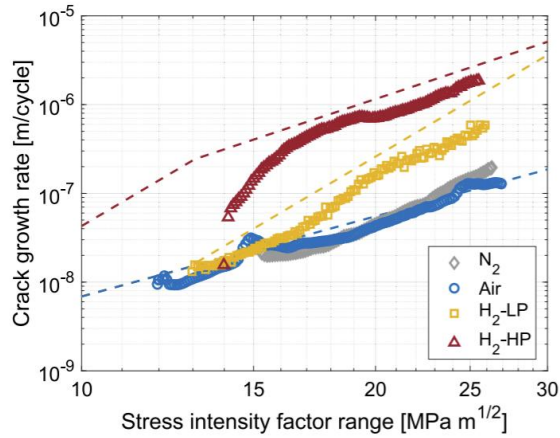


Figure 14 Crack growth rates determined from tests. The dashed lines correspond to design curves per API 579-1/ASME FFS-1 and ASME Code Case 220 [50]

Amaro et al. [19] performed load-controlled fatigue crack growth experiments per ASTM E647-08 [60]. The results indicate that the HA-FCGR increases with the increasing hydrogen pressure for values of ΔK below approximately $20 \text{ MPa}\sqrt{\text{m}}$. Above this value, the HA-FCGR converges regardless of the hydrogen pressure. Figure 15 displays the test results.

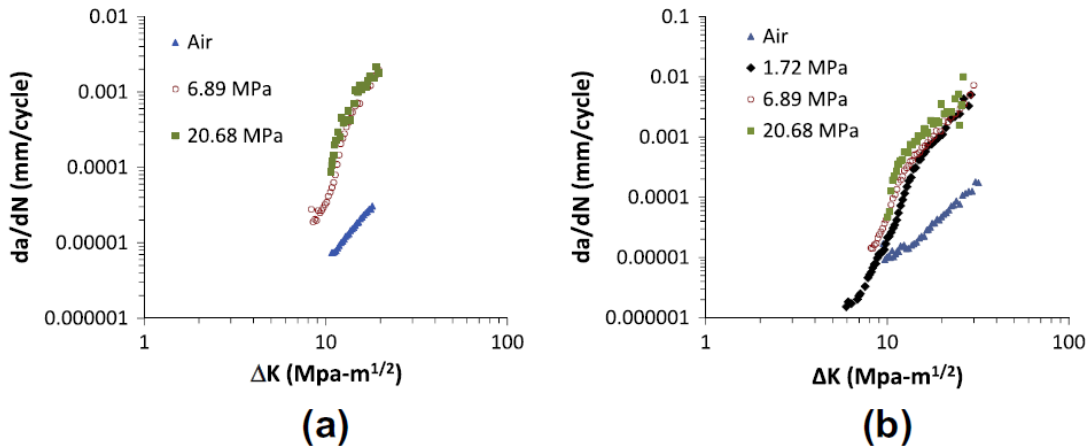


Figure 15 FCGR of (a) API X52 and (b) X100 steel as a function of hydrogen test pressure [19]

Comparing the results from Leon-Cazares et al. [50] and Amaro et al. [19], Leon-Cazares et al. investigated API X52 vintage pipeline steel, while Amaro et al. reviewed API 5L X52 modern pipeline steel and X100 steel. The pressure of the gaseous hydrogen varies between about 1 MPa and 20.7 MPa . X52 vintage steel does not show the HA-FCGR converging up to a ΔK value of $26 \text{ MPa}\sqrt{\text{m}}$, while X52 modern steel exhibits a convergence ΔK value of about $16 \text{ MPa}\sqrt{\text{m}}$. For the X100 steel tested by Amaro et al., it is possible that the HA-FCGR converges at ΔK value of $20 \text{ MPa}\sqrt{\text{m}}$, as shown in Figure 15.

Faucon et al. [51] extracted API 5L X60 pipe from a circumferential section of a subsea pipeline and conducted force-controlled fatigue tests. An in-situ gaseous hydrogen charging fatigue set-up was used. No significant influence of hydrogen on the fatigue crack initiation is shown, but the presence of hydrogen reduces the total lifetime by 37% which is attributed to the hydrogen accelerated fatigue crack growth, by a factor of four. No apparent difference in the number of load cycles until failure is observed between the pressure of 70 barg and 150 barg. It is postulated that the hydrogen saturation in the crack process zone is already reached under 70 barg. Analyzing Figure 16 from Faucon et al. [51], this statement applies to the weld metal specimens. Furthermore, even though the difference in the total number of load cycles until failure between specimens tested in 70 barg and 150 barg hydrogen gas is not apparent, a reduction at hydrogen pressure of 150 barg does occur. The magnitude of the total number of load cycles until failure is 10^5 . It is reasonable to assume that the FCGR of specimens tested in 150 barg hydrogen gas is distinctively higher than specimens tested in 70 barg hydrogen gas.

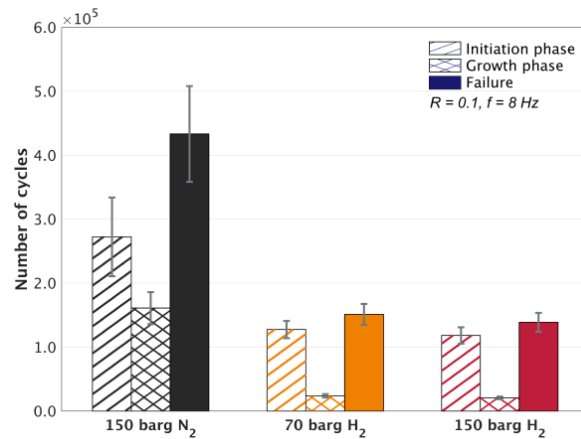


Figure 16 Bar graph of the number of loadcycles spent in the crack initiation, growth, and until failure, of the weld metal specimens [51]

The literature reviewed clearly demonstrates that the HA-FCGR is positively influenced by the pressure of the gaseous hydrogen. However, the convergence ΔK value above which the HA-FCGR is independent of hydrogen pressure provided by different studies varies slightly.

4.2.3 Load frequency

Matsuo et al. [59] performed fatigue tests at a constant $\Delta K \approx 25 \text{ MPa}\sqrt{\text{m}}$. The RFCGR gradually increases with the decreasing f from 5 Hz to 0.1 Hz, and reaches a maximum value at $f = 0.1 \text{ Hz}$. After reaching the maximum value, the RFCGR decreases with the decreasing f from 0.1 Hz to 0.001 Hz, and is nearly equal to that in air at f of 0.01 Hz and 0.001 Hz. Figure 17 presents the trend. When hydrogen accelerates the

FCGR, the slip bands are shown localized at the crack tip, and when hydrogen does not accelerate the FCGR, the slip bands are formed widely at the crack tip and the ductile striations are observed.

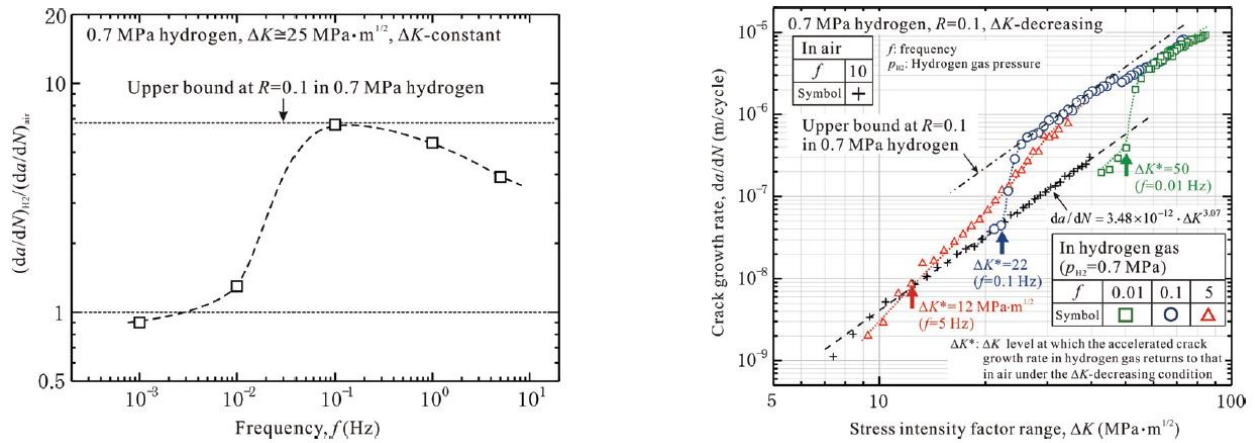


Figure 17 FCGR response in relation to f and ΔK [59]

Matsuo et al. [59] furthermore revealed that a ΔK value, representing the same implication as ΔK_{max}^T by Amaro et al. [7], at which the FCGR is noticeably accelerated by hydrogen, increases as f decreases from 5 Hz to 0.01 Hz, as shown in Figure 17.

All FCG tests performed by Matsunaga et al. [56] are in accordance with ASTM E647-08. To investigate the effect of internal hydrogen, hydrogen was saturated in the material and uniformly distributed from the surface to center, in the hydrogen-charged specimens. ΔK for the fatigue test was kept at $20 \text{ MPa}\sqrt{\text{m}}$. The results are shown in Figure 18.

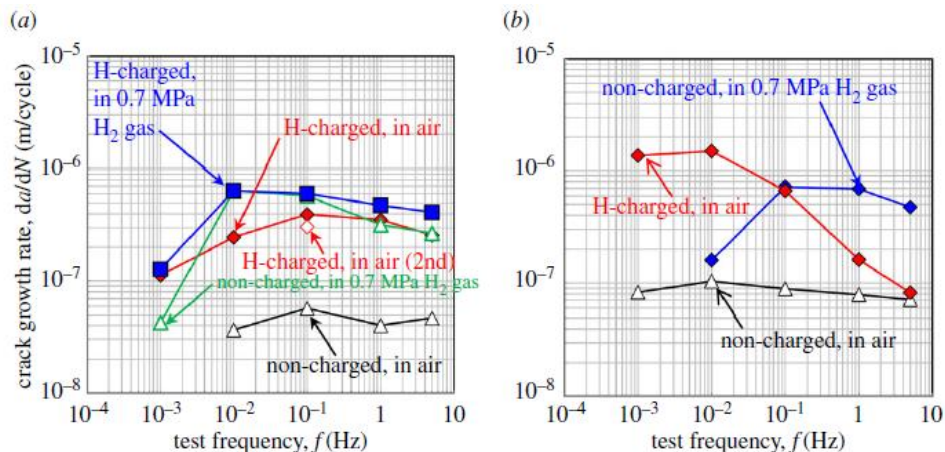


Figure 18 da/dN as a function of f , at ΔK of $20 \text{ MPa}\sqrt{\text{m}}$ (a) Type 304 stainless steel (b) Ductile cast iron [56]

Two types of steel tested both exhibit the peculiar frequency dependence of FCGR, in both the external and internal hydrogen tests. For hydrogen charged or non-charged specimens under 0.7 MPa hydrogen gas, the

ratio of hydrogen induced RFCGR, $(da/dN)_{H_2}/(da/dN)_{air}$, gradually increases with a decreasing f from 5 Hz, subsequently reaching a peak at f of 0.01 Hz for stainless steel and at f of 0.1 Hz for ductile cast iron. This is consistent with the results from Matsuo et al. [59], where the RFCGR increases with the decreasing f from 5 Hz reaching a peak at $f=0.1$ Hz, for low alloy steel JIS-SCM435 under 0.7 MPa hydrogen gas.

Slifka et al. [15] propose to handle the effect of loading frequency f on the FCGR by adding an analytical term where f is raised to an exponent to the phenomenological model introduced by Amaro et al. [22]. The loading frequency raised to a power of -0.1 is applied for the X70A steel, such as $\frac{da}{dN} \propto f^{-0.1}$, and lesser exponents are applied for the other three steels tested. It is hypothesized that a decreasing cyclic load frequency offers more time for hydrogen to diffuse to the crack tip. Since an increasing pressure increases the driving force for diffusion, a decrease in loading frequency might have a similar effect to an increase in gas pressure. The FCGR increases with a decreasing f from 1 Hz to 0.01 Hz, as shown in Figure 19. It is proposed that 34 MPa gas pressure essentially saturates the X52 vintage steel, because there is no apparent difference in FCGR with a decreasing load frequency.

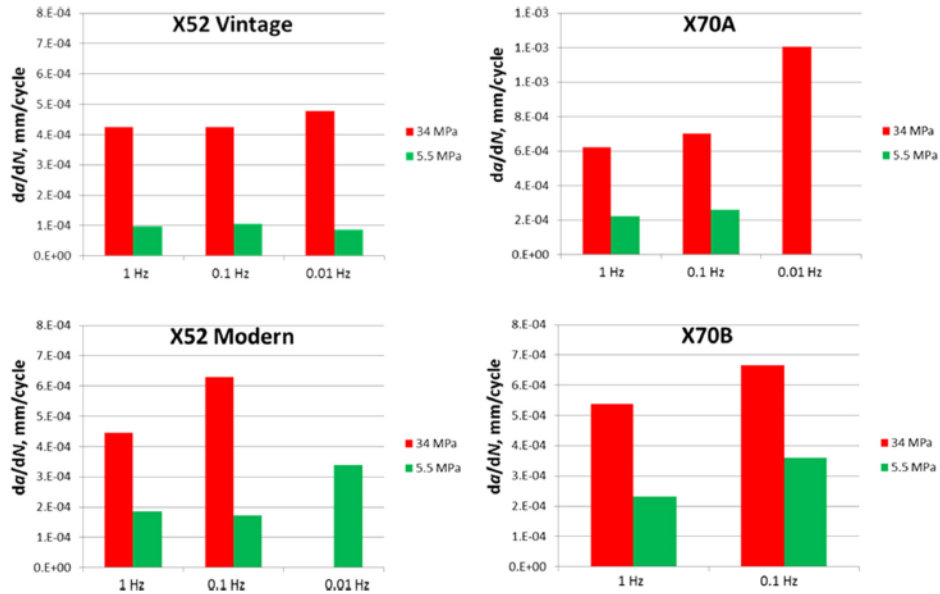


Figure 19 da/dN at ΔK of $14 \text{ MPa}\sqrt{\text{m}}$ for four materials [15]

From the literature reviewed, the HA-FCG response is negatively influenced by the increase of the cyclic load frequency. An exponent of -0.1 is proposed. The HA-FCG response peaked at a lower f value of 0.01 Hz in the tests conducted by Slifka et al. [15], comparing with the transition f value of 0.1 Hz from Matsuo et al. [59] and Matsunaga et al. [56]. It is worth noting that Matsuo et al. [59] and Matsunaga et al. [56] fatigue tested the specimens in 0.7 MPa hydrogen gas while Slifka et al. [15] pressurized the hydrogen gas to 5.5 MPa and 34 MPa for the tests. The results from Slifka et al. [15] under 34 MPa hydrogen gas show

a more pronounced trend. For X52 vintage steel under 5.5 MPa hydrogen gas, da/dN at f of 0.1 Hz is slightly higher than that at f of 0.01 Hz. Following Chapter 4.2.4 presents the research studies considering the effect of hydrogen gas pressure joint with cyclic load frequency on the FCGR.

4.2.4 Pressure joint with load frequency

Yoshikawa et al. [34] and Yamabe et al. [33] evaluate the FCGR response against the combination of the pressure of the hydrogen gas P_H (p_{H_2}) and the cyclic load frequency f . At P_H of 0.1, 0.7, and 10 MPa, the RFCGR gradually increases with a decrease in f , and peaks out. In the lower frequency regime, the FCG rapidly decelerates and becomes nearly equivalent to the FCGR in air. At P_H of 45 MPa, the hydrogen induced RFCGR monotonically increases with the decreasing f , and reaches a saturation value of about 30, at the upper limit around f of 0.01 to 0.001 Hz. At P_H of 90 MPa, the RFCGR monotonically increases with the decreasing f and an upper limit is not confirmed down to f of 0.0001 Hz. Figure 20 displays all above findings. It is inferred that a steep gradient of hydrogen at the crack tip causes a localization of plasticity which prevents crack tip blunting and sharpens the crack tip, which resembles the HELP mechanism of HE by Lynch [3]. This slip localization at the crack tip consequently enhances the hydrogen successive fatigue crack growth. As a result, $\frac{da}{dN}$ is increased. Yamabe et al. [33] conclude the HA-FCG acceleration is therefore accompanied by a localization of plastic deformation near the crack tip. It is proposed that such a peculiar dependence of HA-FCGR can be unified by a novel parameter $\sqrt{P_H f}$ which represents the gradient of hydrogen concentration at the crack tip.

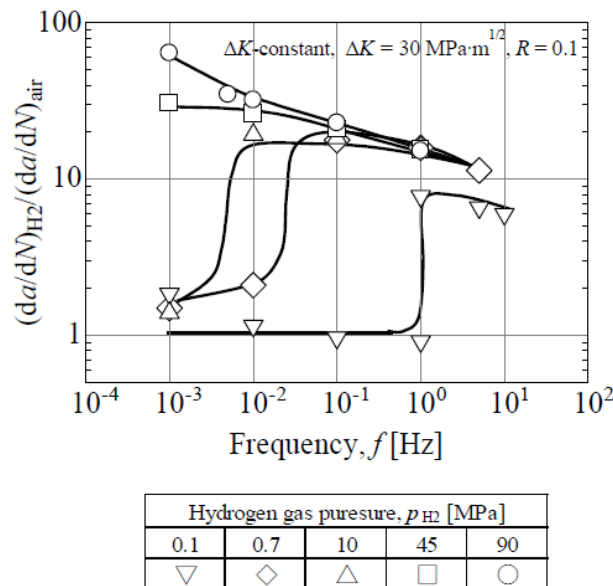


Figure 20 $(da/dN)_{Hz}/(da/dN)_{air}$ versus test frequency f [34] [33]

4.2.5 Temperature

Nelson and Williams [44] studied commercially obtained AISI-SAE 4130 low alloy steel. Specimens tested in 0.0773 MPa hydrogen gas exhibit a lowered threshold stress intensity factor for hydrogen fracture under lower temperature as shown in Figure 21, which is disadvantageous.

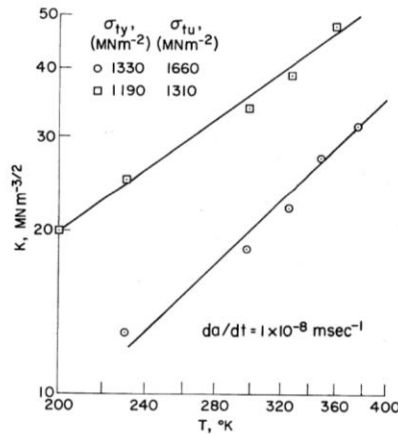


Figure 21 Effect of temperature on the threshold intensity factor for hydrogen assisted fracture of AISI-SAE 4130 low alloy steel in 0.0773 MPa hydrogen gas [44]

A review of factors affecting hydrogen induced degradation performed by Laureys et al. [61] explains the influence of temperature based on the hydrogen trapping model. At a temperature that is lower than room temperature, the diffusivity of hydrogen is too sluggish to substantially occupy traps. At a high temperature, the hydrogen mobility is enhanced and trapping is diminished.

Chen et al. [62] reproduced Figure 22 from Xing et al. [45] to illustrate the influence of temperature on HE. At a low temperature, hydrogen does not have sufficient mobility to facilitate the diffusion controlled HE mechanisms that lead to fracture, whereas at a high temperature, hydrogen is too mobile to be pinned by dislocations. HE reaches the maximum level at around room temperature of 313 K. This review aligns with the analysis from Laureys et al. [61].

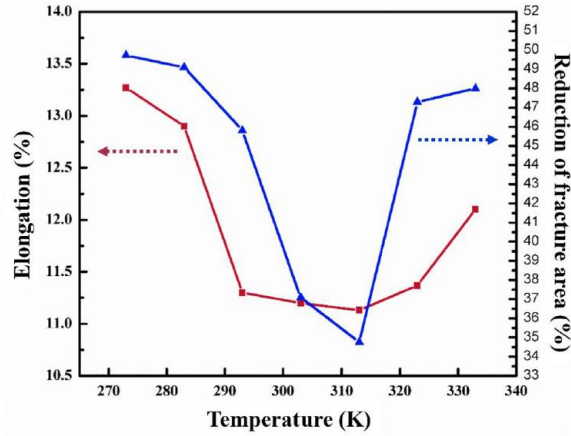


Figure 22 The extent of HE of hydrogen-charged ferritic/bainitic X90 pipeline steel specimens in terms of the reductions of elongation (red) and fracture area (blue) [62]

Matsuoka et al. [58] focused on relatively high ΔK regime ($\Delta K = 25 \text{ MPa}\sqrt{\text{m}}$) with the maximum acceleration of hydrogen enhanced fatigue crack growth (HEFCG). The HEFCG can be interpreted in terms of trap site occupancy, based on thermal equilibrium theory. The experimental results show that elevated temperatures mitigate HEFCG in hydrogen gas at 0.7 MPa , where the trap site occupancy is reduced. In contrast, in hydrogen gas at 90 MPa , the HEFCG is insensitive to temperature, as the trap site occupancy was insensitive to temperature. Figure 23 presents the test results. The temperature dependence of HEFCG can be successfully correlated to the trap-site occupancy when the binding energy is 47 kJ/mol , which corresponds approximately to the binding energy of a dislocation core. Therefore, hydrogen trapped at dislocations plays a critical role in the temperature dependence of HEFCG in low carbon steels, as illustrated in below Equation (59) and (60):

$$\frac{da}{dN} \propto \theta_x, \quad (59)$$

$$\frac{\theta_x}{1-\theta_x} = 3.08 \times 10^{-4} \sqrt{P_H \exp\left(\frac{bP_H}{R_g T}\right)} \exp\left(-\frac{3440}{T}\right) \exp\left(\frac{E_b}{R_g T}\right), \quad (60)$$

where θ_x is the hydrogen occupancy of trap sites, P_H is the pressure of hydrogen gas, b is a constant, T is the absolute temperature, and E_b is the binding energy of a trap site.

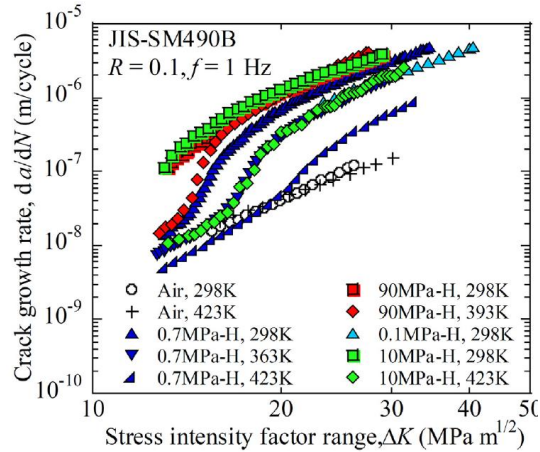


Figure 23 Effect of temperature on FCG curves [58]

Yamabe et al. [33] proved that the FCGR is accelerated in hydrogen gas. However, the FCGR is lower with higher temperatures. ΔK_{max}^T indicated in the model by Amaro et al. [7] shifts to a higher value with an increase in the test temperature, as shown in Figure 24.

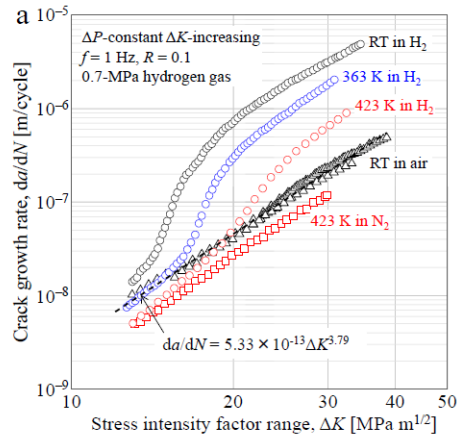


Figure 24 FCGR in elevated temperatures [33]

Increasing the temperature from room temperature, evidently mitigates the hydrogen enhancement of the fatigue response. However, the pressure of the gaseous hydrogen may play a role in the effect of temperature such that the FCGR becomes independent of the temperature under high hydrogen gas pressure.

4.2.6 Strength

Strength differences of more than two times have negligible effects on the FCGR in gaseous hydrogen for the pipeline and pressure vessel steels tested by Ronevich et al. [49], as shown in Figure 25. Analyses performed by Slifka et al. [15] show the expected decrease in ductility with increasing yield strength, but no corresponding change in the FCGR.

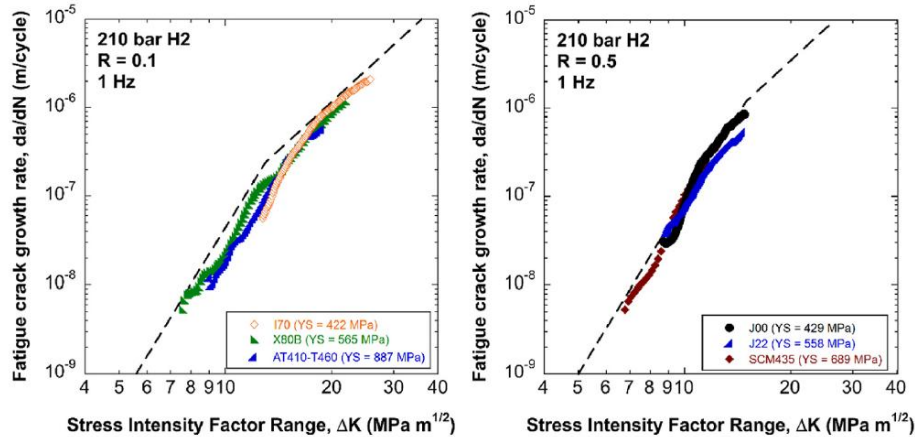


Figure 25 FCGR curves of pipeline and pressure vessel steels tested in 210 bar gaseous hydrogen at stress ratio R of 0.1 and 0.5 respectively [49]

4.2.7 Microstructure

Various microstructures exhibit similar FCGR differing by a factor of two to three at most in tests conducted by Ronevich et al. [49]. Ronevich et al. [53] discovered that fatigue cracks propagating perpendicular to the banded pearlite exhibit a growth rate nearly an order of magnitude lower than cracks propagating parallel to the pearlite. It is presumed that the crack tip branching shields the crack tip from applied stress and lowers the fatigue growth rate.

Yamabe et al. [33] carried out the fatigue tests under a constant load range. To estimate hydrogen diffusion properties at the crack tip, cold-rolled plates of JIS-SM490B with rolling ratios of 5% to 40% were tested, in addition to plates as received with no cold rolling. Hydrogen diffusivity, D , of the cold-rolled plates is lower due to lattice defects produced by the cold rolling. D decreases with an increase in the rolling ratio, and becomes constant when the rolling ratio is above 20%.

4.2.8 Load ratio R

Load ratio R is believed to be a significant influencing factor on the FCG. Unfortunately, fatigue tests were carried out under the same R value respectively in many research studies. Ronevich et al. [49] generated Figure 26 utilizing data from their studies and previous work. Even though no conclusion regarding the influence of R was proposed in the article, it can be drawn from Figure 26 that, the FCGR increases when increasing R from 0.1, to 0.5, then to 0.7, for pipeline and pressure vessel steels tested under 210 bar hydrogen gas with load frequency of 1 Hz. This figure indirectly displays the positive influence of the load ratio R on the HA-FCGR.

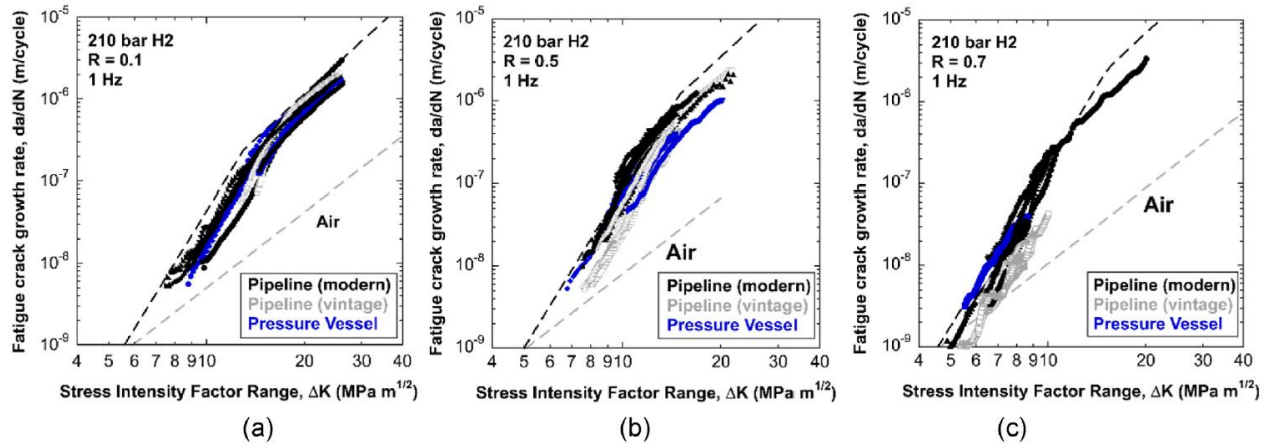


Figure 26 FCGR curves for pipeline and pressure vessel steels [29]

Demonstrating the effect of R on the threshold ΔK_0 and K_{max}^T , Suresh and Ritchie [20] also indirectly proved that a higher R value leads to a higher HA-FCGR, as shown in Figure 8.

4.2.9 Test method

Matsunaga et al. [33] observed that specimens tested in pressurized hydrogen gas exhibit higher FCGR than the pre-charged specimens do.

Zafra et al. [57] also performed ex-situ and in-situ fatigue tests. For ex-situ tests the specimens were pre-charged for 21 hours (until saturation) in a high-pressure reactor at 450 °C and at 19.5 MPa of pure gaseous hydrogen, subsequently fatigue tested in air. The FCGR of specimens tested under pressurized hydrogen gas is always greater than that of specimens pre-charged even at low ΔK values, where the hydrogen content in pre-charged specimens is the highest. Unlike in-situ results, the FCGR curves obtained from pre-charged specimens show a plateau of constant da/dN with increasing ΔK . The diminished acceleration of FCGR could be the result of progressive hydrogen egress at the crack faces. Similar fracture morphologies are observed in specimens tested under in-situ and ex-situ conditions, indicating that a critical hydrogen concentration is already attained in pre-charged specimens.

FCGRs of specimens that are fatigue tested in pressurized gaseous hydrogen are consistently greater. A pressurized gaseous hydrogen environment closely resembles the operating environment of the interior surface of the hydrogen pipeline. The fatigue response of steels tested in pressurized hydrogen gas, other than steels pre-charged with hydrogen, should indeed be the focus of this work.

4.2.10 Summary

Table 6 below summarizes the influences of relevant variables on the HA-FCG response of the specimens tested. It should be noted that the purity of the gaseous hydrogen in which the specimens are fatigue tested,

is not consistently available among all the literature referenced. As a result, this work excludes the influence of hydrogen gas purity on the fatigue response of the pipeline steel.

The summarized relation between the relevant variable and resulting HA-FCG response is limited within the valid domain of the variable specified in the respective reference, presented in Table 5.

Table 6 Summary of influences of relevant variables on HA-FCG response collected from literature reviewed

Reference	Pressure	f	Pressure & Frequency	T	Strength	Microstructure	R
Xing et al. [45]				Positive up to 313 K; negative beyond 313 K			
Nelson and Williams [44]				Negative			
Ronevich et al. [49]	Positive up to $\Delta K = 30$ $MPa\sqrt{m}$; converge above this $30 MPa\sqrt{m}$				Insensitive	Cracks propagate faster parallel to the banded pearlite	Positive
León-Cázares et al. [50]	Positive (data ends at $\Delta K = 27 MPa\sqrt{m}$)						
Faucon et al. [51]	Reduce measured life time						
An et al. [52]	Positive						
Slifka et al. [15]	Positive; most sensitive at the highest slope of da/dN versus ΔK	Positive to $f^{-0.1}$			Insensitive		
Slifka et al. [54]	X100 steel: positive						
Matsunaga et al. [56]		Negative					
Yoshikawa et al. [34]	Positive up to $\Delta K = 30$ $MPa\sqrt{m}$; converge above this ΔK		Positive to $(P_H f)^{1/2}$				
Matsuoka et al. [58]				Negative under 0.7 MPa pressure Insensitive under 90 MPa pressure			
Matsuo et al. [59]		Positive up to $f = 0.1$ Hz; negative above this value of f					
Yamabe et al. [33]	Positive up to $\Delta K = 30$ $MPa\sqrt{m}$; converge above this ΔK		Positive to $(P_H f)^{1/2}$	Negative		Increased lattice defects reduce hydrogen diffusivity	
Amaro et al. [19]	Positive up to $\Delta K = 20$ $MPa\sqrt{m}$; converge above this ΔK						

Note:

:not available

Detailed analyses leading to Table 6 are provided in Chapter 4.2.2 to 4.2.9.

A higher hydrogen gas pressure leads to a higher HA-FCGR, up to a convergence ΔK value. Above this ΔK , the HA-FCGR converges. Above room temperature, a higher temperature leads to a lower HA-FCGR, however up to a critical pressure. Above the critical hydrogen gas pressure, the HA-FCGR becomes

insensitive to temperature. The cyclic load frequency is shown to have a peculiar effect on the HA-FCGR. The HA-FCGR increases with a decreasing f , reaching a peak at the critical f value, then begins to decrease with the decreasing f . It is possible that the critical f value is affected by the pressure. The square root of the product of pressure and frequency, $\sqrt{P_H f}$, is demonstrated to positively influence the HA-FCGR.

It is reasonable to expect a demand to operate the hydrogen pipelines in high pressure, which leads to an increased FCGR enhanced by hydrogen. However, the associated high temperature environment may be carefully assessed to mitigate this enhancement. High and low cyclic load frequency regimes should be distinguished to estimate the predicted FCGR due to the proven peculiar effect.

Pressure, frequency, and temperature are the primary test parameters interconnected influencing the subsequent HA-FCG response. Consequently, they are considered to be the primary test parameters to be incorporated in the formulated functions to replace the empirical parameters included in the HA-FCGR predictive model.

4.3 Key threshold values

The shape of the HA-FCGR curve predicted by the model developed by Amaro et al. [7] is determined by the key threshold values, ΔK_{max}^T and ΔK_{tr} . ΔK_{max}^T and ΔK_{tr} define the transition points from the fatigue only regime to transient regime, and from the transient regime to steady-state regime, as shown in Figure 4.

Cyclic tests were performed at room temperature in air, dry gaseous nitrogen at pressure of 34.5 bar, mixed nitrogen with 3% hydrogen by volume at pressure of 34.5 bar, and gaseous hydrogen at pressure of 207 bar, by Leon-Cazares et al. [50]. Hydrogen starts to accelerate the crack growth rate above a threshold ΔK value of about $15 \text{ MPa}\sqrt{\text{m}}$. This ΔK represents the same implication as ΔK_{max}^T from the model by Amaro et al. [7], which is the transition point from region A to region B, as shown in Figure 4. Below this threshold value, hydrogen shows no effect in accelerating the crack growth. It should be noted from Figure 14 that ΔK_{max}^T of $15 \text{ MPa}\sqrt{\text{m}}$ fits well for the low hydrogen pressure tests. For the high pressure tests, ΔK_{max}^T may be reduced from extrapolation. However, the authors do not make a specific distinction.

Faucon et al. [51] observed trans-granular and ductile fracture path of the steel in nitrogen. In hydrogen, similar behavior was observed until the onset of HA-FCG that occurred at ΔK of $15 \text{ MPa}\sqrt{\text{m}}$. Above this value, the fracture surface transitions to a mixed mode of trans-granular and inter-granular quasi-cleavage fracture. This ΔK_{max}^T value agrees with the findings from Leon-Cazares et al. [50]. However, no figure is provided in the article for the similarities to be verified.

Fatigue testing by Ronevich et al. [55] was performed under constant load amplitude condition with ΔK increasing as the crack grew. Specimens tested in hydrogen exhibit accelerated fatigue crack growth to more than 40 times greater than rates in air for $\Delta K > 15 \text{ MPa}\sqrt{\text{m}}$. The onset of HA-FCG occurs at low ΔK values (e.g. $6\text{-}8 \text{ MPa}\sqrt{\text{m}}$, if the data is extrapolated to the curve in air). As shown in Figure 27, ΔK_{max}^T is $6\text{-}8 \text{ MPa}\sqrt{\text{m}}$ concluded from test results. The overall FCGR trends observed in this X52 pipeline steel are characteristic of ferritic pipeline steels previously tested in hydrogen gas.

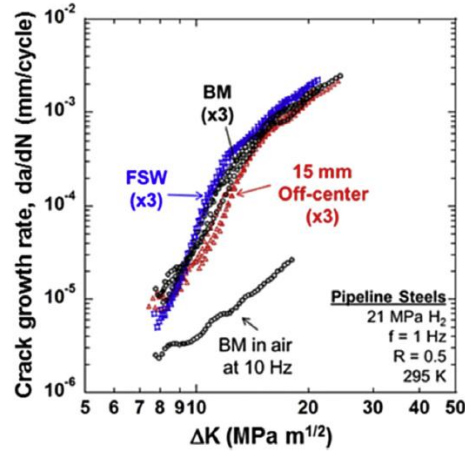


Figure 27 FCG of X52 steel pipe tested at base medal, center of friction stir weld, and 15mm off-center [55]

Test results from Ronevich et al. [55] with load ratio R equal to 0.5, and Leon-Cazares et al. [50] with R of 0.1, show that an increased R value leads to a decreased ΔK_{max}^T .

Suresh and Ritchie [20] demonstrated that ΔK_{max}^T is sensitive to frequency, load ratio and pressure, which can be a reason why ΔK_{max}^T varies with different test parameters. Their rest results as well agree with that an increasing R decreases ΔK_{max}^T .

Observed from the test results by Slifka et al. [54], there is a transition ΔK of $11 \text{ MPa}\sqrt{\text{m}}$ and $15 \text{ MPa}\sqrt{\text{m}}$ for X52 steel and X100 steel, respectively. Before the transition, the FCGR in hydrogen is characterized by a slope greater than that in air, possibly due to increased hydrogen concentration as hydrogen diffuses to the crack driven by high stress. After the transition, the slope of the FCGR as a function of ΔK is similar to that in air, but with a rate 1 to 2 order of magnitude higher. Perhaps the hydrogen concentration is saturated in the crack process zone at such a high level of stress intensity. This is the transition ΔK_{tr} between transient regime (region B) and steady-state regime (region C) in Figure 4. The fracture surface transitions from inter-granular to mostly trans-granular fracture as ΔK increases.

Amaro et al. [19] established a ΔK_{tr} of $13 \text{ MPa}\sqrt{\text{m}}$ for X52 and X100 steels, as shown in Figure 15.

Fatigue tests performed by Yoshikawa et al. [34] and Yamabe et al. [33] revealed when ΔK is less than $20 \text{ MPa}\sqrt{\text{m}}$, the FCG acceleration increases with an increase in ΔK . When ΔK is greater than $20 \text{ MPa}\sqrt{\text{m}}$, the $\frac{da}{dN} - \Delta K$ curves in hydrogen gas are parallel to the curves in air. In other words, the value of ΔK_{tr} [41][67] is $20 \text{ MPa}\sqrt{\text{m}}$, as shown in Figure 28.

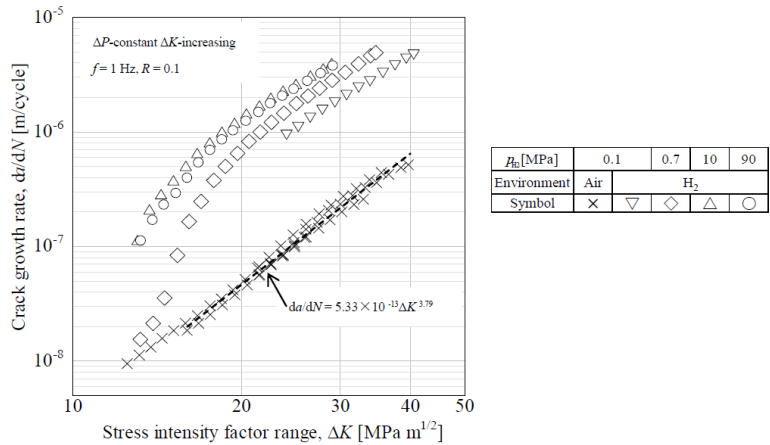


Figure 28 Relationship between $\frac{da}{dN}$ and ΔK [34] [33]

The load ratio R is 0.5 for the fatigue tests conducted by Slifka et al. [54] and Amaro et al. [19], while Yoshikawa et al. [34] and Yamabe et al. [33] applied R of 0.1 in their tests. The test results demonstrate that an increased R value leads to a decreased ΔK_{tr} .

The values of ΔK_{max}^T and ΔK_{tr} discussed above are summarized in Table 7.

Table 7 Summary of ΔK_{max}^T and ΔK_{tr} collected from literature reviewed

Reference	ΔK_{max}^T ($\text{MPa}\sqrt{\text{m}}$)	ΔK_{tr} ($\text{MPa}\sqrt{\text{m}}$)
Suresh and Ritchie [20]	SA 542 Class 2 steel: 20 with R equal to 0.1 SA 542 Class 3 steel: 12, 17, 22 with R equal to 0.5, 0.3, 0.05 SA 516 Grade 70 steel: 10 with R equal to 0.15	
León-Cázarez et al. [50]	15	
Faucon et al. [51]	15	
Slifka et al. [54]		X52 steel: 11 X100 steel: 15
Ronevich et al. [55]	6 to 8	
Yoshikawa et al. [34]		20
Yamabe et al. [33]		20
Amaro et al. [19]		13

Note:

█ :not available

Not included in the model by Amaro et al. [7], but implied in the EAC model by Anderson [9], another key threshold stress intensity range ΔK_0 is presented by Suresh and Ritchie [20], and Murakami and Ritchie [63]. The crack growth rates of the tested steel specimens in hydrogen are experimentally undetectable

below ΔK_0 . ΔK_0 in air can be close to 50% higher than ΔK_0 in dry hydrogen, but this significant difference is only evident when the load ratio R is low, e.g. 0.05. A test by Suresh and Ritchie [20] demonstrated that the value of ΔK_0 is the same in both air and hydrogen when R is 0.75, shown in Figure 8. ΔK_0 in hydrogen with R value of 0.75, is 30% lower than the ΔK_0 in hydrogen with R value of 0.05. An increased R decreases ΔK_0 . This ΔK_0 value is critical for extending the model by Amaro et al. [7] by including the near-threshold corrosion fatigue behaviour of steels. A list of ΔK_0 values obtained by Suresh and Ritchie [20] is summarized in Table 8.

Table 8 Summary of ΔK_0 [20]

Steel	Yield strength (MPa)	R	f (Hz)	Dry hydrogen gas pressure (MPa)	Temperature (°C)	ΔK_0 (MPa \sqrt{m}) approximation
SA 542 Class 2	275	0.75	50	0.14	23	2.7
		0.05	50	0.14	23	4.6
SA 542 Class 3	345	0.75	50	0.14	23	3.1
		0.05	50	0.14	23	5.3
SA 516 Grade 70	260	0.75	50	0.14	23	3.8
		0.15	50	0.14	23	5.7

The key threshold values can be utilized to update the HA-FCGR predictive model by connecting physical meanings of the threshold values to the empirical parameters in the model.

5 A Tri-Linear HA-FCGR model

A predictive model for HA-FCGR consisting of three linear regions is proposed in this chapter. Initially, an effort is made to eliminate the need for parameters with complex units. A Tri-Linear format for the predictive model defined by two knee points is introduced next. Applying the proposed Tri-Linear format for the HA-FCGR prediction model, the key values associated with the two knee points are optimized implementing the Nonlinear Least Square method in MATLAB, based on the fatigue test results digitized from the referenced literature.

5.1 Handling units

Many of the predictive models introduced in Chapter 3 follow the format of Paris' relation represented by Equation (8): $\left(\frac{da}{dN}\right)_{air} = a_{air} \cdot \Delta K^{B_{air}}$. The unit of da/dN is length per cycle. $mm/cycle$ is selected to be the unit for da/dN in this work. The unit of ΔK is $MPa\sqrt{m}$. This indicates a complex unit is required for a_{air} with a dimensionless B_{air} , that is $10^{-3}MPa^{-B_{air}}m^{1-\frac{B_{air}}{2}}$. Units of the fitted parameters required for the predictive model per Equation (17) in ASME B31.12 2023 [8] are presented in Chapter 3.2.2.

Different approaches have been employed by researchers to simplify the unit of the multiplier a_{air} .

Golahmar et al. [17] introduced a reference stress intensity factor K_r that is expressed as $\sqrt{\frac{G_c E}{(1-\nu)^2}}$, where G_c is the fracture toughness of the material, and E is the Young's modulus. ΔK is subsequently normalized by K_r so that the crack growth rate is expressed in terms of $\Delta K/K_r$ that is dimensionless. Amsterdam et al. [64] introduced multiple transition points on the FCGR curve, to accommodate the multiple slopes due to the different micro-mechanisms of fatigue crack growth associated with the plasticity or plastic dissipation at the crack tip. In each linear region, $\frac{da}{dN} = \left(\frac{da}{dN}\right)_{TP} \left(\frac{\Delta K}{\Delta K_{TP}}\right)^{n_i}$, where $\left(\frac{da}{dN}\right)_{TP}$ and ΔK_{TP} are the FCGR and stress intensity factor range at the pivot point, and the exponent n_i changes for different linear regions.

The collected fatigue test results of steel in gaseous hydrogen consist of values of $\frac{da}{dN}$ and ΔK . To not alter the shape of the HA-FCGR curves necessarily, ΔK is normalized by $1 MPa\sqrt{m}$ in this work. $\left(\frac{da}{dN}\right)_{air}$ thus becomes $a_{air} \cdot (\Delta K/1)^{B_{air}}$. With B_{air} being dimensionless, the unit of a_{air} is simply the same as the unit of $\left(\frac{da}{dN}\right)_{air}$ that is $mm/cycle$.

5.2 A Tri-Linear format

The predictive model developed by Amaro et al. [7], of which the simplified version is implemented in ASME B31.12 2023 [8], includes six fitted parameters. Additionally, it adopts the springs-in-parallel model structure so that $\left(\frac{da}{dN}\right)_{PH}$ and $\left(\frac{da}{dN}\right)_{\Delta K}$ compete with one another. The model is flexible and viable. However, six parameters are required to be fitted by a minimum of three sets of experimental results.

Many other models introduced in Chapter 3.4 evolve around the Paris' law equation, with a multiplier added to account for the effect of hydrogen enhancement. Attempts have been made to incorporate hydrogen pressure and cyclic load frequency into different models.

It is commonly acknowledged that in Region A defined by Amaro et al. [7] shown in Figure 4, the HA-FCGR is effectively equivalent to the FCGR of steel in air, and in Region C, the slope of the HA-FCGR curve closely follows the slope of the FCGR curve of steel in air. The HA-FCGR curves from literature based on previous fatigue test results presented in Chapter 4.2 further support these statements. Therefore, in this work, the HA-FCGR of Regime A is assumed to be identical to the FCGR of steel tested in air, and the exponent of ΔK in Regime C is assumed to be the same as the exponent of ΔK in Regime A.

The onset of hydrogen enhancement on the HA-FCGR curve, labeled as ΔK_{max}^T shown in Figure 4 by Amaro et al. [7], hereafter is specified as ΔK_1 . The point on the HA-FCGR curve representing the saturation of hydrogen enhancement, termed as ΔK_{tr} and $\left(\frac{da}{dN}\right)_{tr}$ shown in Figure 4, are specified as ΔK_2 and $\left(\frac{da}{dN}\right)_2$ hereafter. A HA-FCGR curve can be fully determined if the three values associated with the two knee points of the HA-FCGR curve, namely ΔK_1 , ΔK_2 and $\left(\frac{da}{dN}\right)_2$, can be quantified.

The updated predictive model becomes a step function as follows:

$$\frac{da}{dN} = \begin{cases} \mathbf{a}_{air} \cdot \Delta K^{B_{air}}, & \Delta K \leq \Delta K_1 \\ \left(\frac{da}{dN}\right)_1 \cdot \left(\frac{\Delta K}{\Delta K_1}\right)^{\frac{\log\left[\left(\frac{da}{dN}\right)_2 / \left(\frac{da}{dN}\right)_1\right]}{\log(\Delta K_2 / \Delta K_1)}}, & \Delta K > \Delta K_1 \text{ and } \Delta K < \Delta K_2 \\ \left(\frac{da}{dN}\right)_2 \cdot \left(\frac{\Delta K}{\Delta K_2}\right)^{B_{air}}, & \Delta K \geq \Delta K_2 \end{cases} \quad (61)$$

where $\left(\frac{da}{dN}\right)_1 = \mathbf{a}_{air} \cdot \Delta K_1^{B_{air}}$.

This proposed Tri-Linear HA-FCGR model hence aims to capture regime dependent behaviour via two derived pivot points.

5.3 Curve fitting to experimental results

The HA-FCGR curves collected from literature are digitized first. The updated format of the predictive model presented in Chapter 5.2 is followed. For each curve, a_{air} and B_{air} are obtained from the FCGR curve of the same steel tested in air provided along with the HA-FCGR curve in the literature. The values of ΔK_1 , ΔK_2 and $\left(\frac{da}{dN}\right)_2$ for each curve are optimized by the Nonlinear Least Square method implemented in MATLAB. The total residual error of the Nonlinear Least Square optimization that is the sum of the squared differences between the logarithms of the modeled values and the experimental data, is expressed as:

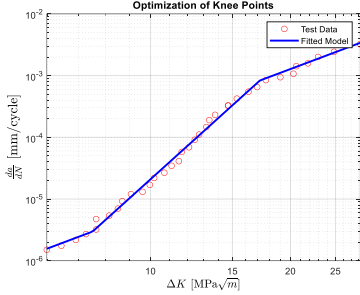
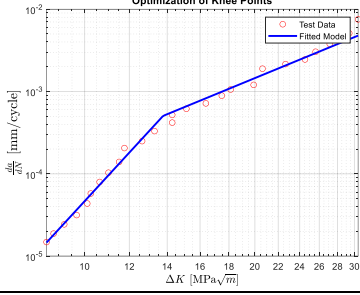
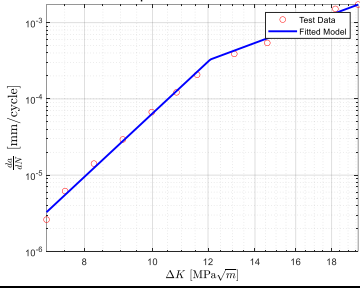
$$ER = \sum_{i=1}^{N_{data}} \left[\log_{10} \left(\frac{da}{dN} \right)_{data_i} - \log_{10} \left(\frac{da}{dN} \right)_{model_i} \right]^2, \quad (62)$$

where N_{data} is the number of data points in the fatigue test results, $\left(\frac{da}{dN}\right)_{data_i}$ is the i^{th} observed crack growth rate in the fatigue test, and $\left(\frac{da}{dN}\right)_{model_i}$ is the i^{th} modeled crack growth rate.

In this study, all available experimental data are used to determine the key values of the HA-FCGR curve. Physically motivated equations are then established to relate these key values to test parameters. This study aims to develop a mechanistic and interpretable framework rooted in fracture mechanics and material science; therefore, it is appropriate to use the full dataset. This approach ensures that the derived relationships are grounded in observed behaviour across the entire range of data. Future work could expand on this by validating the proposed model equations with independent datasets as they become available.

The test parameters, material properties, optimized knee points and the ER of the Nonlinear Least Square optimization of each HA-FCGR curve along with the referenced literature, are presented in below Table 9.

Table 9 Summary of fitted Tri-Linear HA-FCGR curves from literature

Reference	Figure	Material	P_H (MPa)	R	f (Hz)	T (K)	σ_y (MPa)	a_{air}	B_{air}	ΔK_1 (MPa \sqrt{m})	ΔK_2 (MPa \sqrt{m})	$\left(\frac{da}{dN}\right)_2$ (mm/cycle)	ER	Fitted Tri-Linear HA-FCGR curve and experimental data points
Amaro et al. [22]	Fig. 8	API-5L X100	1.7	0.5	1.00	293	689	9.90E-09	2.83	7.50	17.19	8.32E-04	0.1683	
Amaro et al. [22]	Fig. 8	API-5L X100	6.9	0.5	1.00	293	689	9.90E-09	2.83	6.59	13.77	5.05E-04	0.1148	
Drexler et al. [65]	Fig. 7	X70A	34.0	0.5	1.00	293	509	2.00E-09	3.42	6.14	12.09	3.29E-04	0.0288	

Drexler et al. [65]	Fig. 7	X70B	34.0	0.5	1.00	293	553	4.00E-09	3.31	6.37	11.47	2.71E-04	0.0393	
Matsuo et al. [59]	Fig. 2	JIS-SCM435	0.7	0.1	0.10	293	767	3.48E-09	3.07	22.24	24.29	3.03E-04	0.4842	
Matsuo et al. [59]	Fig. 2	JIS-SCM435	0.7	0.1	0.01	293	767	3.48E-09	3.07	50.05	53.94	2.67E-03	0.2920	
Matsuoka et al. [58]	Fig. 1	JIS-SM490B	0.7	0.1	1.00	298	360	3.00E-10	3.96	12.52	17.76	4.07E-04	0.1043	

Matsuoka et al. [58]	Fig. 1	JIS-SM490B	0.7	0.1	1.00	363	360	3.00E-10	3.96	15.40	19.97	3.72E-04	0.0818	
Matsuoka et al. [58]	Fig. 1	JIS-SM490B	10.0	0.1	1.00	423	360	5.00E-09	3.04	16.16	20.89	5.48E-04	0.2326	
Matsuoka et al. [58]	Fig. 1	JIS-SM490B	90.0	0.1	1.00	393	360	3.00E-10	3.96	12.34	16.83	5.39E-04	0.1531	
Ronevich et al. [55]	Fig. 4	X52	21.0	0.5	1.00	295	360	7.00E-09	2.78	5.84	14.11	5.45E-04	0.0751	

Ronevich et al. [66]	Fig. 5	X100	21.0	0.5	1.00	295	690	1.00E-08	2.87	5.18	12.98	5.39E-04	0.0630	
Ronevich et al. [49]	Fig. 4	J00	21.0	0.1	1.00	293	429	1.00E-08	3.11	8.81	15.21	5.07E-04	0.1685	
Saxena an Nibur [67]	Fig. 3	Class 70	10.0	0.1	1.00	295	771	3.00E-09	3.29	9.33	20.12	4.75E-04	0.0202	
Slifka et al. [54]	Fig. 6	X100	1.7	0.5	1.00	293	705	9.84E-09	2.83	7.15	13.01	5.77E-04	0.1281	

Slifka et al. [54]	Fig. 6	X100	7.0	0.5	1.00	293	705	9.84E-09	2.83	6.01	11.45	4.58E-04	0.0881	
Slifka et al. [54]	Fig. 8	X100	7.0	0.5	0.10	293	705	9.84E-09	2.83	5.94	11.39	6.80E-04	0.0525	
Slifka et al. [54]	Fig. 7	X52	7.0	0.5	1.00	293	426	2.43E-09	3.31	6.09	11.99	7.01E-04	0.2200	
Slifka et al. [15]	Fig. 12	X52 vintage	5.5	0.5	1.00	293	325	3.00E-09	3.16	8.43	19.70	6.84E-04	0.7126	

Slifka et al. [15]	Fig. 12	X52 vintage	34.5	0.5	1.00	293	325	3.00E-09	3.16	7.59	12.04	3.79E-04	0.4331	
Slifka et al. [15]	Fig. 12	X52 modified	5.5	0.5	1.00	293	487	8.00E-10	3.72	5.80	15.64	4.12E-04	0.2924	
Slifka et al. [15]	Fig. 16	X52 vintage	5.5	0.5	0.10	293	325	3.00E-09	3.16	8.99	18.35	8.24E-04	0.0146	
Slifka et al. [15]	Fig. 13	X70B	5.5	0.5	1.00	293	553	6.00E-09	3.10	9.51	14.27	4.79E-04	0.8486	

Slifka et al. [15]	Fig. 17	X70A	34.5	0.5	0.10	293	509	4.00E-09	3.19	6.02	12.64	5.23E-04	0.0259	
Yamabe et al. [33]	Fig. 5	JIS-SM490B	0.7	0.1	1.00	293	360	5.33E-10	3.79	12.60	17.78	4.59E-04	0.1642	
Yamabe et al. [33]	Fig. 5	JIS-SM490B	0.7	0.1	1.00	363	360	5.33E-10	3.79	15.49	20.13	3.83E-04	0.0693	
Yamabe et al. [33]	Fig. 5	JIS-SM490B	0.7	0.1	1.00	423	360	5.33E-10	3.79	19.13	26.11	3.84E-04	0.2657	

Yoshikawa et al. [34]	Fig. 5	JIS-SM490B	0.7	0.1	1.00	293	360	5.33E-10	3.79	12.53	18.11	4.76E-04	0.0556	
Zafra et al. [57]	Fig. 11 (Ronevich 2016)	X65	21.0	0.5	1.00	293	450	5.00E-09	3.10	5.50	14.53	5.74E-04	0.0332	

6 Fracture Mechanisms

In this chapter, the fracture mechanisms of the three regions categorized by Amaro et al. [7] are reviewed. Fracture surface images from the literature are presented to support the proposed mechanisms. It is critical to identify the dominant fracture mechanism in each region in order to quantify the three key values, namely ΔK_1 , ΔK_2 and $\left(\frac{da}{dN}\right)_2$, associated with the two knee points on the HA-FCGR curve, shown in Figure 29.

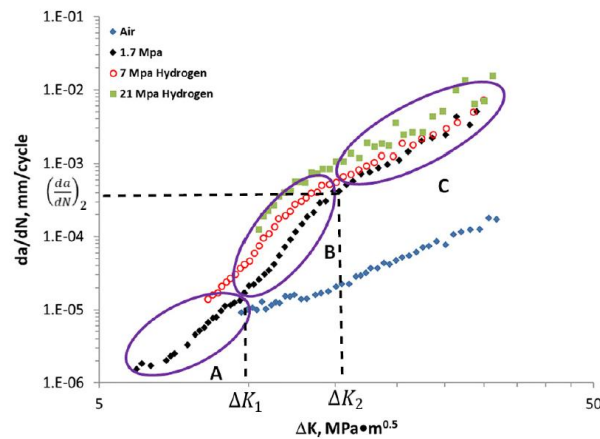


Figure 29 Typical HA-FCGR results of API X100 steel delineated into three regions: A, B and C. All data is generated at a frequency of 1 Hz and load ratio R of 0.5 [7]

6.1 Region A

The hydrogen assisted fatigue crack surface in Region A closely matches what is produced in air.

Amaro et al. [22] presented fatigue surface of X100 steel pre-cracked in laboratory air, shown in Figure 30.

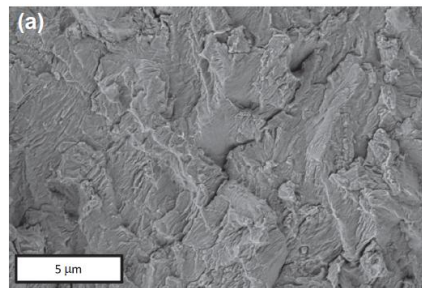


Figure 30 Fatigue surface of X100 steel pre-cracked in laboratory air [22]

Slifka et al. [54] also presented fatigue surface of X100 steel pre-cracked on a different scale, shown in Figure 31.

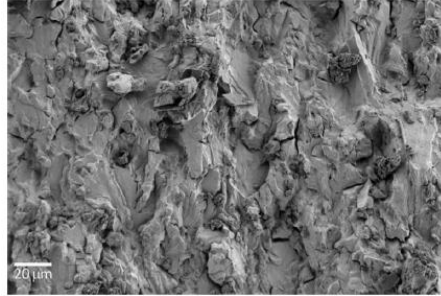


Figure 31 Fatigue surface of X100 steel pre-cracked [54]

The fatigue surface of X100 steel pre-cracked in air exhibits mainly ductile trans-granular character. It is worth noting that the applied ΔK to pre-crack the specimen is not provided.

Amaro et al. [7] presented fatigue-crack surfaces of Region A for three materials tested in gaseous hydrogen under 1 Hz frequency and load ratio of 0.5, shown in Figure 32. Failures are seen predominantly ductile trans-granular fracture.

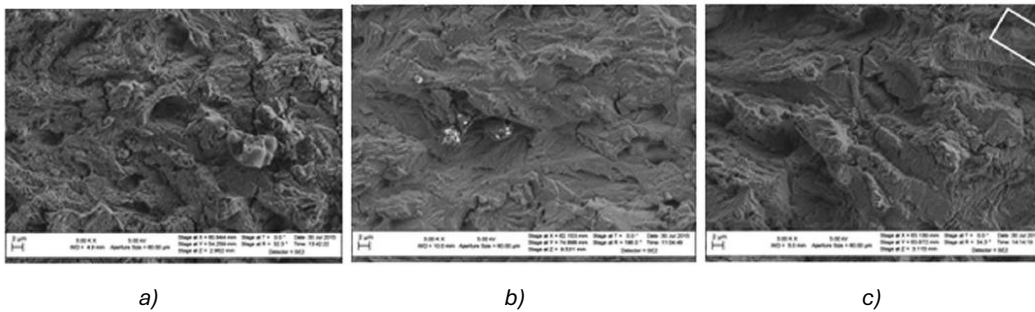


Figure 32 Fatigue-crack surfaces of Region A for a) X52 modern steel under 5.5 MPa hydrogen, b) X52 Alloy J steel under 6.9 MPa hydrogen, and c) X52 vintage steel under 5.5 MPa hydrogen [7]

6.2 Region B

Regime B is defined as the transient regime by Amaro et al. [7]. The HA-FCGR rapidly rises due to the hydrogen enhancement. Brittle failure is expected in this region. Suresh and Ritchie [20] presented fracture surface of $2\frac{1}{4}$ Cr-1Mo steel tested in dry hydrogen at $R = 0.3$ and frequency of 50 Hz. Figure 33 below provides the HA-FCGR curve.

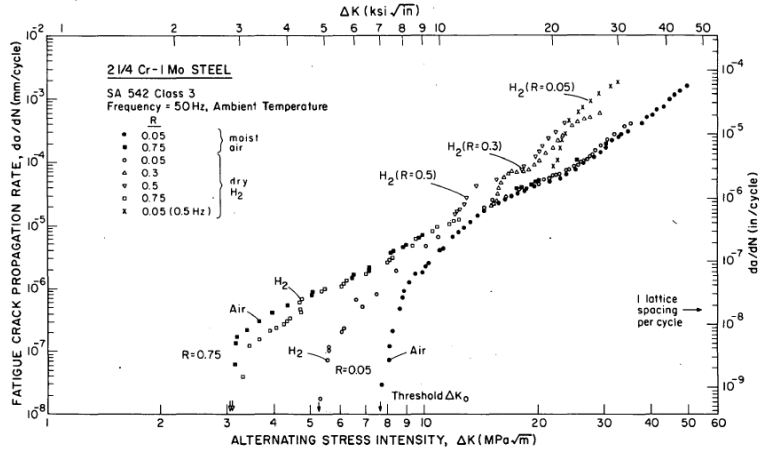


Figure 33 FCGR curve of SA 542 Class 3 steel [20]

At $\Delta K = 14 \text{ MPa}\sqrt{m}$, the fracture surface in hydrogen shown in Figure 34 exhibits mainly trans-granular failure with a small fraction of inter-granular facets. This can be considered a transition from Region A to Region B, based on the HA-FCGR curve in Figure 33.

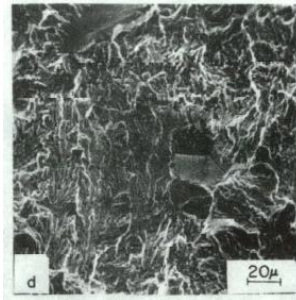


Figure 34 Mechanisms of fatigue crack growth in the mid-growth rate regime for bainitic $2\frac{1}{4}\text{-Cr-1Mo}$ steel tested at $R = 0.3$ and frequency of 50 Hz [20]

At $\Delta K = 20 \text{ MPa}\sqrt{m}$ in Region B shown in Figure 33, the fracture surface shown in Figure 35 exhibits clearly brittle inter-granular failure.

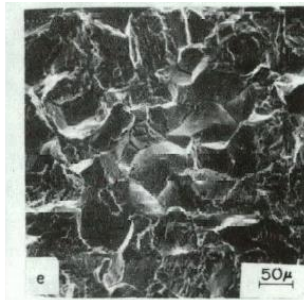


Figure 35 Mechanisms of fatigue crack growth in the high-growth rate regime for bainitic $2\frac{1}{4}\text{-Cr-1Mo}$ steel tested at $R = 0.3$ and frequency of 50 Hz [20]

Oriani and Josephic [13] presented a photo micrograph of the fracture surface of AISI 4340 steel cracking under hydrogen at ΔK of approximately $18.67 \text{ MPa}\sqrt{\text{m}}$, that is clearly a sharp inter-granular fracture as shown in Figure 36. No definitive conclusion can be made whether ΔK of $18.67 \text{ MPa}\sqrt{\text{m}}$ is within Region B for this steel from the information provided in the reference. ΔK of $18.67 \text{ MPa}\sqrt{\text{m}}$ is categorized as a low stress intensity factor while ΔK of $43.95 \text{ MPa}\sqrt{\text{m}}$ is considered high stress intensity factor.

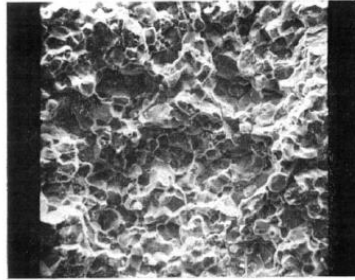


Figure 36 Fracture surface of AISI 4340 steel under hydrogen at ΔK of approximately $18.67 \text{ MPa}\sqrt{\text{m}}$ [13]

The photo micrograph of the fracture surface of AISI 4340 steel cracking under hydrogen at a high ΔK value of approximately $43.95 \text{ MPa}\sqrt{\text{m}}$, by Oriani and Josephic [13], indicates a contribution from a tearing mode that blurs the outlines of the grains while the fracture remains inter-granular, as shown in Figure 37.

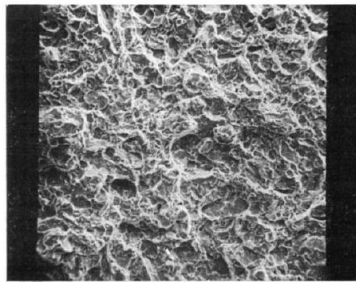


Figure 37 Fracture surface of AISI 4340 steel under hydrogen at ΔK of approximately $43.95 \text{ MPa}\sqrt{\text{m}}$ [13]

No HA-FCGR curve is provided in the referenced work by Oriani and Josephic [13]. Therefore, it cannot be determined which region above two values of ΔK fall under. Nonetheless, the observation demonstrates a transition from clear inter-granular fracture to inter-granular fracture with ductile tearing, while ΔK increases.

6.3 Region C

Regime C is defined as the steady state regime by Amaro et al. [7]. The effect of hydrogen embrittlement is saturated. The slope of the HA-FCGR curve closely resembles the slope of the FCGR curve of steel tested in air. The fracture surface of X100 steel tested in 20.7 MPa hydrogen by Amaro et al. [22] exhibits trans-granular quasi-cleavage marks in Region C, shown in below Figure 38. The red circle indicates the possible combination of ductile failure along the crack path.

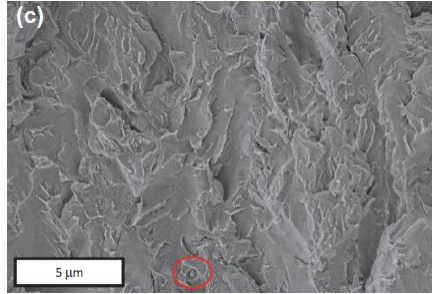


Figure 38 Fracture surface of X100 steel tested in 20.7 MPa hydrogen [22]

The fracture surface of X52 Alloy J steel tested in 6.9 MPa hydrogen by Amaro et al. [7] as well exhibits quasi-cleavage marks in Region C, shown in below Figure 39. An area of ductile failure is also circled in red.

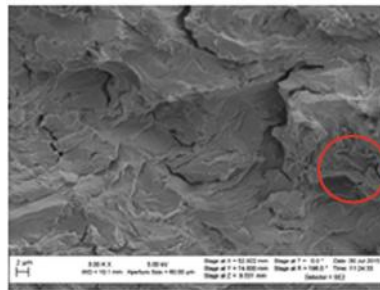


Figure 39 Fracture surface of X52 Alloy J steel tested in 6.9 MPa hydrogen [22]

Investigating the temperature effect on fatigue crack propagation of BS 4360 50EE low alloy steel in hydrogen gas and air, Marrow et al. [68] observed trans-granular cleavage facets on the fracture surfaces of specimens tested in hydrogen, and the area fraction of cleavage facets on the fracture surface increased with increasing ΔK and decreasing temperature. The corresponding FCGR curve and the fracture surface are shown in Figure 40. The value of ΔK for the shown fracture surface is not provided.

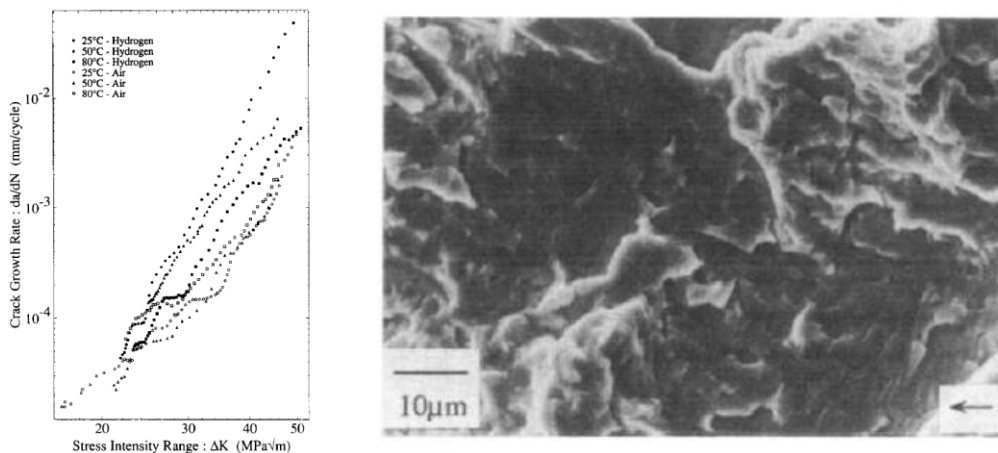


Figure 40 FCGR curve and fracture surface of BS 4360 50EE low alloy steel teste in hydrogen [68]

Quasi-cleavage fracture combined with ductile failure is observed for the fatigue crack surface in Region C by Amaro et al. [7] and Amaro et al. [22]. At a high ΔK , Oriani and Josephic [13] observed ductile tearing at the grain boundaries in an inter-granular dominant failure. Petti and Dodds [69] investigated the competition between trans-granular cleavage and ductile tearing mechanisms over the temperature driven ductile to brittle transition region. They suggested that ductile tearing pushes the crack front forward which increases the volume of material at high stress levels hereby increases the likelihood of failure by cleavage fracture. The ductile tearing occurs due to the coalescence of growing voids ahead of the crack front. The formation and growth of such voids potentially alter the local stress fields acting on the nearby inclusions, and eventually trigger cleavage fracture. It is therefore assumed in this study that failure begins to shift to an inter-granular fracture in Region B, and continues to transition to inter-granular fracture with ductile tearing at grain boundaries, to eventually trans-granular quasi-cleavage fracture while ΔK approaches Region C.

6.4 Summary

The HA-FCGR in Region A is nearly identical to FCGR of the material tested in air. Therefore, a trans-granular ductile failure mechanism is expected. In Region B, failure shifts to a brittle inter-granular fracture. Ductile tearing at grain boundaries then trans-granular quasi-cleavage marks begin to appear while ΔK approaches Region C. In Region C, quasi-cleavage facets are observed on the fatigue crack surface, along with a fraction of ductile cracking.

Based on the above observed fracture mechanisms of the three regions, it is reasonable to assume ΔK_1 represents the commencement of inter-granular fracture, and ΔK_2 and $(\frac{da}{dN})_2$ represent the stress intensity factor range and HA-FCGR where trans-granular quasi-cleavage fracture combined with ductile crack propagation appears on the fatigue failure surface. These assumptions are applied in the following chapters to quantify the key values of the Tri-Linear HA-FCGR curve.

7 Onset of hydrogen enhancement

The threshold ΔK_1 represents the minimum value of stress intensity factor range below which hydrogen does not affect the FCG response of steels [20]. ΔK_1 determines the shape of the predictive model of HA-FCGR. If the applied ΔK is below ΔK_1 , the hydrogen enhancement of the fatigue response is negligible. Therefore, the value of ΔK_1 is expected to be of great value to the energy industry in order to differentiate hydrogen affected and non-affected operating conditions. In this chapter, an effort is made to quantify ΔK_1 , using the known steel properties and fatigue test parameters provided in the experimental data. ΔK_1 is firstly related to the threshold stress intensity for hydrogen induced crack growth, K_{TH2} . The fatigue test results collected from literature are utilized to provide experimentally determined ΔK_1 .

7.1 The mechanism of fracture behind ΔK_1

Murakami and Matsuoka [70] presented peculiar void growth behaviour inside the hydrogen-charged pipeline steel specimen in a tensile test, compared to the uncharged specimen, as shown in Figure 41. Localized slip deformation attributed to the presence of hydrogen elongates the voids in the direction perpendicular to the tensile axis.

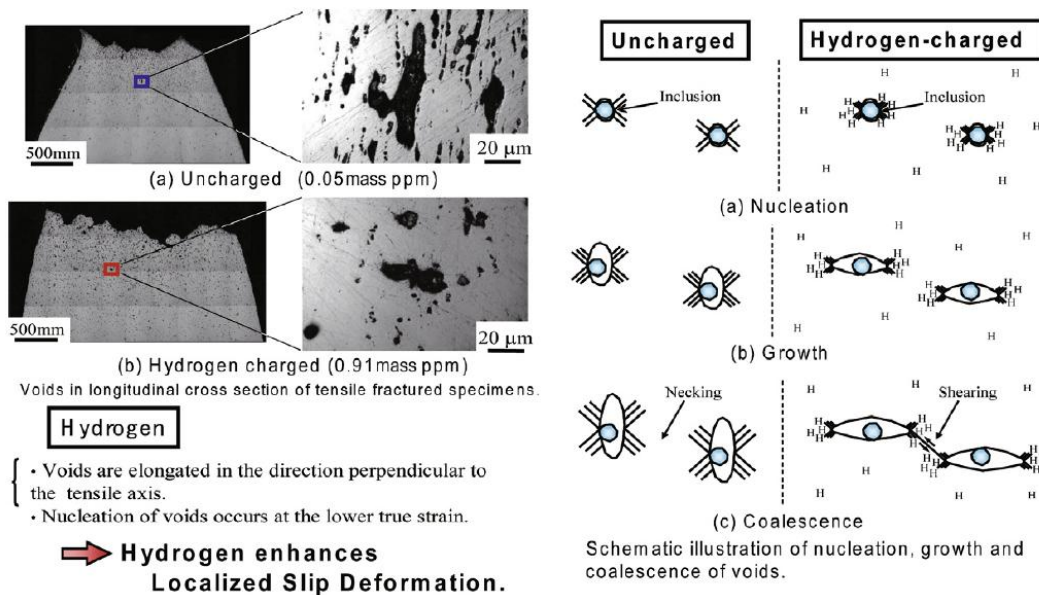


Figure 41 Development of voids in tensile test of a pipeline steel, JIS-SGP (0.078% carbon steel) [70]

Figure 42 shows the crack shapes and slip bands morphologies of uncharged and hydrogen-charged specimens of JIS SCM435 steel tested at ΔK of $20 \text{ MPa}\sqrt{\text{m}}$ under a frequency of 20 Hz. Many slip bands spread widely along the crack line in the uncharged specimen. The slip bands of the hydrogen-charged specimen are localized in a very narrow area immediately next to the crack line. The slip localization

induced by hydrogen at the crack tip elongates the voids under loading. As a result, the diameter that represents the size of the void decreases in the presence of hydrogen introducing higher stress concentration. This observation bears a resemblance to the HELP mechanism introduced in Chapter 2. Owing to HELP, decreased elastic interaction between adjacent slip bands can potentially lead to more closely spaced slip bands and smaller slip steps [3]. This agrees with the observation of slip bands located in a narrow area next to the crack line. Moreover, HELP argues that subcritical crack growth occurs by a more localized micro-void coalescence process assisted by hydrogen. Consequently, the void size is reduced due to localized coalescence. To summarize, hydrogen induces localized narrow slip bands, which subsequently lowers the size of the voids, introducing higher stress concentration.[3]

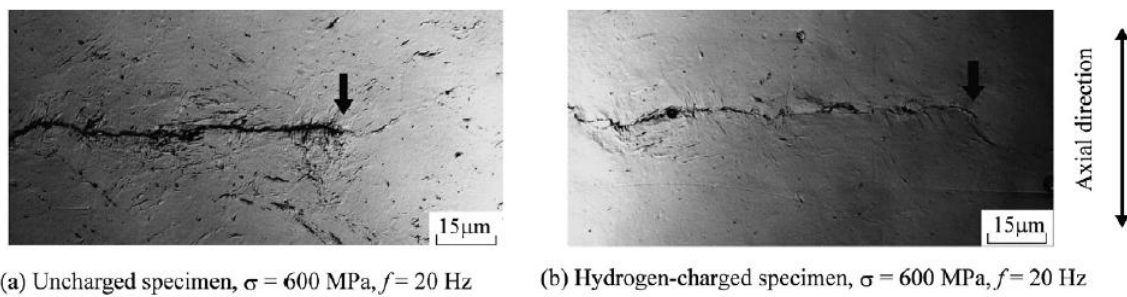


Figure 42 Slip bands and fatigue cracks at ΔK of $20 \text{ MPa}\sqrt{\text{m}}$ [70]

It cannot be determined if ΔK of $20 \text{ MPa}\sqrt{\text{m}}$ falls under Region B of the HA-FCGR curve from the information provided in the referenced literature. ΔK_1 in this work represents the onset of hydrogen enhanced FCGR, where the fatigue cracking shifts from ductile to brittle behaviour. Chapter 6.2 provides support that in Region B failure shifts to brittle inter-granular fracture. Therefore, an assumption is made in this study that ΔK_1 corresponds to the commencing of inter-granular fracture induced by micro-void coalescence along the grain boundaries, adopting the HELP mechanism.

7.2 ΔK_1 and K_{TH2}

The K_{max} corresponding to ΔK_1 can be written as $\Delta K_1 / (1 - R)$. Anderson [9] proposed a model where K_{max} equal to K_{IEAC} illustrated in Figure 3, which is the static loading threshold stress intensity for environmental cracking. Suresh and Ritchie [20] relate the stress intensity range at which abrupt hydrogen enhancement of the FCGR occurs to K_{max}^T , shown in Figure 9. Suresh and Ritchie however state K_{max}^T often coincides with the threshold stress intensity K_{IEAC} in high strength steels and is considerably less in lower strength steels.

McEvily and Wei [38] characterize environment-enhanced FCG response of high strength metals into Type A, B and C. Type A represents a synergistic action of fatigue and corrosion in the material-environment system. In the system of Type B, substantial environment-enhanced sustained load crack growth appears

above the apparent threshold for stress corrosion cracking, K_{ISCC} , and the environmental effects are negligible below K_{ISCC} . Generally, material-environment systems fall between the two extremes Type A and B, that is Type C, shown in Figure 43. The predictive model proposed by McEvily and Wei is introduced in Chapter 3.4.

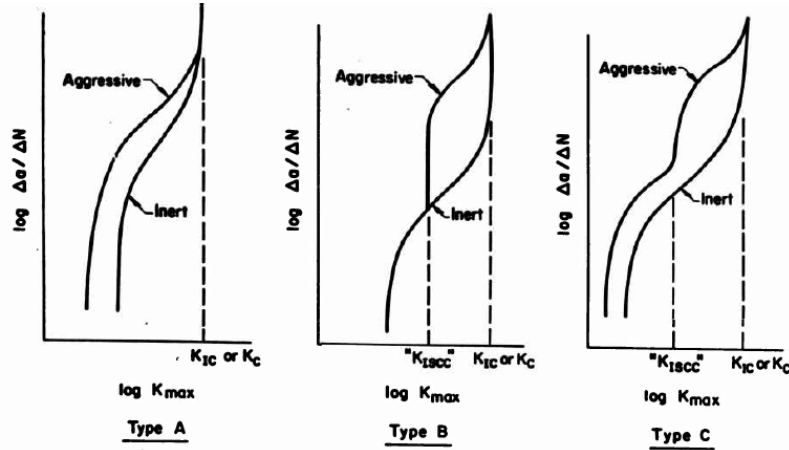


Figure 43 Types of FCG behaviour [38]

Suresh and Ritchie [20] suggest that the K_{max} corresponding to ΔK_1 is considerably less than K_{ISCC} in lower strength steels. However, according to the predicted desirable operating conditions for the hydrogen transmission pipelines in Chapter 1.2, it is expected for the energy sector to favour medium to high strength steels. For the purposes of this study, it is reasonable to correlate the static loading threshold stress intensity for hydrogen assisted cracking, denoted as K_{TH2} hereafter, with ΔK_1 on the HA-FCGR curves.

7.3 Verification of EAC model

7.3.1 Complete EAC model

The theoretical EAC model by Anderson [9] is presented in complete form first, as follows:

$$\left(\frac{da}{dN}\right)_{total} = \left(\frac{da}{dN}\right)_{inert} + \left(\frac{da}{dN}\right)_{EAC}, \quad (63)$$

where $\left(\frac{da}{dN}\right)_{inert}$ is the crack growth per cycle due to fatigue of the material in an inert environment, and

$\left(\frac{da}{dN}\right)_{EAC}$ is the environmental crack growth rate. $\left(\frac{da}{dN}\right)_{EAC}$ can be expressed by the crack growth per unit time as:

$$\left(\frac{da}{dN}\right)_{EAC} = \int_0^{T_{period}} \frac{da}{dt} dt, \quad (64)$$

where t is time and T_{period} is the period of one cycle. It is expected that $\frac{da}{dt}$ is a function of the test parameters and the stress intensity K . Anderson [9] references $\frac{da}{dt}$ curves of 4130 steel exposed to gaseous hydrogen under different pressure, shown in below Figure 44.

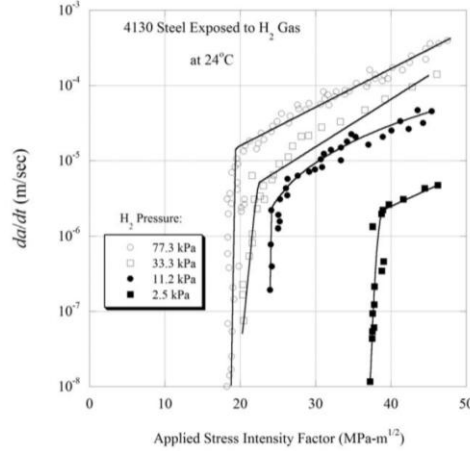


Figure 44 Cracking of 4130 steel exposed to gaseous hydrogen [9]

For the purpose of verification of this EAC model, $\frac{da}{dt}$ is approximated to be a function of the hydrogen pressure and K , as follows:

$$\frac{da}{dt} = \begin{cases} 0 & K < K_{IEAC} \\ \exp(A_{EAC} + B_{EAC} \cdot P_H^{C_{EAC}} \cdot K) & K_{IEAC} < K \end{cases} \quad (65)$$

where A_{EAC} , B_{EAC} and C_{EAC} are fitted constants, and the static loading threshold stress intensity for environmental cracking, K_{IEAC} , below which no environmentally assisted cracking occurs, is given by:

$$K_{IEAC} = a_{EAC} P_H^{b_{EAC}}, \quad (66)$$

where a_{EAC} and b_{EAC} are fitted constants.

The cyclic loading is assumed to be a sine wave, given by:

$$K = \frac{\Delta K}{1-R} - \frac{\Delta K}{2} + \frac{\Delta K}{2} \sin(2\pi ft), \quad (67)$$

7.3.2 Curve fitting and verification of the EAC model

Results of three fatigue tests from literature are selected to fit to the EAC model presented above. The Least Square Method is implemented in MATLAB to obtain the optimized fitted parameters included in the EAC model, namely A_{EAC} , B_{EAC} , C_{EAC} , a_{EAC} and b_{EAC} . Since K_{IEAC} and $\frac{da}{dt}$ are both dependent on only the test parameter P_H , it is assumed that one set of optimized fitted parameters of the EAC model is applicable to fatigue tests of the same material with the same test conditions except for the hydrogen

pressure P_H . Therefore, results of three fatigue tests from literature of the same test material under the same test conditions, except for different hydrogen pressure, as the three fatigue tests of which the results are fitted to the EAC model respectively, are selected to verify the EAC model.

The test parameters of the fatigue tests, the fitted parameters, ΔK_1 derived from the fitted parameters, and the associated environmentally assisted FCGR curves are presented in Table 10.

Table 10 Curve fitting and verification of the EAC model

Reference	Test parameters	EAC model - fitted parameters	Curve
Amaro et al. [22]	Detailed source: Fig. 8 Material: API-5L X100 P_H (MPa): 6.89 R : 0.5 f (Hz): 1.00 T (K): 293 σ_y (MPa): 689 a_{air} : 9.90E-9 B_{air} : 2.8300 ΔK_1 (MPa \sqrt{m}): 6.59	A_{EAC} : -9.704874 B_{EAC} : 0.084966 C_{EAC} : 0.010405 a_{EAC} : 19.787460 b_{EAC} : -0.009955 K_{IEAC} (MPa \sqrt{m}): 18.1209 $K_{IEAC}(1-R)$ (MPa \sqrt{m}): 9.0604	
Amaro et al. [22]	Detailed source: Fig. 8 Material: API-5L X100 P_H (MPa): 1.72 R : 0.5 f (Hz): 1.00 T (K): 293 σ_y (MPa): 689 a_{air} : 9.90E-9 B_{air} : 2.8300 ΔK_1 (MPa \sqrt{m}): 7.50	Applying the same fitted parameters as above K_{IEAC} (MPa \sqrt{m}): 18.3730 $K_{IEAC}(1-R)$ (MPa \sqrt{m}): 9.1865	
Slifka et al. [54]	Detailed source: Fig. 6 Material: X100 P_H (MPa): 7 R : 0.5 f (Hz): 1.00 T (K): 293 σ_y (MPa): 705 a_{air} : 9.84E-9 B_{air} : 2.8290 ΔK_1 (MPa \sqrt{m}): 6.01	A_{EAC} : -8.541096 B_{EAC} : 0.069633 C_{EAC} : 0.012151 a_{EAC} : 19.208253 b_{EAC} : -0.000108 K_{IEAC} (MPa \sqrt{m}): 19.1899 $K_{IEAC}(1-R)$ (MPa \sqrt{m}): 9.5950	
Slifka et al. [54]	Detailed source: Fig. 6 Material: X100 P_H (MPa): 1.7 R : 0.5 f (Hz): 1.00 T (K): 293 σ_y (MPa): 705 a_{air} : 9.84E-9 B_{air} : 2.8290 ΔK_1 (MPa \sqrt{m}): 7.15	Applying the same fitted parameters as above K_{IEAC} (MPa \sqrt{m}): 19.1928 $K_{IEAC}(1-R)$ (MPa \sqrt{m}): 9.5964	

Slifka et al. [15]	Detailed source: Fig. 12 Material: X52 vintage P_H (MPa): 34.5 R : 0.5 f (Hz): 1.00 T (K): 293 σ_y (MPa): 325 a_{air} : 3.00E-9 B_{air} : 3.1563 ΔK_1 (MPa \sqrt{m}): 7.59	A_{EAC} : -7.335031 B_{EAC} : 0.030944 C_{EAC} : 0.012720 a_{EAC} : 69.247145 b_{EAC} : -0.113687 K_{IEAC} (MPa \sqrt{m}): 21.1111 $K_{IEAC}(1 - R)$ (MPa \sqrt{m}): 10.5556	
Slifka et al. [15]	Detailed source: Fig. 12 Material: X52 vintage P_H (MPa): 5.5 R : 0.5 f (Hz): 1.00 T (K): 293 σ_y (MPa): 325 a_{air} : 3.00E-9 B_{air} : 3.1563 ΔK_1 (MPa \sqrt{m}): 8.43	Applying the same fitted parameters as above K_{IEAC} (MPa \sqrt{m}): 26.0119 $K_{IEAC}(1 - R)$ (MPa \sqrt{m}): 13.0059	

7.3.3 Summary

Table 10. demonstrates that even though the EAC model does not precisely reflect Region B defined by Amaro et al. [7], $K_{IEAC}(1 - R)$ is consistently 1.2 to 1.6 times the value of ΔK_1 obtained from curve fitting the fatigue test results detailed in Chapter 5.3. K_{IEAC} is assumed to be a function of P_H , and is approximated by the Least Square Optimization of the assumed EAC model. ΔK_1 is as well approximated by the Least Square Optimization applying the updated HA-FCGR model to the fatigue test data. With the approximation of the models and the uncertainty of the data associated with this procedure of verification, it is not expected that $K_{IEAC}(1 - R)$ equals ΔK_1 exactly. Nevertheless, the initial approach to predict ΔK_1 by quantifying the static loading threshold stress intensity for hydrogen assisted cracking, denoted as K_{TH2} , is deemed viable.

7.4 Quantification of K_{TH2}

The HELP mechanism is introduced in Chapter 2, which proposes that a more localized micro-void coalescence process induced by hydrogen produces subcritical crack growth. For the HELP mechanism, Gerberich [71] provided a mechanism linked to the work of separation in shear of the ligaments as follows:

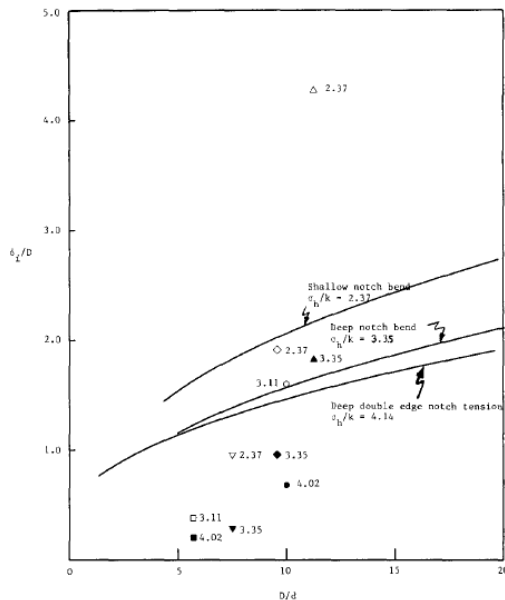
$$G_{IC} \approx \frac{\sigma_y l_0^2}{\sqrt{3} 2d_0}, \quad (68)$$

where G_{IC} is the critical strain energy release rate, l_0 is the ligament height, and d_0 is the hole size. G_{IC} represents the energy required to propagate a crack per unit area. l_0 is the distance between two voids, which represents how much material is available to deform before failure. The term $\sigma_y l_0^2$ thus provides an

estimate of the plastic work done per unit thickness ($\frac{N \cdot m}{m}$) of the material. The diameter of the void, d_0 , controls the stress concentration level and influences the initiation of fracture. The energy per unit thickness stored in the material between two voids normalized by the hole size gives the energy per area ($\frac{N \cdot m}{m^2}$), matching the definition of G_{IC} .

The plastic zone grows with l_0^2 . A larger void spacing l_0 indicates more bulk material between voids, allowing for greater plastic deformation and energy absorption prior to void coalescence. This leads to an enlarged plastic zone, resulting in increased crack tip blunting, which corresponds to a greater crack tip opening displacement at the onset of crack propagation, denoted as δ_{IC} .

Wu et al. [72] analyzed the effect of hydrostatic stress on the growth of voids from inclusions located near the tip of the notch. A slip line theory by Rice and Johnson estimates the crack tip opening displacement at initiation, δ_i , is approximately 1 to 2.7 times the inclusion spacing denoted as D . Figure 45 is provided to present δ_i/D as a function of D/d_i with d_i being the inclusion diameter, using the Rice-Tracey model for void growth ahead of the crack tip. δ_i hence is positively correlated to the square of the inclusion spacing.



Condition	0.2% Proof stress (MPa)	Ultimate tensile strength (MPa)	Elongation (%)	Reduction in area (%)	Inclusion spacing (μm)	Inclusion/void size (μm)	a/W	δ_i (mm)	Symbol in Figure 3
Normalized ¹	202	338	29	35	45	4	0.1	0.192	△
							0.5	0.082	▲
5% Prestrained ¹	325	385	19	27	45	4.7	0.1	0.086	◇
							0.5	0.043	◆
15% Prestrained ¹	421	424	6.7	22	45	6.0	0.1	0.043	▽
							0.5	0.013	▼
Normalized ²	240	400	-	-	100	10	0.2	0.160	○
							0.5	0.068	●
20% Prestrain ²	630	660	-	-	100	~17.5	0.2	~0.038	□
							0.5	0.02	■

¹Steel studied in present work.

²Steel studied by Thompson and Knott [19].

Figure 45 δ at void coalescence curves based on slip-line theory of experimental data [72]

Li et al. [73] calculated the relationship between the critical crack tip opening displacement, δ_{IC} , and $X_0(R_V/R_I)|_{R_{av}}$ for ultra-high strength steel AerMet100, where X_0 is the average inclusion size spacing, R_V/R_I is the void radius divided by the inclusion radius, nucleating the void evaluated at the average inclusion size R_0 . δ_{IC} is in linear relationship with $X_0(R_V/R_I)|_{R_{av}}$ shown in Figure 46. This again indirectly indicates δ_{IC} is positively correlated to the inclusion spacing.

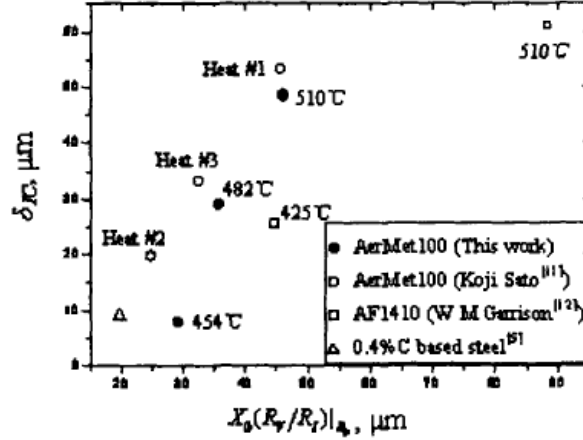


Figure 46 Relationship between calculated δ_{IC} and $X_0(R_V/R_I)|_{R_{av}}$ [73]

For the purpose of predicting K_{TH2} based upon voids coalescence along the grain boundaries, voids and inclusions are not explicitly differentiated. Void spacing l_0 can be considered equivalent to the inclusion spacing representing the material available to deform plastically before failure. Therefore, l_0 is approximated as being proportional to δ_{IC} at K_{TH2} , that is $\frac{K_{TH2}^2}{\sigma_y E}$ employing the standard relationship of crack tip opening displacement, δ . The applied stress intensity becomes K_{TH2} when $G_{IC} = \frac{K_{TH2}^2}{E}$ is reached. Combining Equation (68), $l_0 \approx \frac{K_{TH2}^2}{\sigma_y E}$ and $G_{IC} = \frac{K_{TH2}^2}{E}$, K_{TH2} can be expressed as follows:

$$K_{TH2} = (2\sqrt{3}\sigma_y E d_0)^{0.5}, \quad (69)$$

Rice and Tracy [74] applied an approximate Rayleigh-Ritz procedure to the enlargement of an isolated spherical void in a non-hardening material, shown in Figure 47. Void growth is investigated under a remote tensile extension field with superposed hydrostatic stresses and is concluded to be essentially spherical. A dilatation amplification factor D_a is introduced as:

$$D_a = \dot{R}_0 / \dot{\epsilon} R_0, \quad (70)$$

where $\dot{\epsilon}$ is the strain rate, R_0 is the original void size, and \dot{R}_0 is the average radial velocity on the void boundary.

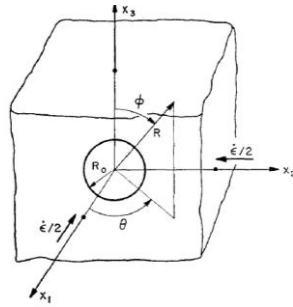


Figure 47 Spherical void in a remote simple tension strain field [74]

Figure 48 displays the proposed approximation of D_a as a function of mean normal stress over yield stress as follows:

$$D_a = 0.283 \exp(\sqrt{3} \sigma_\infty / 2 \sigma_0), \quad (71)$$

where σ_∞ is the mean normal stress, and σ_0 is yield stress. Given the same mean normal stress, D_a is positively correlated to $1/\sigma_0$.

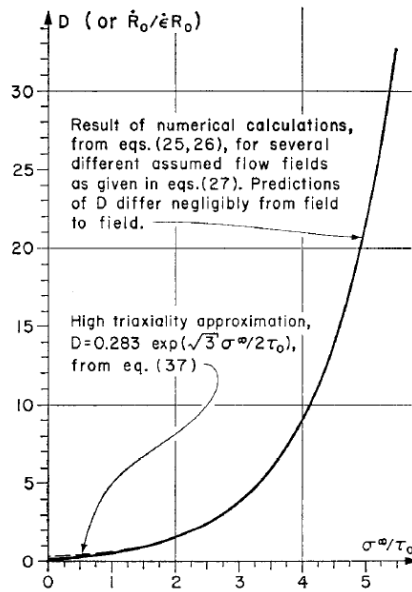


Figure 48 Dilatation amplification factor D_a [74]

The parameter d_0 in Equation (69) represents the critical size of the void at failure. It is relevant to the void nucleation and growth. However, it is not feasible to quantify the void nucleation under fatigue loading. From above research study by Rice and Tracy [74], the dilatation amplification factor D_a representing void growth is positively correlated to $1/\sigma_0$. Therefore, d_0 is assumed to be positively correlated to $1/\sigma_0$ to begin with. Inevitably, d_0 is also affected by the presence of hydrogen. As illustrated in Chapter 7.1, the hydrogen induced localized slip deformation elongates the voids resulting a reduced d_0 associated with

higher stress concentration. To incorporate the hydrogen effect and the strain rate $\dot{\epsilon}$ included in Equation (71) expressing D_a , the novel parameter $\sqrt{P_H f}$ introduced by Yoshikawa et al. [34] is utilized.

The strain rate $\dot{\epsilon}$ is represented by the cyclic load frequency f in this study. Although $\dot{\epsilon}$ is related to both the frequency and the amplitude of the applied strain, the strain amplitude is effectively captured by the stress intensity factor range in the context of this study. As such, f alone is used as a proxy for $\dot{\epsilon}$. With more time available for the micro-voids to coalesce, a larger void equivalent to a greater d_0 is expected to appear with a decreasing f , leading to a greater value of K_{TH2} . Given the same load ratio R , a greater threshold K_{TH2} results in a higher ΔK_1 , which aligns with the test results from Matsuo et al. [59] as reviewed in Chapter 4.2.3. Yoshikawa et al. [34] examined the joint effect of hydrogen pressure and load frequency, and proposed a novel parameter $\sqrt{P_H f}$ to represent the gradient of hydrogen concentration in front of a crack tip. A hydrogen penetration depth is introduced as $\sqrt{D_H t_H}$, where D_H is the hydrogen diffusivity coefficient, and $t_H = 1/(2f)$. The gradient of hydrogen concentration is initially expressed as $\frac{C_s}{\sqrt{D_H t_H}}$, where C_s is the concentration of hydrogen at the crack surface. With C_s positively increasing with $\sqrt{P_H}$, the gradient of hydrogen concentration is simplified to $\sqrt{P_H f}$. Figure 49 shows the hydrogen concentration distribution ahead of the crack tip as proposed.

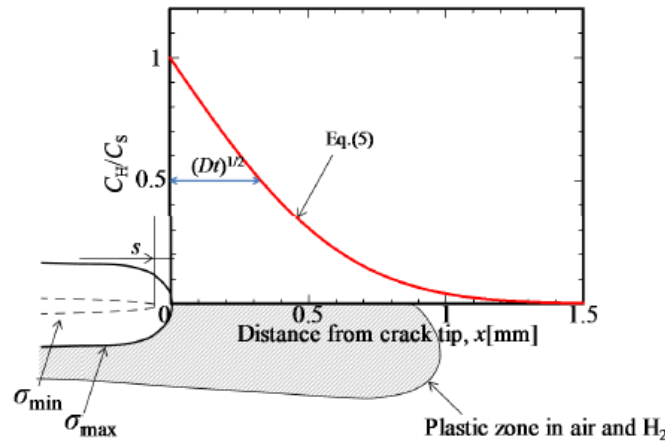


Figure 49 Hydrogen concentration distribution ahead of the crack tip [34]

Under a fixed value of ΔK , the hydrogen enhancement of FCGR is negligible when $\sqrt{P_H f}$ is below a critical value, and abruptly increases when $\sqrt{P_H f}$ is above this critical value, as illustrated in Figure 50. It's worth noting that the critical value of $\sqrt{P_H f}$ could vary for different steels at different test conditions.

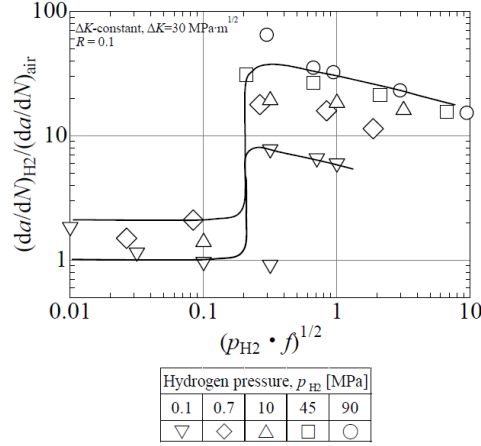


Figure 50 Relationship between hydrogen enhancement of FCGR and $\sqrt{P_H f}$ [34]

The photos and illustrations of the voids in hydrogen charged and uncharged materials shown in Figure 41 demonstrate that d_0 decreases in the presence of hydrogen due to the elongation of the voids prompted by hydrogen. Equation (69) yields a lower K_{TH2} with a reduced d_0 in the presence of hydrogen. This aligns with the observation that steels behave in a more brittle manner under the influence of hydrogen. Therefore, it is assumed that with a lower hydrogen concentration gradient $\sqrt{P_H f}$, the hydrogen effect is less significant indicating that d_0 decreases only slightly. The stress intensity introduced by the voids is thus weakened leading to a higher K_{TH2} in return.

In this study, the critical value of $\sqrt{P_H f}$ is determined to be $1\sqrt{MPa/s}$, based on the experimental data. When $\sqrt{P_H f}$ is below $1\sqrt{MPa/s}$, $\sqrt{P_H f}$ is incorporated into d_0 to account for the increase of d_0 under a lower gradient of hydrogen concentration.

The parameter d_0 in Equation (69) is therefore expressed as a function of $1/\sigma_y$ and $\sqrt{P_H f}$ as follows:

$$d_0 \begin{cases} = \frac{C_{11} \exp\left(\frac{C_{12}}{\sigma_y}\right)}{\sqrt{P_H f}}, & \text{if } \sqrt{P_H f} < 1\sqrt{MPa/s} \\ = C_{11} \exp\left(\frac{C_{12}}{\sigma_y}\right), & \text{if } \sqrt{P_H f} \geq 1\sqrt{MPa/s} \end{cases} \quad (72)$$

where fitted constants $C_{11} = 9.4235199 \times 10^{-8} m$ and $C_{12} = 776.99309 MPa$, and the unit of d_0 is m .

7.5 Predicted ΔK_1

ΔK_1 is calculated as the predicted K_{TH2} multiplied by $(1 - R)$ as follows:

$$\Delta K_1 = (2\sqrt{3}\sigma_y E d_0)^{0.5} (1 - R), \quad (73)$$

where d_0 is expressed by Equation (72).

The test parameters, material properties, ΔK_1 obtained from curve fitting of the fatigue test results, ΔK_1 predicted by the model described in the previous chapters, along with the referenced literature are summarized in Table 11.

Table 11 ΔK_1 Prediction

Reference	Figure	Material	P_H (MPa)	R	f (Hz)	T (K)	σ_y (Mpa)	ΔK_1 Data ($MPa\sqrt{m}$)	$\sqrt{P_H f}$ ($\sqrt{MPa/s}$)	d_0 (m)	ΔK_1 Prediction ($MPa\sqrt{m}$)
Amaro et al. [22]	Fig. 8	API-5L X100	1.7	0.5	1.00	293	689	7.50	1.31	2.91E-07	6.04
Amaro et al. [22]	Fig. 8	API-5L X100	6.9	0.5	1.00	293	689	6.59	2.62	2.91E-07	6.04
Drexler et al. [65]	Fig. 7	X70A	34.0	0.5	1.00	293	509	6.14	5.83	4.34E-07	6.34
Drexler et al. [65]	Fig. 7	X70B	34.0	0.5	1.00	293	553	6.37	5.83	3.84E-07	6.22
Matsuoka et al. [58]	Fig. 1	JIS-SM490B	0.7	0.1	1.00	298	360	12.52	0.84	9.75E-07	14.38
Matsuoka et al. [58]	Fig. 1	JIS-SM490B	0.7	0.1	1.00	363	360	15.40	0.84	9.75E-07	14.38
Matsuoka et al. [58]	Fig. 1	JIS-SM490B	10.0	0.1	1.00	423	360	16.16	3.16	8.16E-07	13.15
Ronevich et al. [55]	Fig. 4	X52	21.0	0.5	1.00	295	360	5.84	4.58	8.16E-07	7.31
Ronevich et al. [66]	Fig. 5	X100	21.0	0.5	1.00	295	690	5.18	4.58	2.91E-07	6.04
Ronevich et al. [49]	Fig. 4	J00	21.0	0.1	1.00	293	429	8.81	4.58	5.76E-07	12.07
Slifka et al. [54]	Fig. 6	X100	1.7	0.5	1.00	293	705	7.15	1.30	2.84E-07	6.03
Slifka et al. [54]	Fig. 6	X100	7.0	0.5	1.00	293	705	6.01	2.65	2.84E-07	6.03
Slifka et al. [54]	Fig. 8	X100	7.0	0.5	0.10	293	705	5.94	0.84	3.39E-07	6.59
Slifka et al. [54]	Fig. 7	X52	7.0	0.5	1.00	293	426	6.09	2.65	5.84E-07	6.73
Slifka et al. [15]	Fig. 12	X52 vintage	5.5	0.5	1.00	293	325	8.43	2.35	1.03E-06	7.80
Slifka et al. [15]	Fig. 12	X52 vintage	34.5	0.5	1.00	293	325	7.59	5.87	1.03E-06	7.80
Slifka et al. [15]	Fig. 12	X52 modified	5.5	0.5	1.00	293	487	5.80	2.35	4.65E-07	6.42
Slifka et al. [15]	Fig. 16	X52 vintage	5.5	0.5	0.10	293	325	8.99	0.74	1.39E-06	9.06
Slifka et al. [15]	Fig. 13	X70B	5.5	0.5	1.00	293	553	9.51	2.35	3.84E-07	6.22
Slifka et al. [15]	Fig. 17	X70A	34.5	0.5	0.10	293	509	6.02	1.86	4.34E-07	6.34
Yamabe et al. [33]	Fig. 5	JIS-SM490B	0.7	0.1	1.00	293	360	12.60	0.84	9.75E-07	14.38
Yamabe et al. [33]	Fig. 5	JIS-SM490B	0.7	0.1	1.00	363	360	15.49	0.84	9.75E-07	14.38
Yamabe et al. [33]	Fig. 5	JIS-SM490B	0.7	0.1	1.00	423	360	19.13	0.84	9.75E-07	14.38
Yoshikawa et al. [34]	Fig. 5	JIS-SM490B	0.7	0.1	1.00	293	360	12.53	0.84	9.75E-07	14.38
Zafra et al. [57]	Fig. 11 (Ronevich 2016)	X65	21.0	0.5	1.00	293	450	5.50	4.58	5.30E-07	6.58

The predicted ΔK_1 is plotted against the experimental ΔK_1 collected from literature in Figure 51.

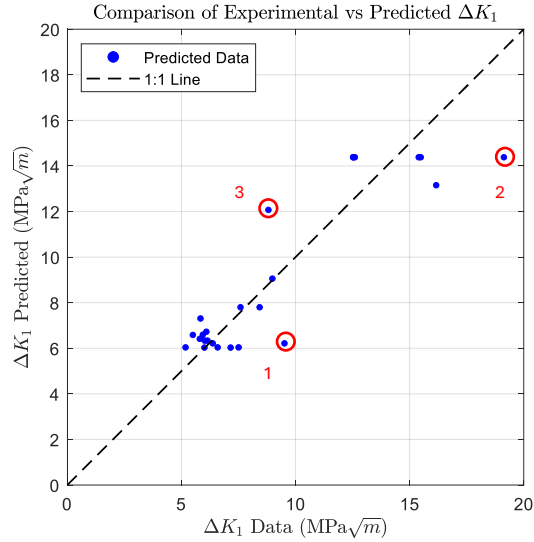


Figure 51 Comparison of predicted ΔK_1 and experimental ΔK_1

7.6 Discussion

Data sets 1, 2 and 3 circled in Figure 51 show a relatively higher level of deviation between the measured and estimated ΔK_1 values; therefore, these three pairs of predicted and experimental ΔK_1 are further reviewed. The information correlated to these three data sets is summarized in Table 12.

Table 12 Predicted ΔK_1 for further review

Data sets	Reference	Figure	Material	P_H (MPa)	R	f (Hz)	T (K)	σ_y (MPa)	ΔK_1 Data (MPa \sqrt{m})	ΔK_1 Predicted (MPa \sqrt{m})
1	Slifka et al. [15]	Fig. 13	X70B	5.5	0.5	1.00	293	553	9.51	6.22
2	Yamabe et al. [33]	Fig. 5	JIS-SM490B	0.7	0.1	1.00	423	360	19.13	14.38
3	Ronevich et al. [49]	Fig. 4	J00	21.0	0.1	1.00	293	429	8.81	12.07

The predicted ΔK_1 is 65% and 75% of the experimental ΔK_1 at data sets 1 and 2, respectively. Figure 52 is the fitted HA-FCGR curve based on the experimental data corresponding to data set 1. Fitted ΔK_1 is determined to be 9.51 MPa \sqrt{m} . However, the test data does not offer a clear knee point ΔK_1 . It is possible that the value of ΔK_1 is below 8 MPa \sqrt{m} that is not contained in the fatigue test. This is potentially the reason why the predicted ΔK_1 is well below the 1:1 line in Figure 51. The temperature for the fatigue test associated with data set 2 is 423 K that is significantly higher than room temperature. It is reviewed in Chapter 4.2.5 that an elevated temperature mitigates the hydrogen enhancement of the fatigue response. Experimental results show that the threshold stress intensity factor for hydrogen fracture increases with an increasing temperature. The predictive model for ΔK_1 proposed in Chapters 7.4 and 7.5 does not take temperature into account. The predicted ΔK_1 for data set 2 is relatively low compared to the experimental ΔK_1 that is increased due to the elevated temperature.

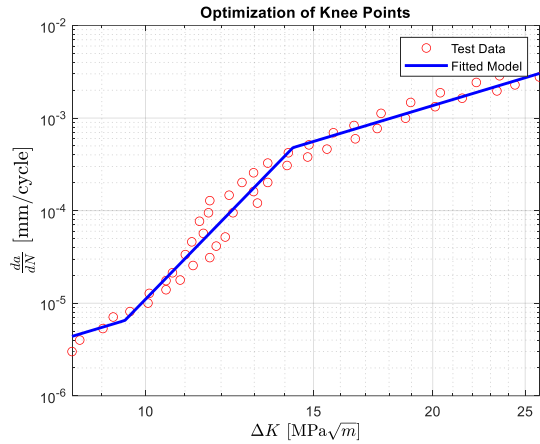


Figure 52 Fitted curve corresponding to data set 1

The predicted ΔK_1 of data set 3 is 137% of the experimental ΔK_1 . The load ratio of the fatigue test corresponding to data set 3 is 0.1. A higher ΔK_1 is expected with a lower R , as reviewed in Chapter 4.2.8. Figure 53 shows the fitted HA-FCGR curve based on the experimental data corresponding to data set 3, and the original figure from the reference. The knee point ΔK_1 is ambiguous. Another potential value for ΔK_1 can be above $10 \text{ MPa}\sqrt{\text{m}}$. The overestimate of ΔK_1 at data set 3 can be limited to 20% accordingly.

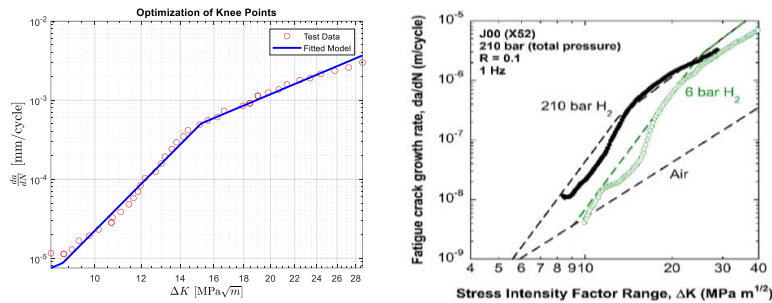


Figure 53 Fitted curve and original figure [49] corresponding to data set 2

It is apparent that the fitted ΔK_1 values from the fatigue test results affect the level of calculated accuracy of the predictive model. However, there exists inevitable optimization error in the fitted ΔK_1 applying Least Square Method in MATLAB. The fitted curves are results of optimized local minimum. The column “Error” in Table 9 presents the residual error of the optimization. This error should be considered when evaluating the reliability of the predictive model

There also lies the opportunity to further improve the predictive model for ΔK_1 including the temperature effect. If the test temperature is above room temperature, the predictive model remains conservative, offering a lower onset of hydrogen enhancement of the HA-FCGR, ΔK_1 .

8 ΔK_2 at hydrogen enhancement saturation

ΔK_2 represents the stress intensity factor range at which the effect of hydrogen on the FCGR saturates. The slope of the HA-FCGR curve returns to approximately that of fatigue response of steel in air. In this chapter, an effort is made to quantify ΔK_2 , using the known steel properties and fatigue test parameters provided in the fatigue test data. The previous experimental results collected from literature is utilized to provide experimentally determined ΔK_2 .

8.1 Fracture mechanisms

Based on the fracture mechanisms reviewed and proposed in Chapter 6.2 and Chapter 6.3, it is assumed in this study that from ΔK_1 to ΔK_2 , the failure transitions from inter-granular fracture to inter-granular fracture with ductile tearing at the grain boundaries, to eventually trans-granular quasi-cleavage fracture mixed with ductile crack propagation. ΔK_2 represents the stress intensity factor range at which quasi-cleavage fracture is dominant while ductile crack propagation begins to appear. The predictive model to quantify ΔK_2 is based on predicting cleavage fracture toughness.

8.2 Dislocation velocity affected by hydrogen

Courtney [75] presented an empirical equation representing the relation between dislocation velocity v_D and applied shear stress τ by:

$$\frac{v_D}{v_0} = \left(\frac{\tau}{\tau_0}\right)^{e_D}, \quad (74)$$

where τ_0 and e_D are experimentally determined material constants, and v_0 is the dislocation velocity at stress τ_0 . The dislocation velocity is therefore strongly dependent on the applied shear stress.

Taketomi et al. [76] as well correlated the dislocation velocity and shear stress in the absence of hydrogen, as shown in below Figure 54.

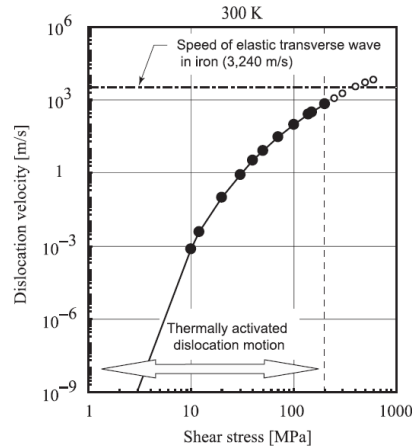


Figure 54 Correlation between dislocation velocity and shear stress without hydrogen [76]

Taketomi et al. [76] further investigated the occurrence of interactions between an edge dislocation and a hydrogen atom by estimating the stress dependent energy barriers for the dislocation motion and hydrogen diffusion in alpha iron using atomistic calculations. The results show that dislocation mobility is increased (softening) at a lower applied stress, and dislocation mobility is decreased (hardening) at an intermediate stress. There is no effect on the steady motion of a dislocation at a higher stress. The analysis of the energy barrier for the dislocation motion in the presence of a hydrogen atom was carried out using the Nudged Elastic Band method. Figure 55 offers an illustration of the analysis.

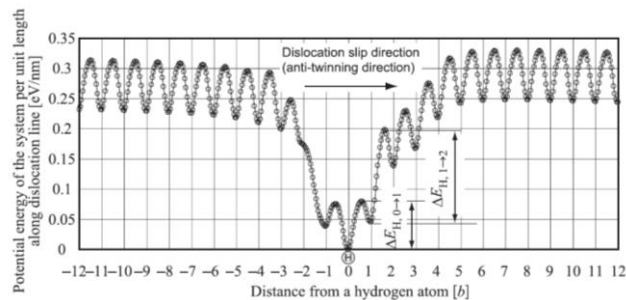


Figure 55 Potential energy barrier of edge dislocation motion around a hydrogen atom [76]

It is considered by Taketomi et al. [76] that the dislocation moves first, and the hydrogen atom diffuses to the dislocation subsequently. Because the hydrogen atom increases the energy barrier for the movement of the dislocation, the dislocation velocity is reduced due to the higher energy barrier, compared to the dislocation velocity without the presence of hydrogen. The dislocation can potentially escape from hydrogen when the applied shear stress is substantial.

The above referenced study is centered on one dislocation core, as one representation of the complex dislocation structure and movement in the plastic zone.

Firstly, this hypothesis of hydrogen reducing dislocation mobility at high stress, which in turn strengthens the material locally, is supported by the observation of trans-granular quasi-cleavage fracture surface at ΔK_2 .

Secondly, it is established that at ΔK_2 , the hydrogen enhancement of the FCGR saturates as the slope of the HA-FCGR curve returns to that of the FCGR curve for the same material tested in air. It is observed that the fracture surfaces of steels tested at a ΔK value that is above ΔK_2 exhibit quasi-cleavage fracture combined with ductile crack propagation. It is therefore assumed in this study that when the applied stress intensity is sufficiently high for the dislocations to escape the diffusing hydrogen, ΔK_2 is reached. Consequently, ductile crack propagation appears on the fracture surface, and the slope of the HA-FCGR restores to that of the FCGR curve of the same material tested in air. Amsterdam et al. [64] offered a physical explanation of the change in the FCGR slope. They concluded that the change in the FCGR slope is most likely due to a change in plasticity or plastic dissipation at the crack tip. It is hypothesized in this study if the velocity of some dislocations promoted by stress intensity is sufficiently high to escape hydrogen, the escaped dislocations produce a considerably similar plastic dissipation to that of fatigue in air. As a result, the slope of the HA-FCGR curve returns to that in air. This hypothesis of dislocations escaping hydrogen is hence supported by the physical explanation by Amsterdam et al. [64].

8.3 Hydrogen-restricted dislocation zone

Murakami et al. [77] investigated hydrogen effect in types 304 and 316L stainless steel. The experiments revealed that there are fewer grains with slip bands in the specimens with higher hydrogen content, shown in Figure 56. It is attributed to the pinning effect of hydrogen on a dislocation. It is postulated that hydrogen trapped at a dislocation core in a dilatational stress field pins an edge location. A higher hydrogen concentration leads to a stronger pinning effect.

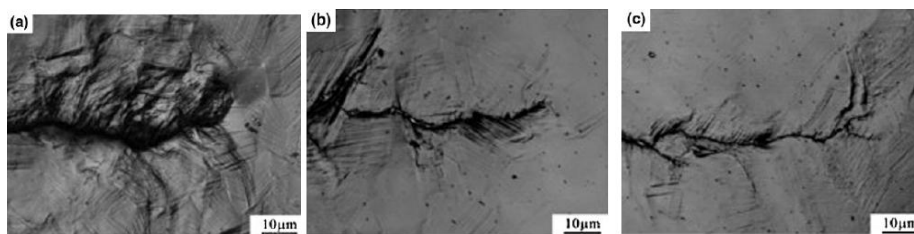


Figure 56 Slip deformation near fatigue crack tip in type 304 (a) uncharged; (b) H-charged $C_H=47.2$ wt ppm; (c) H-charged $C_H=89.2$ wt ppm [77]

Investigating the frequency effect on hydrogen assisted fatigue crack growth in low carbon steel, Yoshikawa et al. [34] also observed fewer slip bands along the crack when the hydrogen enhancement of the crack growth is significant, shown in Figure 57. This is assumed to be contributed by the localization of plastic deformation at the crack tip under the influence of hydrogen.

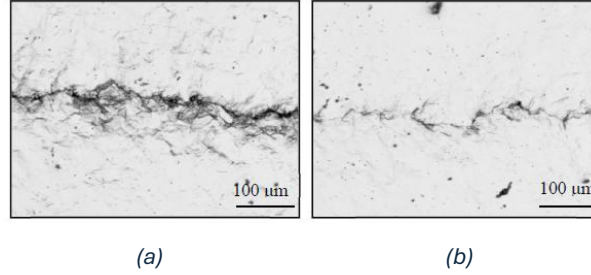


Figure 57 Crack appearance at specimen surface after fatigue test (a) in air; (b) in 0.7 MPa hydrogen

While investigating the effect of hydrogen on dislocation structures around a fatigue crack tip in a single crystalline iron-silicon alloy, Takahashi et al. [78] observed that the amount of dislocations emitted from the crack tip was reduced in the presence of hydrogen. The dislocations were discovered in close vicinity to the crack tip, triggering quasi-brittle fatigue crack growth. This phenomenon supports the hypothesis of hydrogen pinning of dislocations.

Although not all of the aforementioned literature specifically addresses carbon steel, the hydrogen pinning effect in metals is being discussed and acknowledged. This hypothesis is hereby adopted in this study. Because the dislocation movement is restrained by hydrogen, localized plasticity forms adjacent to the crack tip prompting brittle failure that is trans-granular quasi-cleavage fracture as reviewed in Chapter 6.3. Accordingly, a hydrogen-restricted dislocation zone (H-RDZ) in front of the crack tip, where the movement of dislocations is substantially hindered due to the hydrogen pinning effect, is introduced in this chapter.

Yoshikawa et al. [34] and Yamabe et al. [33] defined the depth of hydrogen penetration as $\sqrt{D_H t_H}$, where D_H is the hydrogen diffusivity coefficient, and $t_H = \frac{1}{2f}$. In this study, t_H is however defined as $\frac{1}{f}$, acknowledging the diffusion of hydrogen is continuous in one cycle. Within the zone of which hydrogen diffuses towards the edge in one cycle, it is assumed that there exists an area in which the dislocation movement is substantially restricted due to the hydrogen occupancy. This area hereby is defined as a hydrogen-restricted dislocation zone (H-RDZ) with a characteristic length r_H . Figure 58 illustrates H-RDZ within the reach of hydrogen diffusion.

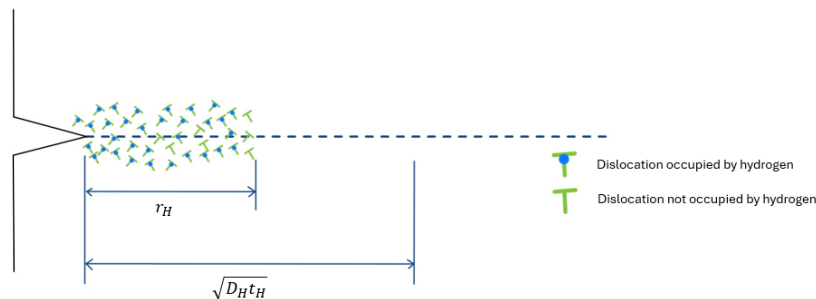


Figure 58 Illustration of H-RDZ

The characteristic length r_H is shorter than but proportional to the depth of hydrogen penetration, because it is required for hydrogen atoms to be present in order to increase the energy barrier for dislocation movement by occupying the dislocations. A deeper hydrogen penetration inherently provides a wider zone for the hydrogen occupation of dislocations to occur. Additionally, two factors are used to scale the hydrogen penetration depth in order to approximate r_H , namely the hydrogen pressure and the material yield strength.

Sieverts' law suggests that the hydrogen concentration at the crack surface C_s is proportional to the square root of hydrogen pressure, that is $C_s \propto \sqrt{P_H}$. Therefore, a higher hydrogen pressure indicates a higher hydrogen concentration which leads to a stronger pinning effect suggested by Murakami et al. [77]. A higher surface concentration of hydrogen inevitably leads to a higher number of dislocations occupied by hydrogen atoms immediately next to the crack tip. Once pinned by hydrogen, the dislocations in return act as obstacles to further restrict dislocation motion, forming an H-RDZ that is highly localized with densely populated immobilized dislocations. The characteristic length r_H correspondingly decreases with an increased hydrogen pressure. A smaller H-RDZ indicates less energy dissipation before failure, hence a more brittle fatigue response of the steel. A lower ΔK_2 representing the saturation point corresponds to a smaller H-RDZ, as a lower ΔK_2 results in a greater slope of the HA-FCGR curve in Region B implying the more brittle fatigue response. A term $\sqrt{\frac{P_H}{P_{re}}}$ is applied to characterize the effect of hydrogen pressure on the

H-RDZ size, which leads to $r_H \propto \frac{\sqrt{D_H t_H}}{\sqrt{\frac{P_H}{P_{re}}}}$ with P_{re} being a reference value of the hydrogen pressure. This

r_H is the inverse of the gradient of hydrogen concentration near the crack tip proposed by Yamabe et al. [33]. A novel parameter G_H that is positively correlated to $\frac{C_s}{\sqrt{D_H t_H}}$ is introduced by Yamabe et al. [33] to

quantify the gradient of hydrogen concentration. An onset hydrogen enhancement of the FCGR occurs when G_H exceeds a critical value. A higher $G_H \propto \frac{C_s}{\sqrt{D_H t_H}}$ that is the inverse of r_H indicates a lower r_H , which implies a lower ΔK_2 associated with a smaller H-RDZ representing a more brittle fatigue response. To

summarize, a shorter characteristic length of $r_H \propto \frac{\sqrt{D_H t_H}}{\sqrt{\frac{P_H}{P_{re}}}}$ corresponding to a lower ΔK_2 is indirectly

supported by the observation and hypothesis proposed by Yamabe et al. [33].

Courtney [75] summarized ways by which the flow strength of crystalline solids is increased by restricting dislocation motion. Different types of obstacles can be introduced into crystalline material to produce such effect. Most commonly employed obstacles are other dislocations, internal boundaries, solute atoms and second phase particles. Work hardening increases dislocation density in the material, which in return are

obstacles restricting the dislocation movement. Boundary strengthening introduces additional internal boundaries into the material which impedes dislocation motion along its entire slip plane length. If the yield strength of the steel is primarily increased through work hardening, the higher dislocation density serves two key roles. Firstly, it acts as an obstacle to hinder the dislocation movement. Secondly, it provides more trapping sites for hydrogen atoms. Hydrogen trapped at dislocations further impedes their movement, reducing the hydrogen restricted dislocation zone size r_H . Even in high-strength steels where dislocation density is not significantly increased through strengthening, dislocation movement remains restricted due to other obstacles introduced during the strengthening process. As a result, r_H still decreases. Courtney [75] provides the below equation describing the shear flow stress for work hardening:

$$\tau_y = \tau_i + \alpha_T G_s b_v \sqrt{\rho_d}, \quad (75)$$

where τ_i is the intrinsic strength of a material independent of dislocation interactions, α_T is a constant, G_s is the shear modulus that is $\frac{E}{2(1+\nu)}$, b_v is the Burger's vector, and ρ_d is the dislocation density. The intrinsic strength of the material τ_i is dropped from the equation to isolate the contribution from dislocations only. The shear flow stress τ_y is related to σ_y via the Schmid factor m_{Schmid} , such that $\sigma_y = \frac{\tau_y}{m_{Schmid}}$. Removing the constants α_T , G_s , b_v and ν , $\rho_d \approx (\frac{\sigma_y}{E})^2$.

In this study, $(\frac{\sigma_y}{E})^2$ is selected to represent the effect of yield strength on the hydrogen assisted plastic zone size.

An H-RDZ size r_H , based on the hydrogen penetration depth, affected by the hydrogen pressure and yield strength of the steel, is formulated as:

$$r_H \propto \frac{\sqrt{D_H t_H}}{\sqrt{\frac{P_H}{Pre} (\frac{\sigma_y}{E})^2}}, \quad (76)$$

8.4 Predictive model of ΔK_2

The K_{max} corresponding to ΔK can be written as $\Delta K/(1 - R)$. The corresponding plastic zone size r_y is in relation to $[\frac{\Delta K/(1-R)}{\sigma_y}]^2$, as:

$$r_y \propto [\frac{\Delta K/(1-R)}{\sigma_y}]^2, \quad (77)$$

Marrow et al. [79] introduced the notion of range of crack tip opening displacement per cycle, $\Delta\delta$, as follows:

$$\Delta\delta \propto \frac{\Delta K^2}{E\sigma_y}, \quad (78)$$

Marrow et al. [68] presented the fracture surface of ferritic stainless steel tested in hydrogen, and indicated that the brittle striation scale was comparable to the scale of $\Delta\delta$.

Investigating the fatigue response of carbon steel in gaseous hydrogen at high ΔK values where quasi-cleavage fracture appears, $\Delta\delta$ is selected in this study to represent the localized plastic zone in front the crack tip under cyclic loading.

At ΔK_2 , the hydrogen enhancement of the FCGR saturates. It is assumed in this study that above ΔK_2 , some dislocations can escape hydrogen due to the high applied stress intensity. The escaped dislocations produce a considerably similar plastic dissipation to that of fatigue in air. Agreeing to the conclusion by Amsterdam et al. [64] that the FCGR slope most likely represents the level of plastic dissipation at the crack tip, the slope of the HA-FCGR curve above ΔK_2 returns to that in air.

The H-RDZ represents a zone in front of the crack tip where the dislocation motion is substantially restricted. It is caused primarily by the hydrogen pinning effect, secondarily by the built-in obstacles in the material to impede dislocation movement.

In the absence of hydrogen, dislocations move along the slip plane to dissipate energy when a load is applied to the crack tip. When dislocation motion is impeded by obstacles such as other dislocations, grain boundaries or precipitates, the material dissipates less energy before failure leading to a lower fracture toughness, particularly in the form of inter-granular quasi-cleavage fracture. When this region in which the dislocation motion is restricted is relatively small, dislocation mobility is significantly inhibited, thereby substantially suppressing the plastic deformation at the crack tip. The combination of reduced energy dissipation and constrained plastic deformation results in lower fracture toughness and limited crack tip blunting at failure, accompanied by a smaller brittle zone in front of the crack tip. In contrast, a larger brittle zone permits greater dislocation movement before encountering obstacles. Consequently, higher fracture toughness and increased crack tip blunting at failure are expected due to the increased energy dissipation associated with plastic deformation.

The hydrogen pinning effect is comparable to the above mechanistic theory of fracture and dislocation motion. When hydrogen-pinned dislocations pile up in a smaller H-RDZ, the plastically active region immediately next to the crack tip is also smaller. With less energy dissipated at failure and more significantly suppressed plastic deformation associated with a smaller H-RDZ, lower fracture toughness and less crack tip blunting at failure are expected to appear. Kyriakopoulou et al. [80] investigated hydrogen embrittlement in X65 pipeline steel. For the X65 steel specimen subjected to in situ hydrogen cathodic

charging at 10 mA/cm^2 , the energy driving crack propagation, J integral, is calculated as 202.01 kN/m^2 , the elastic crack tip opening displacement δ is calculated as 0.0054 mm and the plastic δ is calculated as 1.44 mm . Following *in situ* hydrogen cathodic charging at 20 mA/cm^2 , the corresponding values were determined 175.8 kN/m^2 , 0.0037 mm and 0.98 mm . The results agree with the hypothesis proposed regarding the H-RDZ. A higher hydrogen concentration, equivalent to the higher hydrogen charging current, leads to a smaller H-RDZ thus lower fracture energy and less crack tip blunting at failure represented by the critical crack tip opening displacement, δ_{IC} .

Therefore, the characteristic length of this highly embrittled zone, r_H , is expected to be positively correlated to the range of crack tip opening displacement $\Delta\delta$ at ΔK_2 . The standard $\Delta\delta$ is expressed by Equation (78). It should be noted that the standard δ relation is built on linear fracture mechanics, assuming the plastic zone is bound by the elastic stress σ_y at radius r_y [81]. Owing to the hydrogen embrittlement, locally within the H-RDZ the material potentially reaches a higher stress before yielding, compared to the elastic yield stress σ_y of the steel. Equation (78) hence needs to be updated to:

$$\Delta\delta \propto \frac{\Delta K^2}{E \cdot \sigma_{y_local}}, \quad (79)$$

where σ_{y_local} is the local yield strength of the steel within the H-RDZ. Sey and Farhart [82] assessed the tensile properties of cold-finished mild steel, in order to understand the hydrogen embrittlement effect. Steel coupons were subjected to electrochemical hydrogen charging at various charging current densities, and tensile property tests were conducted immediately after the charging process. Figure 59 presents the experimental ultimate tensile and yield strength of the steel versus hydrogen content.

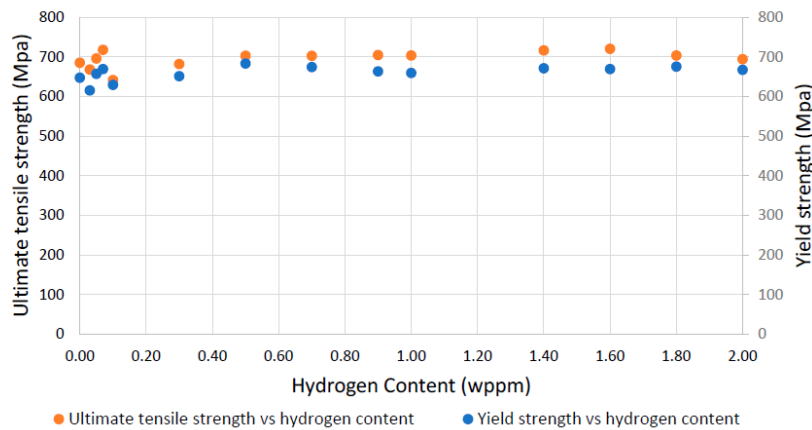


Figure 59 Experimental ultimate tensile and yield strength [82]

In the absence of hydrogen, the yield strength and the ultimate tensile strength of the mild (low carbon) steel are approximately 650 MPa and 700 MPa respectively. Increasing the hydrogen content from zero

to 2.00 *wppm*, both yield and ultimate tensile strength increase to a minor extent. The yield strength fluctuates slightly with the varying hydrogen content. It can be however concluded that the hydrogen content does not significantly impact the degree of increase in the yield strength. It is estimated that in the presence of hydrogen, the yield strength of the mild steel rises to roughly 680 *MPa*, that is 1.05 times the yield strength of the steel in the absence of hydrogen, 650 *MPa*.

Qu et al. [83] examined the hydrogen embrittlement on the base metal and the heat affected zone of X80 steel, through in-situ hydrogen charging. The yield strength of the base metal is 552 *MPa*.

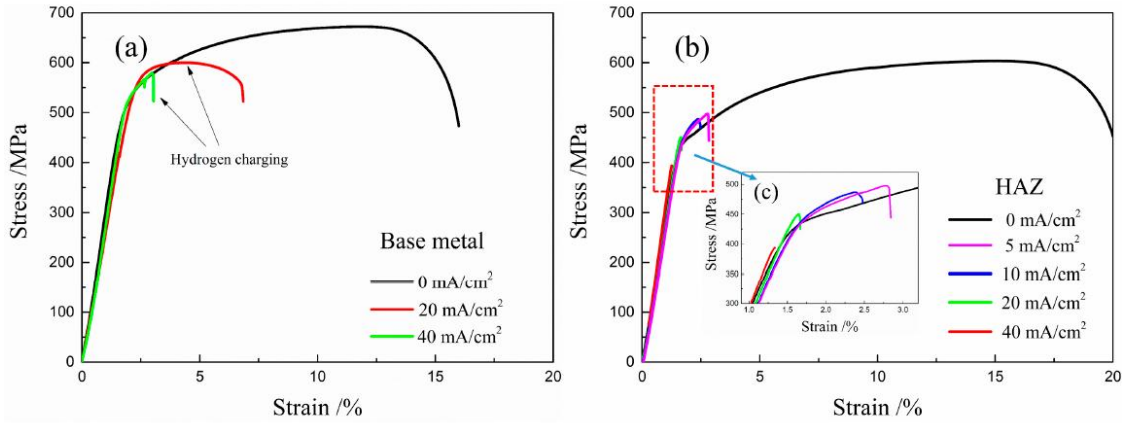


Figure 60 Stress-strain curves for the (a) base metal and (b) heat affected zone of the X80 steel tested at various hydrogen charging current densities [83]

The yield strength of the base metal increases in the presence of hydrogen. The degree of increment is ambiguous regardless of the hydrogen charging current densities. However, it can be concluded that the increase of yield strength due to hydrogen embrittlement is marginal. Shown on the stress-strain curve, the yield strength of the heat affected zone sample is approximately 450 *MPa* that is lower than the base metal. Increasing the hydrogen charging current density, the yield strength of the heat affected zone sample as well increases insignificantly. At 40 *mA/cm²*, the heat affected zone sample breaks before reaching to the yield strength. These test results by Qu et al. [83] furthermore support that the presence of hydrogen raises the yield strength of the material marginally, regardless of the hydrogen concentration or the yield strength of the material prior to hydrogen embrittlement.

As a result, it is deemed rational to assume in this study that the local yield strength of the steel within H-RDZ, σ_{y_local} , equals approximately 1.05 times the global yield strength σ_y . Equation (78) is then modified to:

$$\Delta\delta \propto \frac{\Delta K^2}{E \cdot 1.05 \cdot \sigma_y}, \quad (80)$$

The characteristic length of H-RDZ, r_H , is thus correlated to the range of crack tip opening displacement $\Delta\delta$ at ΔK_2 , applying the locally increased yield strength due to hydrogen embrittlement, expressed as follows:

$$r_H \propto \frac{\Delta K_2^2}{E \cdot 1.05 \cdot \sigma_y}, \quad (81)$$

Equation (81) illustrates that a smaller H-RDZ only marginally increases the local yield strength, so that the corresponding fracture toughness, represented by ΔK_2 here, is potentially lowered as well.

Combing Equation (76) and Equation (81) yields:

$$\frac{\Delta K_2^2}{E \cdot 1.05 \cdot \sigma_y} \propto \frac{\sqrt{D_H t_H}}{\sqrt{\frac{P_H}{P_{re}} \times \left(\frac{\sigma_y}{E}\right)^2}}, \quad (82)$$

where t_H is $\frac{1}{f}$, P_{re} is taken as 0.7 MPa which is the lowest hydrogen pressure within the collected fatigue test data, and the hydrogen diffusivity coefficient D_H (m^2/s) is expressed as:

$$D_H \propto \exp\left(-\frac{H_D}{R_g T}\right), \quad (83)$$

where H_D is the activation energy for the diffusion of hydrogen into α -iron, that is taken as 27000 J/mol.

Figure 61 illustrates this relation of r_H and $\Delta\delta$.

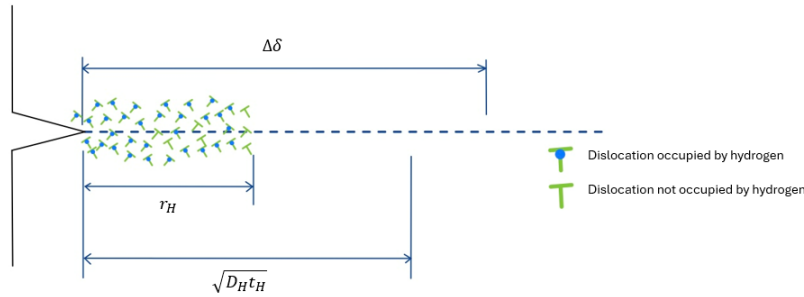


Figure 61 Relation of r_H and $\Delta\delta$

Rearranging Equation (82) leads to:

$$\Delta K_2 \propto \left(\frac{\sqrt{D_H t_H}}{\sqrt{\frac{P_H}{P_{re}} \times \left(\frac{\sigma_y}{E}\right)^2}} \times E \times 1.05 \sigma_y \right)^{0.5}, \quad (84)$$

Combining Equation (83) and (84) to express ΔK_2 as a function of the test parameters provides:

$$\Delta K_2 = fun\left[\left(\frac{\exp\left(-\frac{H_D}{R_g T}\right) \times t}{\sqrt{\frac{P_H}{P_{re}} \times \left(\frac{\sigma_y}{E}\right)^2}} \times E \times 1.05 \sigma_y\right)^{0.5}\right], \quad (85)$$

The final predictive model for ΔK_2 is established as:

$$\Delta K_2 = C_{21} \times \left[\left(\frac{\exp\left(-\frac{H_D}{R_g T}\right) \times \frac{1}{f}}{\sqrt{\frac{P_H}{P_{re}} \times \left(\frac{\sigma_y}{E}\right)^2}} \times 10^{-8} \right) \times E \times \sigma_y \right]^{0.5} + C_{22}, \quad (86)$$

where $r_H = \frac{\exp\left(-\frac{H_D}{R_g T}\right) \times \frac{1}{f}}{\sqrt{\frac{P_H}{P_{re}} \times \left(\frac{\sigma_y}{E}\right)^2}} \times 10^{-8} \text{ m}$, and the fitted constants $C_{21} = 1.9723103 \times 10^{-1}$ and $C_{22} =$

$10.931076 \text{ MPa}\sqrt{\text{m}}$.

8.5 Predicted ΔK_2

The predicted ΔK_2 is plotted against the experimental ΔK_2 collected from literature in Figure 62. The predicted ΔK_2 is in general trending to the experimental ΔK_2 .

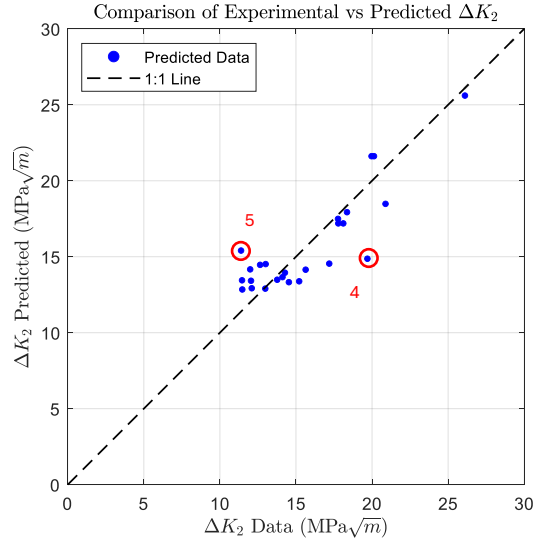


Figure 62 Comparison of predicted ΔK_2 and experimental ΔK_2

8.6 Discussion

Data sets 4 and 5 circled in Figure 62 show a relatively higher deviation of the predicted ΔK_2 from the experimental value; therefore, these two pairs of predicted and experimental ΔK_2 are further reviewed. The information correlated to these two data points are summarized in Table 13.

Table 13 Predicted ΔK_2 for further review

Date set	Reference	Figure	Material	P_H (MPa)	R	f (Hz)	T (K)	σ_y (MPa)	ΔK_2 Data (MPa \sqrt{m})	ΔK_2 Predicted (MPa \sqrt{m})
4	Slifka et al. [15]	Fig.12	X52 vintage	5.5	0.5	1.00	293	325	19.70	14.92
5	Slifka et al. [54]	Fig. 8	X100	7.0	0.5	0.10	293	705	11.39	15.46

The hydrogen pressure of the fatigue test corresponding to the data set 4 is 5.5 MPa, which is relatively low. The yield strength of the X52 vintage steel is determined to be 325 MPa, which is as well low. A relatively low surface hydrogen concentration combined with less obstacles in the material to restrict dislocation movement, it is predicted that r_H is greater with more energy dissipated through dislocation motion until failure. A higher value of ΔK_2 is expected. Reviewing the test parameters of the fatigue tests referenced in this study, 325 MPa is the lowest yield strength of the steels tested. It is possible that the predictive model proposed for ΔK_2 in this chapter does not accurately reflect the advantage of using a low strength steel. The effect of yield strength of the steel can be more heavily weighted if it is lower than a critical value, e.g. 360 MPa, that is the specified minimum yield strength of a common pipeline steel API 5L Grade X52.

Figure 63 presents the fitted curve to the experimental fatigue test data associated with data set 5. Potentially, fitted ΔK_2 can be updated to 12.5 MPa \sqrt{m} observing the fatigue test data. The level of overestimate can be lowered but the prediction is still 24% higher. The potential reason for this overestimation can be attributed to the low cyclic load frequency and high yield strength of the steel. The cyclic load frequency of the fatigue test corresponding to the data set 5 is 0.1 Hz, that is lower than the commonly applied 1 Hz among the fatigue tests referenced. Lower f leads to a higher hydrogen penetration depth, thus a higher r_H . A higher value of ΔK_2 is therefore predicted. However, the yield strength of the steel tested is 705 MPa, which is significantly higher than the strength of the pipeline steels used in the energy industry. The over-prediction indicates that if the yield strength of the material is high, the embrittling effect caused by the strengthening process of the steel potentially governs the fatigue response of the steel in hydrogen. The introduced additional dislocations or other obstacles to restrict dislocation movement through strengthening, limits the dislocation movement in the presence of hydrogen and enforces a small H-RDZ regardless of the test conditions. ΔK_2 can only reach a certain level due to limited energy dissipation.

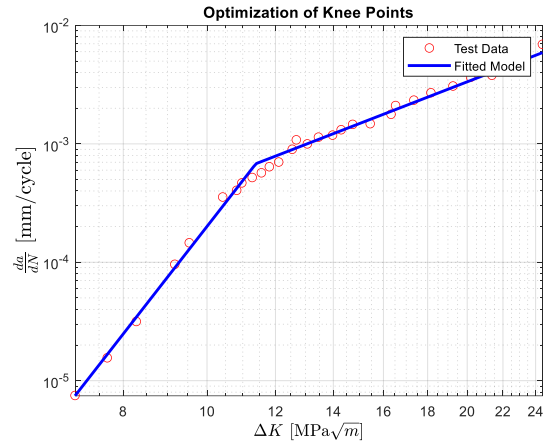


Figure 63 Fitted curve corresponding to Data point 5

It is discovered that the yield strength of the steel plays a critical role in predicting ΔK_2 . It should be noted that in this study, yield strength is selected to represent the microstructure of the material at a high level. When σ_y is below or above a critical value, the effect of σ_y , or the material microstructure becomes dominant governing the hydrogen assisted fatigue response.

9 HA-FCGR at hydrogen enhancement saturation

The crack growth rate $(\frac{da}{dN})_2$ represents the HA-FCGR once the effect of hydrogen on the FCGR saturates, corresponding to ΔK_2 . In this chapter, an effort is made to quantify $(\frac{da}{dN})_2$, using the known steel properties and fatigue test parameters provided in the fatigue test data. The previous experimental results collected from literature is utilized to provide experimentally determined $(\frac{da}{dN})_2$.

9.1 Relation to FPZ and $\Delta\delta_2$

Amaro et al [7] suggested that $(\frac{da}{dN})_2$ results from the interaction between the length of the crack extension per cycle and a characteristic length scale of the material microstructure. This characteristic length equals six times the FPZ size r_p given in Equation (4).

Marrow et al. [79] acknowledged that models for ductile striated fatigue crack growth consider the crack increment per cycle is proportional to the range of crack opening displacement per cycle, expressed as $\frac{da}{dN} \propto \Delta\delta \propto \frac{\Delta K^2}{E\sigma_y}$. Later, Marrow et al. [68] presented the fracture surface of ferritic stainless steel tested in hydrogen, and indicated that the brittle striation scale is comparable to the scale of the crack opening displacement range $\Delta\delta$.

Values of experimental $(\frac{da}{dN})_2$ collected from literature are compared to the characteristic length, $6r_p$, defined by Amaro et al [7] and $\Delta\delta_2$ that is the approximated $\Delta\delta$ at ΔK_2 equal to $\frac{\Delta K_2^2}{E\sigma_y}$ in Table 14. The coefficient of correlation between $\Delta\delta_2$ and $6r_p$ is 0.5762, indicating a moderate positive linear relationship. In comparison, the coefficient of correlation between $(\frac{da}{dN})_2$ and $6r_p$ is 0.3553, reflecting a weaker yet still positive linear association. This weaker correlation can be attributed to the effect of hydrogen on $(\frac{da}{dN})_2$, which is not captured by $6r_p$, thereby introducing variability that reduces the strength of the observed relationship.

Table 14 Comparison of experimental $(\frac{da}{dN})_2$, $6r_p$ and $\Delta\delta_2$

Reference	Figure	Material	P_H (MPa)	R	f (Hz)	T (K)	σ_y (Mpa)	$(\frac{da}{dN})_2$ (mm)	$6r_p$ (mm)	$\Delta\delta_2$ (mm)	$(\frac{da}{dN})_2/6r_p$	$(\frac{da}{dN})_2/\Delta\delta_2$
Amaro et al. [22]	Fig. 8	API-5L X100	1.7	0.5	1.00	293	689	8.32E-04	0.7922	0.0020	0.0011	0.41
Amaro et al. [22]	Fig. 8	API-5L X100	6.9	0.5	1.00	293	689	5.05E-04	0.5082	0.0013	0.0010	0.39
Drexler et al. [65]	Fig. 7	X70A	34.0	0.5	1.00	293	509	3.29E-04	0.7187	0.0014	0.0005	0.24
Drexler et al. [65]	Fig. 7	X70B	34.0	0.5	1.00	293	553	2.71E-04	0.5479	0.0011	0.0005	0.24
Matsuoka et al. [58]	Fig. 1	JIS-SM490B	0.7	0.1	1.00	298	360	4.07E-04	0.9568	0.0042	0.0004	0.10
Matsuoka et al. [58]	Fig. 1	JIS-SM490B	0.7	0.1	1.00	363	360	3.72E-04	1.2088	0.0053	0.0003	0.07
Matsuoka et al. [58]	Fig. 1	JIS-SM490B	10.0	0.1	1.00	423	360	5.48E-04	1.3227	0.0058	0.0004	0.09
Ronevich et al. [55]	Fig. 4	X52	21.0	0.5	1.00	295	360	5.45E-04	1.9570	0.0026	0.0003	0.21
Ronevich et al. [66]	Fig. 5	X100	21.0	0.5	1.00	295	690	5.39E-04	0.4508	0.0012	0.0012	0.46
Ronevich et al. [49]	Fig. 4	J00	21.0	0.1	1.00	293	429	5.07E-04	0.4940	0.0026	0.0010	0.20
Slifka et al. [54]	Fig. 6	X100	1.7	0.5	1.00	293	705	5.77E-04	0.4334	0.0011	0.0013	0.50
Slifka et al. [54]	Fig. 6	X100	7.0	0.5	1.00	293	705	4.58E-04	0.3361	0.0009	0.0014	0.52
Slifka et al. [54]	Fig. 8	X100	7.0	0.5	0.10	293	705	6.80E-04	0.3324	0.0009	0.0020	0.78
Slifka et al. [54]	Fig. 7	X52	7.0	0.5	1.00	293	426	7.01E-04	1.0088	0.0016	0.0007	0.44
Slifka et al. [15]	Fig. 12	X52 vintage	5.5	0.5	1.00	293	325	6.84E-04	4.6760	0.0057	0.0001	0.12
Slifka et al. [15]	Fig. 12	X52 vintage	34.5	0.5	1.00	293	325	3.79E-04	1.7487	0.0021	0.0002	0.18
Slifka et al. [15]	Fig. 12	X52 modified	5.5	0.5	1.00	293	487	4.12E-04	1.3125	0.0024	0.0003	0.17
Slifka et al. [15]	Fig. 16	X52 vintage	5.5	0.5	0.10	293	325	8.24E-04	4.0606	0.0049	0.0002	0.17
Slifka et al. [15]	Fig. 13	X70B	5.5	0.5	1.00	293	553	4.79E-04	0.8483	0.0018	0.0006	0.27
Slifka et al. [15]	Fig. 17	X70A	34.5	0.5	0.10	293	509	5.23E-04	0.7855	0.0015	0.0007	0.35
Yamabe et al. [33]	Fig. 5	JIS-SM490B	0.7	0.1	1.00	293	360	4.59E-04	0.9587	0.0042	0.0005	0.11
Yamabe et al. [33]	Fig. 5	JIS-SM490B	0.7	0.1	1.00	363	360	3.83E-04	1.2284	0.0054	0.0003	0.07
Yamabe et al. [33]	Fig. 5	JIS-SM490B	0.7	0.1	1.00	423	360	3.84E-04	2.0665	0.0090	0.0002	0.04
Yoshikawa et al. [34]	Fig. 5	JIS-SM490B	0.7	0.1	1.00	293	360	4.76E-04	0.9945	0.0043	0.0005	0.11
Zafra et al. [57]	Fig. 11 (Ronevich 2016)	X65	21.0	0.5	1.00	293	450	5.74E-04	1.3282	0.0022	0.0004	0.26

Figure 64 (a) and (b) further display the values of $(\frac{da}{dN})_2$, $\Delta\delta_2$ and $6r_p$, and the ratios of $(\frac{da}{dN})_2/6r_p$ and $(\frac{da}{dN})_2/\Delta\delta_2$, per individual fatigue test.

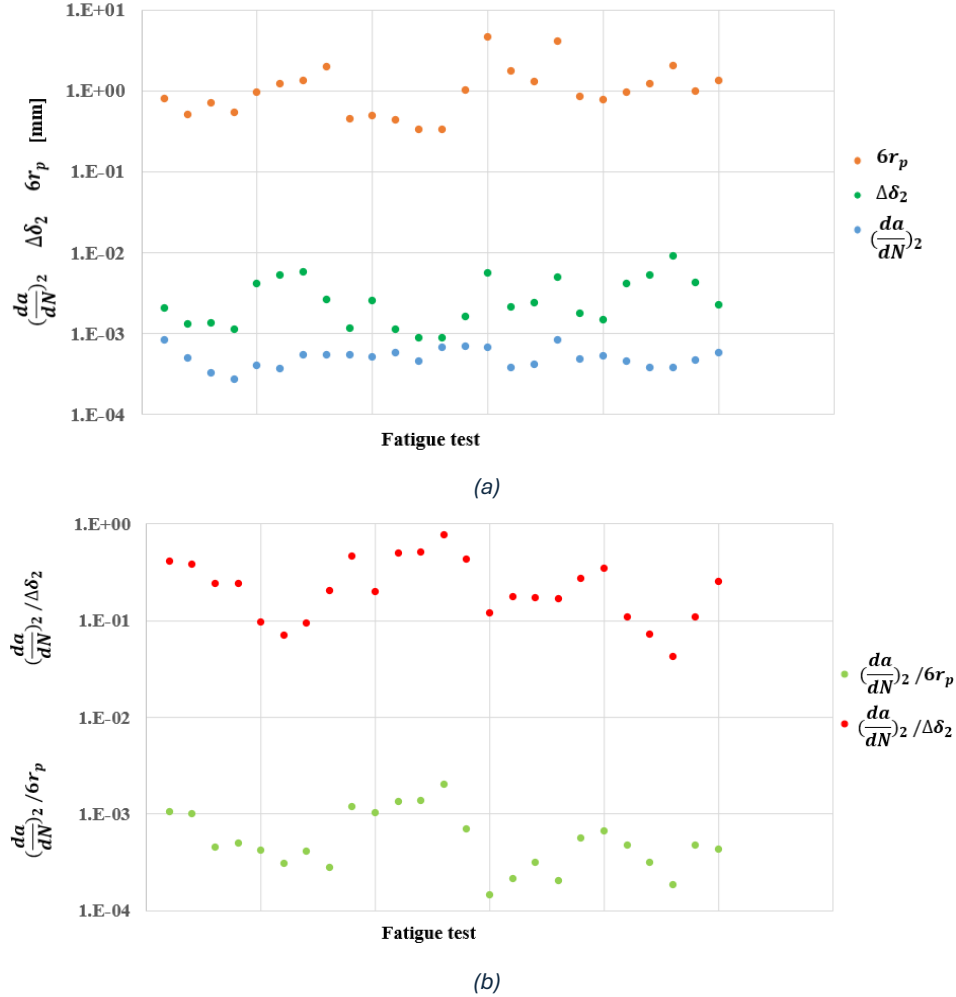


Figure 64 Comparison of (a) $(\frac{da}{dN})_2$, $\Delta\delta_2$ and $6r_p$; (b) $(\frac{da}{dN})_2/6r_p$ and $(\frac{da}{dN})_2/\Delta\delta_2$

9.2 Mechanistic theory

As shown in Figure 29, in Region C the Steady State Regime, the slope of the HA-FCGR curve returns to that of the FCGR curve of steel tested in air. A term that can be named maximum FCGR acceleration due to hydrogen effect in log scale, which equals to $\log\left(\frac{da}{dN}\right) - \log(a_{air}\Delta K^{B_{air}})$ becomes a constant independent of applied ΔK . It is rational to intend to extract this maximum FCGR acceleration from the total $\frac{da}{dN}$ because this term by definition is solely contributed by the hydrogen effect. Figure 65 presents the values of $(\frac{da}{dN})_2$, $(\frac{da}{dN})_{air}$ at ΔK_2 that is $(\frac{da}{dN})_{air_{\Delta K_2}} = a_{air}\Delta K_2^{B_{air}}$, and the maximum FCGR acceleration due to hydrogen effect at ΔK_2 that is $(\frac{da}{dN})_2 - (\frac{da}{dN})_{air_{\Delta K_2}}$, for each fatigue test referenced in this study. Since $(\frac{da}{dN})_{air_{\Delta K_2}}$ is almost one order of magnitude lower than $(\frac{da}{dN})_2$, the maximum FCGR acceleration is lower than but nearly equal to $(\frac{da}{dN})_2$, which is approximately one order of magnitude higher than

$\left(\frac{da}{dN}\right)_{air-\Delta K_2}$. Therefore, a prediction of the extracted maximum FCGR acceleration due to hydrogen effect at ΔK_2 does not differ notably from the prediction of $\left(\frac{da}{dN}\right)_2$. In this chapter, the focus is to propose a predictive model to quantify the total hydrogen assisted FCGR, $\left(\frac{da}{dN}\right)_2$.

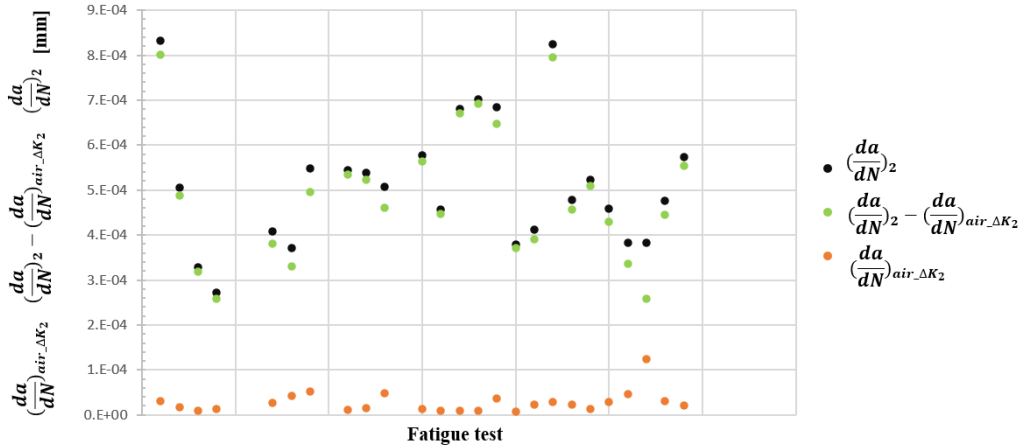


Figure 65 Comparison of $\left(\frac{da}{dN}\right)_2$ and maximum FCGR acceleration

Marrow et al. [68] found that in the strained region, a highly localized concentration of hydrogen is trapped in dislocations, far exceeding the equilibrium concentration of hydrogen at interstitial lattice sites. Cyclic cleavage is considered to possibly occur via the development of an embrittled zone in front of the crack tip. The intense strain in the embrittled zone causes a rapid increase in dislocation density. Dislocations may act as reversible hydrogen traps. Highly localized concentration of hydrogen trapped in the dislocations reduces the local fracture stress within the embrittled zone. It is suggested that the crack advances through the embrittled zone by hydrogen assisted cleavage, arresting once the hydrogen concentration drops below the critical level beyond the embrittled zone, illustrated in Figure 66. Trans-granular cleavage is observed in all three steels tested, namely Zeron 100 duplex stainless steel, E-Brite ferritic stainless steel, and BS 4360 50EE low alloy structural steel.

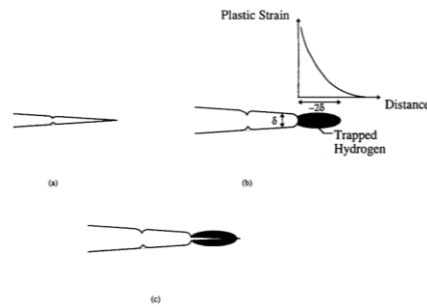


Figure 66 Schematic model of the mechanism of hydrogen assisted cyclic cleavage [68]

It is therefore concluded that the mechanism of hydrogen assisted fatigue crack propagation in low-to-medium strength steels is controlled by the interaction between hydrogen and microstructural traps. The intensity of embrittlement is governed by the occupancy of hydrogen traps. The hydrogen embrittlement declines with an increasing temperature shown from the previous fatigue test results. This can be caused by a reduced occupancy of hydrogen traps. The mobility of hydrogen atoms is promoted by an elevated temperature so that the hydrogen atoms are no longer stably trapped at the trapping sites.

Marrow et al. [68] directly suggested that the crack advances through the embrittled zone and arrests once the hydrogen concentration drops below a critical level beyond the embrittled zone. There are many factors that potentially influence the non-homogeneous distribution of hydrogen concentration along the crack path. The trap density and distribution of the material before and after deformation play an important role to alter the hydrogen distribution. The more hydrogen trapped in the trap sites, the less hydrogen can continue to diffuse through lattice. Dislocations form once the material is strained. The movement of dislocations can be restricted, or dislocations escape and emit along the slip plane. Hydrogen trapped in a dislocation hinders the dislocation velocity but can still diffuse and follow a moving dislocation. This phenomenon as well affects the hydrogen distribution. Additionally, to the best of the author's knowledge, no attempt has been made to quantify the critical hydrogen concentration below which crack propagation ceases in a specific steel. Therefore, in this study, this particular mechanistic theory is not further pursued.

Marrow et al. [68] suggested that the intensity of embrittlement is governed by the occupancy of hydrogen traps. Based on the observed relations described in Chapter 9.1, $(\frac{da}{dN})_2$ is proposed in this study to be the product of $\Delta\delta_2$ and a function of hydrogen occupancy, as follows:

$$\left(\frac{da}{dN}\right)_2 = \Delta\delta_2 \times fun(\theta_x), \quad (87)$$

where θ_x is the trap site occupancy of hydrogen, and $\Delta\delta_2 = \frac{\Delta K_2^2}{E\sigma_y}$.

In the following chapters, the above model to predict $(\frac{da}{dN})_2$ is further expanded, and results are displayed.

9.3 Predictive model of $(\frac{da}{dN})_2$

Matsuoka et al. [58] provided the relationship between the trap-site occupancy θ_x and the lattice site occupancy θ_L as follows:

$$\frac{\theta_x}{1-\theta_x} = \theta_L \exp\left(\frac{E_b}{R_g T}\right), \quad (88)$$

where E_b is the binding energy of a trap site. It is determined that trap sites with a binding energy of 47 kJ/mol , corresponding approximately to the dislocation core, dominate the temperature dependence of hydrogen enhanced FCG response. Therefore, E_b is considered to be 47 kJ/mol in this study. For a body cubic centered system, $\theta_x \gg \theta_L$. θ_L is expressed as:

$$\theta_L = 3.08 \times 10^{-4} \sqrt{F_u} \exp\left(\frac{-3440}{T}\right), \quad (89)$$

where F_u is the fugacity (MPa) given as:

$$F_u = P_H \exp\left(\frac{b_{AN} P_H}{R_g T}\right), \quad (90)$$

where b_{AN} is the Abel-Noble parameter taken to be $1.584 \times 10^{-5} m^3/mol$. θ_x can be then derived as:

$$\theta_x = \frac{\theta_L \exp\left(\frac{E_b}{R_g T}\right)}{1 + \theta_L \exp\left(\frac{E_b}{R_g T}\right)}, \quad (91)$$

As reviewed in Chapter 8.3, ways of strengthening crystalline solids introduce obstacles such as dislocations, internal boundaries, solute atoms and second phase particles to restrict dislocation motion. Most of these obstacles can serve as trap sites for hydrogen atoms. It is therefore rational to assume that the trap density is higher in steel with a higher yield strength. Employing the work hardening Equation (75), the trap density is approximated to be positively correlated to $\left(\frac{\sigma_y}{E}\right)^2$.

Given the same hydrogen trap occupancy, if the number of traps within a unit volume is high, it is reasonable to assume that the level of hydrogen embrittlement is raised. To account for the elevated hydrogen embrittlement due to the number of trap sites existing in the material before deformation, θ_x is multiplied by $\left(\frac{\sigma_y}{E}\right)^2$. The updated trap-site occupancy of hydrogen θ_{xm} , is given by:

$$\theta_{xm} = \theta_x \left(\frac{\sigma_y}{E}\right)^2, \quad (92)$$

The final prediction of $\left(\frac{da}{dN}\right)_2$ is provided as:

$$\begin{aligned} \left(\frac{da}{dN}\right)_2 &= \Delta\delta_2 \times fun(\theta_x) \\ &= \frac{\Delta K_2^2}{\sigma_y E} \times [C_{31} \times \exp(C_{32} \times \theta_{xm})], \end{aligned} \quad (93)$$

where fitted constants $C_{31} = 0.08065590$ and $C_{32} = 278766.00$. θ_x and θ_{xm} are dimensionless.

9.4 Predicted $\left(\frac{da}{dN}\right)_2$

For the results presented in this chapter, $\Delta\delta_2$ is calculated applying the ΔK_2 values obtained from Least Square curve fitting to the fatigue test results, namely fitted ΔK_2 .

The predicted values of $\left(\frac{da}{dN}\right)_2$ are plotted against experimental values of $\left(\frac{da}{dN}\right)_2$ collected from literature in Figure 67.

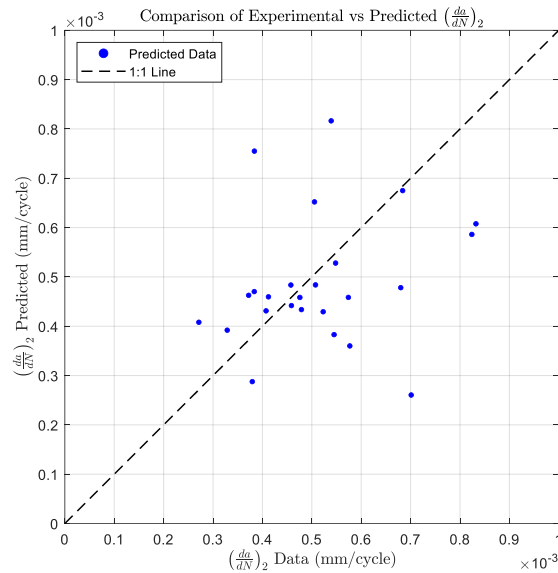


Figure 67 Comparison of predicted $\left(\frac{da}{dN}\right)_2$ and experimental $\left(\frac{da}{dN}\right)_2$, applying fitted ΔK_2

The predicted $\left(\frac{da}{dN}\right)_2$ is in general trending to the experimental $\left(\frac{da}{dN}\right)_2$.

9.5 Discussion

A higher degree of scatter can be seen from Figure 67 for the prediction of $\left(\frac{da}{dN}\right)_2$, comparing to the predictions of ΔK_1 and ΔK_2 shown in Chapter 7.5 and 8.5. There can be a difference of $\pm 0.5 \times 10^{-3}$ mm/cycle between the predicted and the experimental $\left(\frac{da}{dN}\right)_2$. One reason that potentially contributes to the scatter is that the absolute values of $\left(\frac{da}{dN}\right)_2$ are between 10^{-4} and 10^{-3} mm/cycle. A relatively small absolute value of prediction error can contribute to a highly scattered point. Other causes of the higher degree of scatter can be the uncertainties and assumptions involved in the mechanistic theories behind $\left(\frac{da}{dN}\right)_2$. The theory that the crack arrests at a critical low hydrogen concentration along the crack path is not further pursued in this study because it is not yet feasible to model the distribution of hydrogen

concentration and determine the critical hydrogen concentration by the microstructure of the steel, to a level of accuracy that is suitable for the purpose of this study. The applied model calculating hydrogen trap site occupancy includes predictive models, assumptions, and experimentally fitted constants. θ_x requires the expression of θ_L which alone is a predictive model. The trap binding energy is assumed to be the same for all traps that is 47 kJ/mol . Based on the strengthening process of the steel, traps with different binding energy can dominate in steels of different microstructures. Other than the experimentally fitted parameters included, θ_x is also multiplied by $(\frac{\sigma_y}{E})^2$, which approximates the trap density by the yield strength of the steel assuming work hardening as the dominating strengthening process. The factors discussed above may contribute to the greater degree of scatter of the final predicted $(\frac{da}{dN})_2$ values.

The model introduced in Chapter 9.3 to predict $(\frac{da}{dN})_2$ requires the calculation of the approximated $\Delta\delta$ at ΔK_2 , that is $\Delta\delta_2 = \frac{\Delta K_2^2}{E\sigma_y}$. To eliminate the model error associated with predicting ΔK_2 , the results presented in the Chapter 9.4 utilize the fitted ΔK_2 . However, in practical applications, an HA-FCGR curve must be predicted without the prior knowledge of a fitted ΔK_2 . ΔK_2 can be estimated in advance using the predictive model introduced in Chapter 8. $\Delta\delta_2$ can be calculated subsequently using the predicted ΔK_2 . The final predicted $(\frac{da}{dN})_2$ employing the modeled ΔK_2 is presented below in Figure 68.

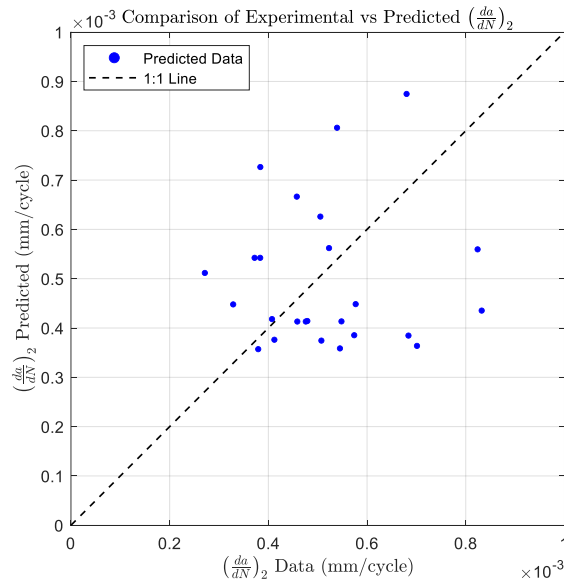


Figure 68 Comparison of predicted $(\frac{da}{dN})_2$ and experimental $(\frac{da}{dN})_2$, applying modeled ΔK_2

l

10 An updated Tri-Linear predictive model

A Tri-Linear predictive model to estimate hydrogen assisted fatigue crack growth rate is fully developed.

It is assumed that the coefficient and exponent of the Paris' relation, a_{air} and B_{air} , for an FCGR curve of steel tested in air, are known factors given the properties of the steel tested. It is commonly seen that the influence of temperature and cyclic load ratio are not considered. In this study, a_{air} and B_{air} are obtained from the FCGR curve of the same steel tested in air provided along with the HA-FCGR curve in the literature.

A model to predict ΔK_1 is introduced in Chapter 7. A predictive model for ΔK_2 is proposed in Chapter 8. Lastly, a model is suggested to predict $(\frac{da}{dN})_2$ in Chapter 9.

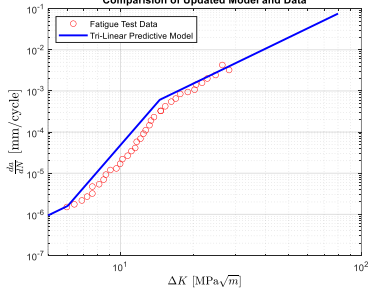
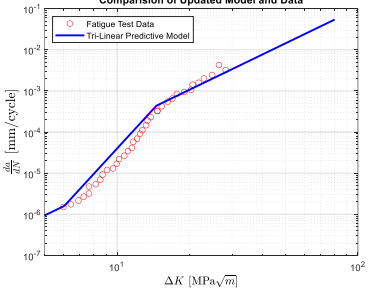
It is also assumed that once ΔK exceeds ΔK_2 , the slope of the HA-FCGR curve returns to the value of the FCGR curve of the same steel tested in air. This assumption is supported by the previous fatigue test results.

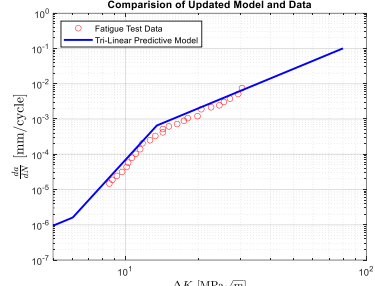
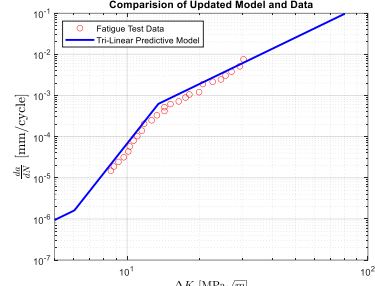
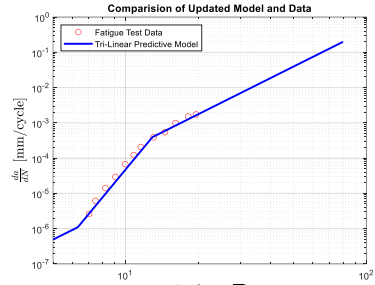
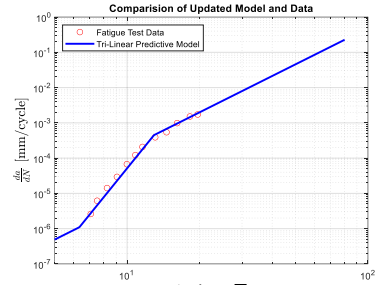
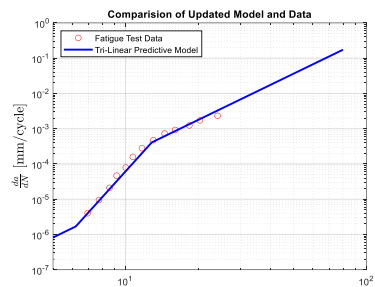
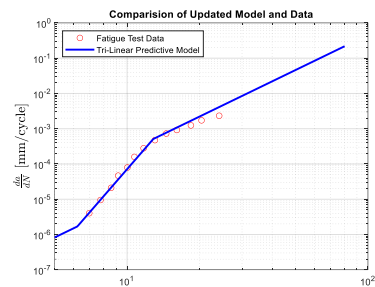
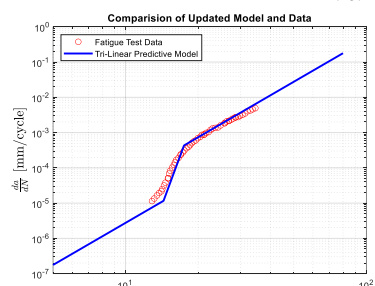
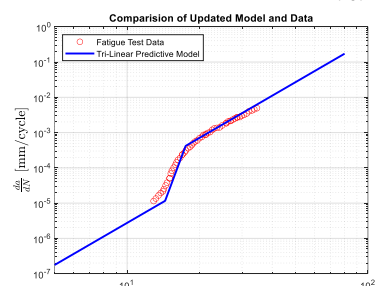
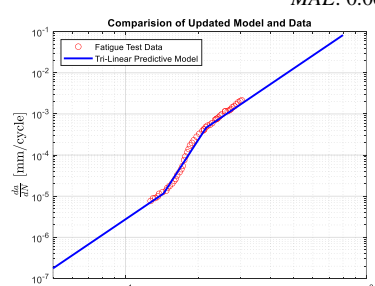
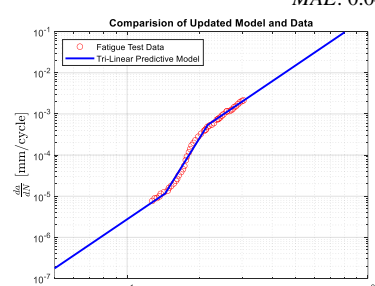
The final updated Tri-Linear model to predict HA-FCGR composed of two knee points namely ΔK_1 versus $(\frac{da}{dN})_1$ and ΔK_2 versus $(\frac{da}{dN})_2$ is presented by Equation (61).

The final complete Tri-Linear HA-FCGR curves based on the test parameters and steel properties along with the experimental data referenced are presented in Table 15. Results built on the fitted ΔK_2 and predicted ΔK_2 are both included. A mean absolute error of the model in logarithmic space as defined below, is also provided in Table 15 to indicate the level of predictive accuracy of the model.

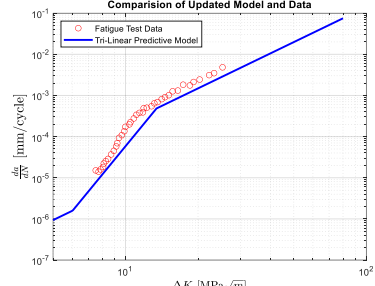
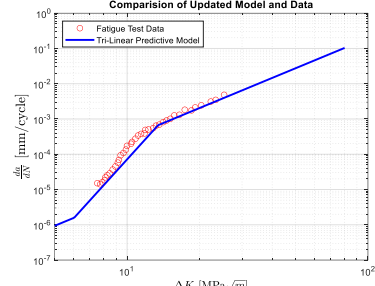
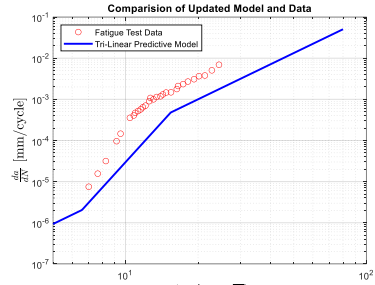
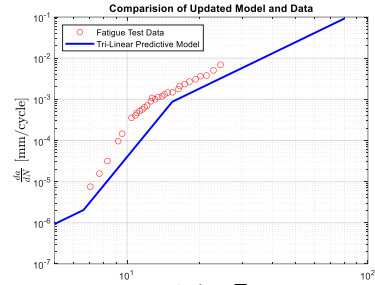
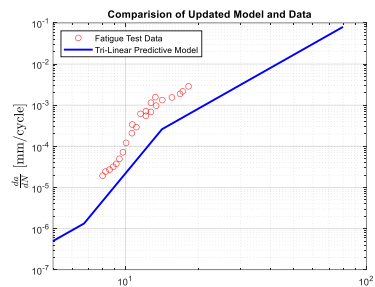
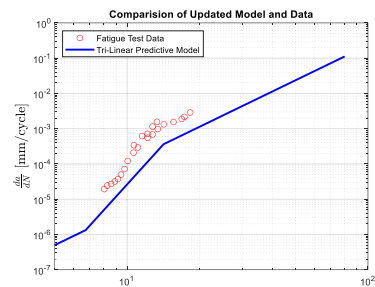
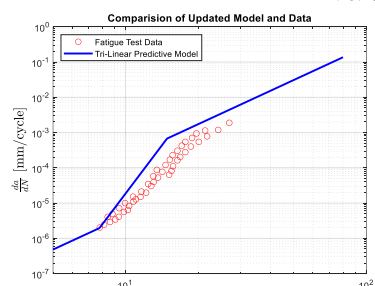
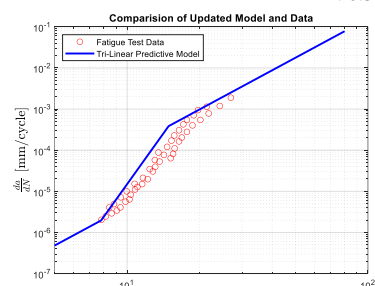
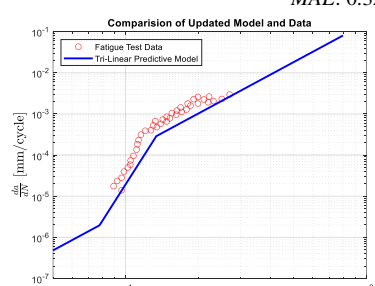
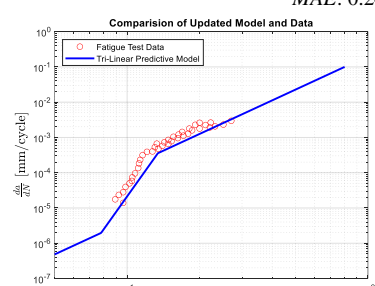
$$MAE = \frac{1}{N_{data}} \sum_{i=1}^{N_{data}} \left| \log_{10} \left(\frac{da}{dN} \right)_{data_i} - \log_{10} \left(\frac{da}{dN} \right)_{model_i} \right|, \quad (94)$$

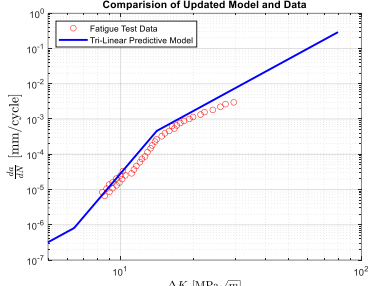
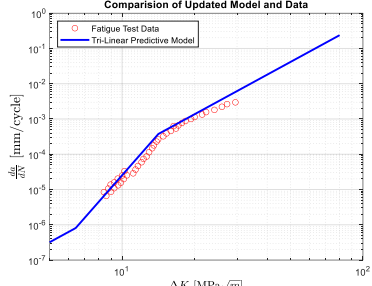
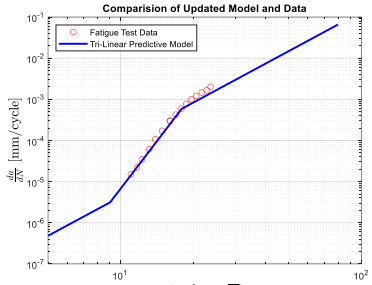
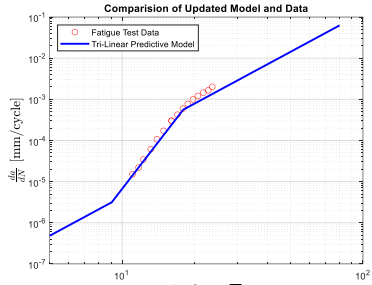
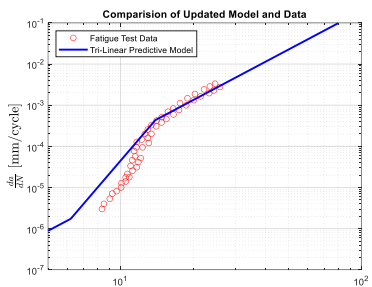
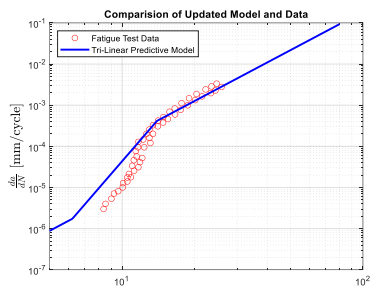
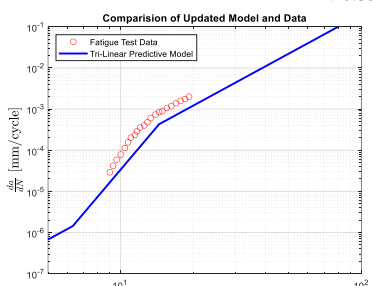
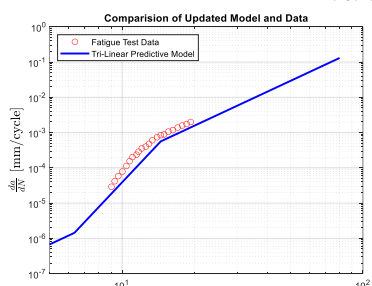
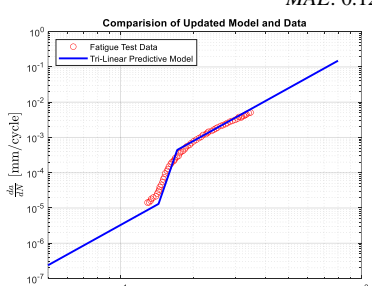
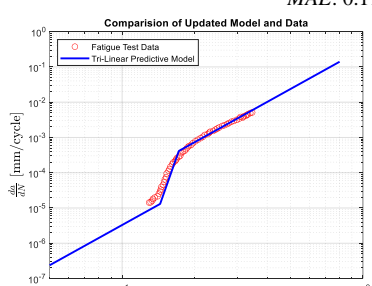
Table 15 HA-FCGR curves predicted by the updated model

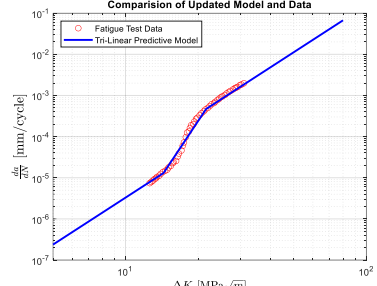
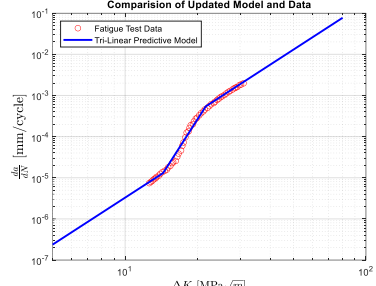
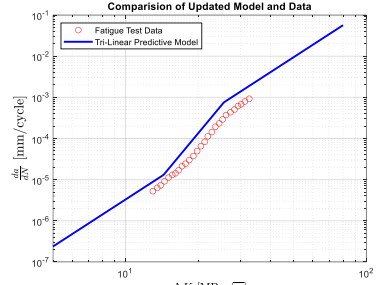
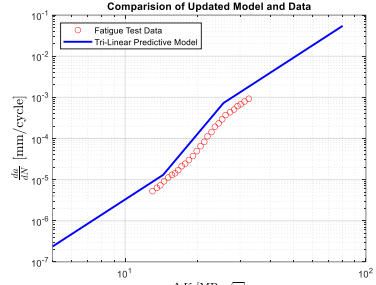
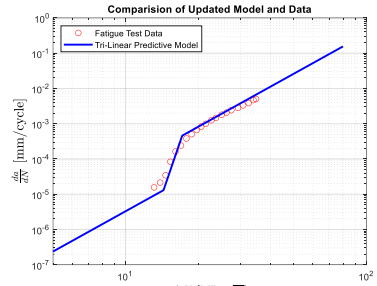
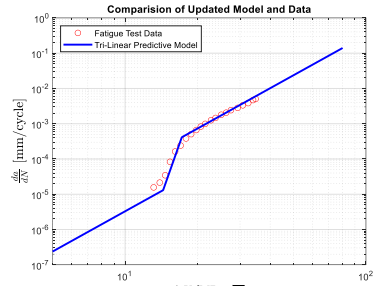
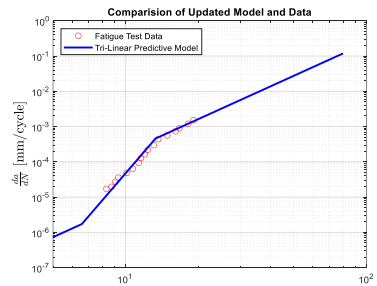
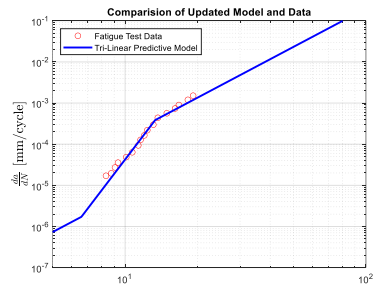
Reference	Test parameters		Tri-Linear HA-FCGR predictive model $(\frac{da}{dN})_2$ is based on fitted ΔK_2	Tri-Linear HA-FCGR predictive model $(\frac{da}{dN})_2$ is based on predicted ΔK_2
Amaro et al. [22]	Figure 8	Fig. 8	MAE: 0.2615	MAE: 0.1908
	Material	API-5L X100		
	P_H (MPa)	1.7		
	R	0.5		
	f (Hz)	1.00		
	T (K)	293		
	σ_y (MPa)	689		

<p>Amaro et al. [22]</p>	<p>Figure Material P_H (MPa) 6.9 R 0.5 f (Hz) 1.00 T (K) 293 σ_y (MPa) 689</p>	<p>Fig. 8 API-5L X100</p>	<p>MAE: 0.1593</p> 	<p>MAE: 0.1454</p> 
<p>Drexler et al. [65]</p>	<p>Figure Material P_H (MPa) 34.0 R 0.5 f (Hz) 1.00 T (K) 293 σ_y (MPa) 509</p>	<p>Fig. 7 X70A</p>	<p>MAE: 0.0916</p> 	<p>MAE: 0.0771</p> 
<p>Drexler et al. [65]</p>	<p>Figure Material P_H (MPa) 34.0 R 0.5 f (Hz) 1.00 T (K) 293 σ_y (MPa) 553</p>	<p>Fig. 7 X70B</p>	<p>MAE: 0.0781</p> 	<p>MAE: 0.0764</p> 
<p>Matsuoka et al. [58]</p>	<p>Figure Material P_H (MPa) 0.7 R 0.1 f (Hz) 1.00 T (K) 298 σ_y (MPa) 360</p>	<p>Fig. 1 JIS-SM490B</p>	<p>MAE: 0.1205</p> 	<p>MAE: 0.1139</p> 
<p>Matsuoka et al. [58]</p>	<p>Figure Material P_H (MPa) 0.7 R 0.1 f (Hz) 1.00 T (K) 363 σ_y (MPa) 360</p>	<p>Fig. 1 JIS-SM490B</p>	<p>MAE: 0.0661</p> 	<p>MAE: 0.0469</p> 

Matsuoka et al. [58]	<p>Figure Fig. 1 Material JIS-SM490B P_H (MPa) 10.0 R 0.1 f (Hz) 1.00 T (K) 423 σ_y (MPa) 360</p>		<p>MAE: 0.3203</p>	<p>MAE: 0.2487</p>
Ronevich et al. [55]	<p>Figure Fig. 4 Material X52 P_H (MPa) 21.0 R 0.5 f (Hz) 1.00 T (K) 295 σ_y (MPa) 360</p>		<p>MAE: 0.1683</p>	<p>MAE: 0.1901</p>
Ronevich et al. [66]	<p>Figure Fig. 5 Material X100 P_H (MPa) 21.0 R 0.5 f (Hz) 1.00 T (K) 295 σ_y (MPa) 690</p>		<p>MAE: 0.1264</p>	<p>MAE: 0.1229</p>
Ronevich et al. [49]	<p>Figure Fig. 4 Material J00 P_H (MPa) 21.0 R 0.1 f (Hz) 1.00 T (K) 293 σ_y (MPa) 429</p>		<p>MAE: 0.2159</p>	<p>MAE: 0.1542</p>
Slifka et al. [54]	<p>Figure Fig. 6 Material X100 P_H (MPa) 1.7 R 0.5 f (Hz) 1.00 T (K) 293 σ_y (MPa) 705</p>		<p>MAE: 0.2626</p>	<p>MAE: 0.2005</p>

Slifka et al. [54]	Figure Material P_H (MPa) R f (Hz) T (K) σ_y (MPa)	Fig. 6 X100 7.0 0.5 1.00 293 705	 <p>MAE: 0.2677</p>	 <p>MAE: 0.1651</p>
Slifka et al. [54]	Figure Material P_H (MPa) R f (Hz) T (K) σ_y (MPa)	Fig. 8 X100 7.0 0.5 0.10 293 705	 <p>MAE: 0.6844</p>	 <p>MAE: 0.4883</p>
Slifka et al. [54]	Figure Material P_H (MPa) R f (Hz) T (K) σ_y (MPa)	Fig. 7 X52 7.0 0.5 1.00 293 426	 <p>MAE: 0.7247</p>	 <p>MAE: 0.6245</p>
Slifka et al. [15]	Figure Material P_H (MPa) R f (Hz) T (K) σ_y (MPa)	Fig. 12 X52 vintage 5.5 0.5 1.00 293 325	 <p>MAE: 0.4953</p>	 <p>MAE: 0.3225</p>
Slifka et al. [15]	Figure Material P_H (MPa) R f (Hz) T (K) σ_y (MPa)	Fig. 12 X52 vintage 34.5 0.5 1.00 293 325	 <p>MAE: 0.3209</p>	 <p>MAE: 0.2484</p>

Slifka et al. [15]	<p>Figure Material X52 modified</p> <p>P_H (MPa) 5.5</p> <p>R 0.5</p> <p>f (Hz) 1.00</p> <p>T (K) 293</p> <p>σ_y (MPa) 487</p>	<p>Fig. 12</p>	<p>MAE: 0.1986</p> 	<p>MAE: 0.1414</p> 
Slifka et al. [15]	<p>Figure Material X52 vintage</p> <p>P_H (MPa) 5.5</p> <p>R 0.5</p> <p>f (Hz) 0.10</p> <p>T (K) 293</p> <p>σ_y (MPa) 325</p>	<p>Fig. 16</p>	<p>MAE: 0.0760</p> 	<p>MAE: 0.0912</p> 
Slifka et al. [15]	<p>Figure Material X70B</p> <p>P_H (MPa) 5.5</p> <p>R 0.5</p> <p>f (Hz) 1.00</p> <p>T (K) 293</p> <p>σ_y (MPa) 553</p>	<p>Fig. 13</p>	<p>MAE: 0.2598</p> 	<p>MAE: 0.2519</p> 
Slifka et al. [15]	<p>Figure Material X70A</p> <p>P_H (MPa) 34.5</p> <p>R 0.5</p> <p>f (Hz) 0.10</p> <p>T (K) 293</p> <p>σ_y (MPa) 509</p>	<p>Fig. 17</p>	<p>MAE: 0.3511</p> 	<p>MAE: 0.2572</p> 
Yamabe et al. [33]	<p>Figure Material JIS-SM490B</p> <p>P_H (MPa) 0.7</p> <p>R 0.1</p> <p>f (Hz) 1.00</p> <p>T (K) 293</p> <p>σ_y (MPa) 360</p>	<p>Fig. 5</p>	<p>MAE: 0.1200</p> 	<p>MAE: 0.1145</p> 

<p>Yamabe et al. [33]</p>	<p>Figure Material P_H (MPa) R f (Hz) T (K) σ_y (MPa)</p>	<p>Fig. 5 JIS-SM490B 0.7 0.1 1.00 363 360</p>	<p>MAE: 0.0566</p> 	<p>MAE: 0.0452</p> 
<p>Yamabe et al. [33]</p>	<p>Figure Material P_H (MPa) R f (Hz) T (K) σ_y (MPa)</p>	<p>Fig. 5 JIS-SM490B 0.7 0.1 1.00 423 360</p>	<p>MAE: 0.3238</p> 	<p>MAE: 0.3142</p> 
<p>Yoshikawa et al. [34]</p>	<p>Figure Material P_H (MPa) R f (Hz) T (K) σ_y (MPa)</p>	<p>Fig. 5 JIS-SM490B 0.7 0.1 1.00 293 360</p>	<p>MAE: 0.1135</p> 	<p>MAE: 0.0884</p> 
<p>Zafra et al. [57]</p>	<p>Figure Material P_H (MPa) R f (Hz) T (K) σ_y (MPa)</p>	<p>Fig. 11 (Ronevich 2016) X65 21.0 0.5 1.00 293 450</p>	<p>MAE: 0.0765</p> 	<p>MAE: 0.0678</p> 

11 Hypotheses of the frequency effect

11.1 Frequency effect on ΔK_1

Presented in Chapter 7.4, frequency is included in predicting ΔK_1 , by employing the gradient of hydrogen concentration term, $\sqrt{P_H f}$. A higher gradient of hydrogen concentration is expected to reduce the diameter of the voids d_0 further due to more localized slip deformation, compared to a lower gradient. A lower value of d_0 leads to a lower ΔK_1 . Matsuo et al. [59] demonstrated a decreasing ΔK_1 with f increasing from 0.01 Hz to 0.1 Hz to 5 Hz, for JIS-SCM435 steel of a yield strength of 767 MPa tested under 0.7 MPa hydrogen gas with a cyclic load ratio of 0.1, as shown in Figure 69. ΔK_1 corresponding to frequency of 0.01, 0.1 and 5 Hz are 50, 22 and 12 MPa \sqrt{m} denoted in Figure 69. The predicted ΔK_1 employing Equation (72) and (73) presented in Chapter 7 corresponding to frequency of 0.01, 0.1 and 5 Hz are 31.44, 21.05 and 10.83 MPa \sqrt{m} . The predicted ΔK_1 is 75%, 96% and 90% of the experimental ΔK_1 respectively. When the frequency is 0.01 Hz, the hydrogen gradient effect incorporated in the predictive model can be heightened more.

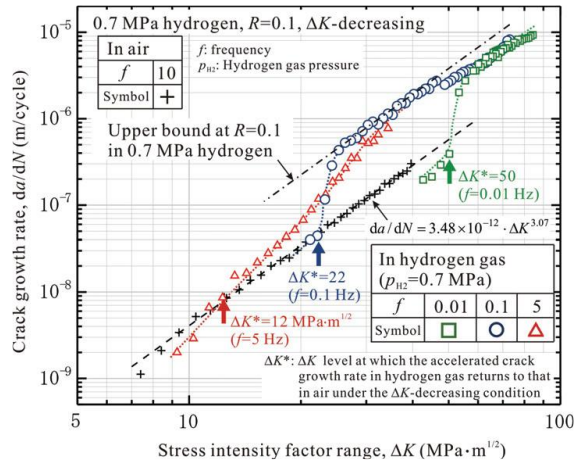


Figure 69 $\frac{da}{dN}$ - ΔK curve in 0.7 MPa hydrogen gas [59]

The increasing $\sqrt{P_H f}$ due to the increasing f is contributed to the decreasing hydrogen penetration depth per cycle, that is $\sqrt{D_H t_H}$. If f is increased continuously, $\sqrt{P_H f}$ tends to infinity while $\sqrt{D_H t_H}$ tends to zero. The realistic scenario is that after f reaches a critical value, the period of the load cycle is too short for sufficient hydrogen to enter the material to trigger the hydrogen enhancement of the FCGR. Above this critical f , an increasing f can potentially lead to a higher ΔK_1 which is equivalent to a less embrittled material by hydrogen. This phenomenon is not yet demonstrated in the previous fatigue tests.

11.2 Frequency effect on ΔK_2

Figure 69 demonstrates a decreasing ΔK_2 with load frequency increasing from 0.01 Hz to 0.1 Hz. However, increasing load frequency from 0.1 Hz to 5 Hz leads to a higher ΔK_2 value.

Frequency is included in predicting ΔK_2 , by employing the penetration depth of hydrogen that is $\sqrt{D_H t_H} = \sqrt{D_H/f}$. A higher frequency signals a shorter penetration depth of hydrogen, which directly links to a smaller hydrogen restricted dislocation zone, given all the other test parameters are the same. A smaller H-RDZ indicates a more brittle behaviour of the material responding to fatigue loading. Therefore, it is reasonable to observe a decreasing ΔK_2 with f increasing from 0.01 Hz to 0.1 Hz. Between 0.1 Hz and 5 Hz, similarly to the frequency effect on ΔK_1 , f reaches the critical value, above which the load cycle is too short for sufficient hydrogen to enter the material. As a result, the hydrogen effect is lowered hence ΔK_2 increases.

ΔK_2 corresponding to frequency of 0.01, 0.1 and 5 Hz are 60, 26 and 36 $MPa\sqrt{m}$ approximated from Figure 69. Equation (86) presented in Chapter 8 to predict ΔK_2 does not account for the phenomenon that the hydrogen embrittlement effect begins to diminish when the cyclic load frequency is above certain critical value. The predicted ΔK_2 corresponding to frequency of 0.01, 0.1 and 5 Hz are 24.50, 18.56 and 13.80 $MPa\sqrt{m}$. As expected, the predicted ΔK_2 decreases with an increasing f . However, the predictions are consistently lower than the experimental values. It is again possible that the frequency effect incorporated in the predictive model should be heightened more when the frequency is as low as 0.01 Hz. Additionally, the yield strength of the steel tested is 767 MPa, which is higher than the yield strength of a typical pipeline steel. The pressure of the hydrogen gas is 0.7 MPa which is the lowest pressure measured in the experimental data referenced. Potentially, under a low hydrogen pressure the effect of microstructure of the material represented by σ_y that is incorporated in the predictive model can be degraded accordingly when the yield strength is higher than a critical value as well.

It is worth noting that the range of critical frequency is not observed for ΔK_1 in Figure 69. This validates the hypothesis that failure mechanisms controlling ΔK_1 and ΔK_2 are different. ΔK_1 represents the minimum stress intensity factor range to trigger inter-granular fracture caused by void coalescence between the grain boundaries. ΔK_2 on other hand represents the stress intensity factor range at which the cyclic cleavage reaches the maximum extent and ductile crack propagation appears. The critical frequency above which not sufficient amount hydrogen enters the material to produce or maintain the hydrogen embrittlement mechanism is not the same for ΔK_1 and ΔK_2 .

11.3 Frequency effect on $\left(\frac{da}{dN}\right)_2$

Figure 69 displays a higher value of $\left(\frac{da}{dN}\right)_2$ coupled with a greater ΔK_2 . Equation (93) in Chapter 9, which predicts $\left(\frac{da}{dN}\right)_2$, is derived from the approximated $\Delta\delta$ at ΔK_2 that is $\Delta\delta_2$, adjusted according to the hydrogen occupancy at trap sites. Therefore, ΔK_2 plays a significant role in quantifying $\left(\frac{da}{dN}\right)_2$. The frequency effect in ΔK_2 as discussed in Chapter 11.2 is incorporated into $\left(\frac{da}{dN}\right)_2$ through Equation (93). The predicted $\left(\frac{da}{dN}\right)_2$ corresponding to frequency of 0.01, 0.1 and 5 Hz are 1.02×10^{-3} , 5.88×10^{-4} and 3.25×10^{-4} mm/cycle, which confirms that the predicted $\left(\frac{da}{dN}\right)_2$ is greater with a higher predicted ΔK_2 value.

11.4 Summary

The above observed frequency effects on the three key values associated with the HA-FCGR curve are ambiguous in other results of fatigue tests.

Slifka et al. [54] presented FCGR for X100 steel at 7 MPa hydrogen gas and f of 1 Hz and 0.1 Hz shown in Figure 70. With a lower frequency, it is possible that ΔK_2 of the HA-FCGR curve is slightly lower and the coupled $\left(\frac{da}{dN}\right)_2$ is lower as well, compared to the test results of a higher frequency. However, the conclusion can be obscure.

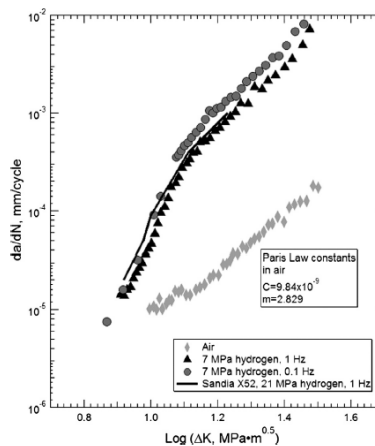


Figure 70 FCGR for X100 steel [54]

Slifka et al. [15] presented FCGR for modern and vintage X52 pipeline steels at 5.5 MPa hydrogen gas and f of 1 Hz, 0.1 Hz, and 0.01 Hz shown in Figure 71. For the vintage X52 steel, perhaps a lower ΔK_2 yet greater value of $\left(\frac{da}{dN}\right)_2$ are observed correlating to a lower frequency.

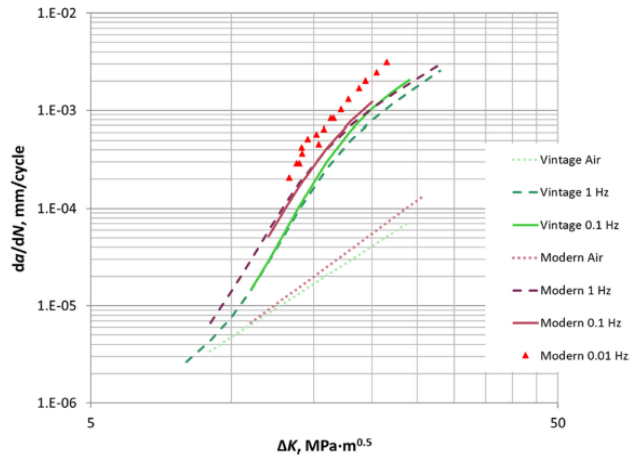


Figure 71 FCGR for modern and vintage X52 pipeline steels [15]

It is important to recognize that the experimental data referenced in this work is insufficient to draw definitive conclusions about the effect of frequency on the entire HA-FCGR curve.

The fatigue tests conducted by Matsuo et al. [59] involve pipeline steel with a yield strength of 767 MPa exposed to 0.7 MPa gaseous hydrogen. Experimental data on carbon steel with lower yield strength under higher hydrogen pressure is essential to investigate the critical frequencies associated with ΔK_1 and ΔK_2 . More fatigue testing can be strategically designed once a better understanding of the critical frequency is established for both low-strength steel at high pressure and high-strength steel at low pressure.

12 Conclusion and recommendation

An updated theoretical Tri-Linear model to predict HA-FCGR is proposed in this study. Given the pressure of the gaseous hydrogen, temperature, cyclic load frequency and load ratio, and the yield strength of the steel, $\frac{da}{dN}$ can be predicted using the applied ΔK employing this predictive model.

The Tri-Linear predictive model follows the three regions A, B and C categorized by Amaro et al. [7]. In Region A, the HA-FCGR closely resembles the FCGR of the same steel tested in air. The multiplier a_{air} and coefficient B_{air} of the Paris' relation are known parameters that are extracted from the referenced literature data. In Region B, the FCGR is accelerated by hydrogen with the slope of the HA-FCGR curve greater than B_{air} . In Region C, hydrogen enhancement saturates and the slope of the HA-FCGR curve returns to that of the FCGR curve in air that is B_{air} .

The HA-FCGR curve is developed by predicting the two knee points that define the three regions. Three key values are associated with the two knee points, namely ΔK_1 , ΔK_2 and $(\frac{da}{dN})_2$. ΔK_1 represents the onset of hydrogen enhancement of the FCGR at which brittle inter-granular fracture appears due to micro voids coalescence along the grain boundaries. The prediction of ΔK_1 hence is built on prediction of a threshold stress intensity factor taking into account the void growth d_0 and the ligament length between voids l_0 . Ductile tearing at grain boundaries then quasi-cleavage marks begin to appear while ΔK approaches ΔK_2 .

Above ΔK_2 , trans-granular quasi-cleavage fracture combined with ductile crack propagation appears on the fatigue failure surface. ΔK_2 and $(\frac{da}{dN})_2$ represent the knee point where the hydrogen embrittlement effect saturates so that the slope of the HA-FCGR curve returns to that of the FCGR curve for the same steel tested in air. It is assumed that above ΔK_2 , a number of dislocations escape hydrogen due to the high applied stress intensity. The escaped dislocations produce a considerably similar plastic dissipation to that of fatigue in air. As a result, the slope of the HA-FCGR curve above ΔK_2 restores to that in air, and the fracture surface is dominated by quasi-cleavage facets with ductile crack propagation beginning to appear.

A hydrogen restricted dislocation zone is introduced with a characteristic length r_H . ΔK_2 is correlated to r_H through the range of the crack tip opening displacement $\Delta\delta$. The prediction of $(\frac{da}{dN})_2$ is constructed upon the range of the crack tip opening displacement resulting from ΔK_2 , adjusted by hydrogen occupancy of the trap sites.

Frequency is incorporated into the prediction of ΔK_1 by factoring in the impact of hydrogen gradient $\sqrt{P_H f}$ on d_0 . The characteristic length r_H is directly shaped by the hydrogen penetration depth $\sqrt{D_H/f}$, and is

linked to $\Delta\delta$. Through r_H and $\Delta\delta$, frequency is integrated into the prediction of ΔK_2 as well the prediction of $(\frac{da}{dN})_2$.

$\Delta\delta$ is a measurable parameter during fatigue testing. The proposed predictive models for ΔK_2 and $(\frac{da}{dN})_2$ can be further verified by the measurement of $\Delta\delta$ when achieving ΔK_2 and $(\frac{da}{dN})_2$ in a fatigue test of steel in hydrogen.

Frequency is effectively integrated into the Tri-Linear predictive model for the HA-FCGR. However, based on the limited data available in the referenced literature, there appears to be a critical frequency above which the effect of hydrogen embrittlement begins to diminish. This threshold varies due to the differences in failure mechanisms associated with ΔK_1 and ΔK_2 . Therefore, further investigation is essential to determine critical frequency values across various steels and testing conditions.

The proposed Tri-Linear HA-FCGR model provides reliable predictions with some limitations. The predictive model for ΔK_1 does not account for the temperature effect. The previous fatigue test results clearly exhibit mitigated hydrogen embrittlement with elevated temperature. Therefore, this model produces a lowered value of ΔK_1 if the test or operating temperature is considerably above room temperature. In this study, σ_y represents the microstructure of the steel, and it appears that σ_y plays a crucial role altering the values of ΔK_1 and ΔK_2 . The yield strength σ_y is between 325 MPa and 705 MPa within the fatigue test data referenced. At the minimum 325 MPa and maximum 705 MPa, it suggests that the predictive model does not fully convey the influence of the microstructure of the original material. The pressure of the hydrogen gas is between 0.7 MPa and 34.5 MPa within the fatigue test data referenced. It may be also inferred that σ_y and P_H are in competing mode to dominate the fatigue response of the steel in the presence of hydrogen. When σ_y is at the minimum 325 MPa, the microstructure of the steel dominates the fatigue response. With less obstacles introduced in the steel to restrict dislocation movement, the hydrogen embrittlement is effectively weakened. When P_H is at the minimum 0.7 MPa, the hydrogen pressure becomes dominant in the fatigue response assisted by hydrogen. With less hydrogen adsorbed onto and absorbed into the material, higher values are expected for ΔK_1 and ΔK_2 due to the reduced hydrogen enhancement in the fatigue response, minimizing the impact of higher number of obstacles introduced into the higher strength steel.

To ensure the Tri-Linear model provides reliable predictions of HA-FCGR across a wide range of steels and test conditions, further investigation of these competing and coupled variables is necessary to accurately reflect their realistic impact on the hydrogen assisted fatigue response.

Reference:

- [1] F. Qney, T. N. Veziroglu, and Z. Dulger, "Evaluation of Pipeline Transportation of Hydrogen and Natural Gas Mixtures," *Int. J. Hydrogen Energy*, vol. 19, no. 10, p. 813, 1994.
- [2] R. Carvalho, L. Buzna, F. Bono, E. Gutiérrez, W. Just, and D. Arrowsmith, "Robustness of trans-European gas networks," *Phys Rev E Stat Nonlin Soft Matter Phys*, vol. 80, no. 1, Aug. 2009, doi: 10.1103/PhysRevE.80.016106.
- [3] S. Lynch, "Hydrogen embrittlement phenomena and mechanisms," *Corrosion Reviews*, vol. 30, no. 3–4, pp. 105–123, Jun. 2012, doi: 10.1515/correv-2012-0502.
- [4] A. Islam, T. Alam, N. Sheibley, K. Edmonson, D. Burns, and M. Hernandez, "Hydrogen blending in natural gas pipelines: A comprehensive review of material compatibility and safety considerations," Dec. 03, 2024, *Elsevier Ltd.* doi: 10.1016/j.ijhydene.2024.10.384.
- [5] J. Zhao *et al.*, "Effect of Pressure Sampling Methods on Pipeline Integrity Analysis," *J Pipeline Syst Eng Pract*, vol. 8, no. 4, Nov. 2017, doi: 10.1061/(asce)ps.1949-1204.0000273.
- [6] J. H. Lienhard, "Synopsis of Lift, Drag, and Vortex Frequency Data for Rigid Circular Cylinders," 1966.
- [7] R. L. Amaro, R. M. White, C. P. Looney, E. S. Drexler, and A. J. Slifka, "Development of a Model for Hydrogen-Assisted Fatigue Crack Growth of Pipeline Steel1," *Journal of Pressure Vessel Technology, Transactions of the ASME*, vol. 140, no. 2, Apr. 2018, doi: 10.1115/1.4038824.
- [8] *Hydrogen Piping and Pipelines ASME Code for Pressure Piping, B31 ASME B31.12-2023*. U.S.A., 2023.
- [9] T. L. Anderson, *Fracture Mechanics - Fundamentals and Applications*, 3rd ed. CRC Press, 2005.
- [10] M. Truschner, A. Trautmann, and G. Mori, "The Basics of Hydrogen Uptake in Iron and Steel," *BHM Berg- und Hüttenmännische Monatshefte*, vol. 166, no. 9, pp. 443–449, Sep. 2021, doi: 10.1007/s00501-021-01142-x.
- [11] N. Nanninga, A. Slifka, Y. Levy, and C. White, "A Review of Fatigue Crack Growth for Pipeline Steels Exposed to Hydrogen," *J Res Natl Inst Stand Technol*, vol. 115, pp. 437–452, 2010.
- [12] M. L. Martin, M. J. Connolly, F. W. Delrio, and A. J. Slifka, "Hydrogen embrittlement in ferritic steels," Dec. 01, 2020, *American Institute of Physics Inc.* doi: 10.1063/5.0012851.
- [13] R. A. Oriani and P. H. Josephic, "Equilibrium Aspects of Hydrogen-Induced Cracking of Steels," *ACTA Metallurgica*, vol. 22, pp. 1065–1074, 1974.
- [14] P. Sofronis and R. M. McMeeking, "Numerical Analysis of Hydrogen Transport near a Blunting Crack Tip," *J. Mech. Phys. Solids*, vol. 37, no. 3, pp. 317–350, 1989.
- [15] A. J. Slifka *et al.*, "Fatigue measurement of pipeline steels for the application of transporting gaseous hydrogen," *Journal of Pressure Vessel Technology, Transactions of the ASME*, vol. 140, no. 1, Feb. 2018, doi: 10.1115/1.4038594.
- [16] C. Moriconi, G. Hénaff, and D. Halm, "Cohesive zone modeling of fatigue crack propagation assisted by gaseous hydrogen in metals," *Int J Fatigue*, vol. 68, pp. 56–66, 2014, doi: 10.1016/j.ijfatigue.2014.06.007.

- [17] A. Golahmar, P. K. Kristensen, C. F. Niordson, and E. Martínez-Pañeda, "A phase field model for hydrogen-assisted fatigue," *Int J Fatigue*, vol. 154, Jan. 2022, doi: 10.1016/j.ijfatigue.2021.106521.
- [18] S. Serebrinsky, E. A. Carter, and M. Ortiz, "A quantum-mechanically informed continuum model of hydrogen embrittlement," *J Mech Phys Solids*, vol. 52, no. 10, pp. 2403–2430, Oct. 2004, doi: 10.1016/j.jmps.2004.02.010.
- [19] R. L. Amaro, E. S. Drexler, and A. J. Slifka, "Fatigue crack growth modeling of pipeline steels in high pressure gaseous hydrogen," *Int J Fatigue*, vol. 62, pp. 249–257, 2014, doi: 10.1016/j.ijfatigue.2013.10.013.
- [20] S. Suresh and R. O. Ritchie, "Mechanistic Dissimilarities Between Environmentally-Influenced Fatigue-Crack Propagation at Near-Threshold and High Growth Rates in Lower-Strength Steels," *Metal Science*, pp. 529–538, 1981.
- [21] K. A. Nibur, B. P. Somerday, C. S. Marchi, J. W. Foulk, M. Dadfarnia, and P. Sofronis, "The relationship between crack-tip strain and subcritical cracking thresholds for steels in high-pressure hydrogen gas," *Metall Mater Trans A Phys Metall Mater Sci*, vol. 44, no. 1, pp. 248–269, Jan. 2013, doi: 10.1007/s11661-012-1400-5.
- [22] R. L. Amaro, N. Rustagi, K. O. Findley, E. S. Drexler, and A. J. Slifka, "Modeling the fatigue crack growth of X100 pipeline steel in gaseous hydrogen," *Int J Fatigue*, vol. 59, pp. 262–271, 2014, doi: 10.1016/j.ijfatigue.2013.08.010.
- [23] J. W. Hutchinson, "Singular Behaviour at the End of a Tensile Crack in a Hardening Material," *J. Mech. Phys. Solids*, vol. 16, pp. 13–31, 1968.
- [24] J. R. Rice and G. F. Rosengren, "Plane Strain Deformation Near a Crack Tip in a Power-Law Hardening Material," *J. Mech. Phys. Solids*, vol. 16, pp. 1–12, 1968.
- [25] *ASME Boiler and Pressure Vessel Code Section VIII Division 3*. The American Society of Mechanical Engineers, 2019.
- [26] E. Martínez-Pañeda, C. F. Niordson, and R. P. Gangloff, "Strain gradient plasticity-based modeling of hydrogen environment assisted cracking," *Acta Mater*, vol. 117, pp. 321–332, Sep. 2016, doi: 10.1016/j.actamat.2016.07.022.
- [27] S. del Busto, C. Betegón, and E. Martínez-Pañeda, "A cohesive zone framework for environmentally assisted fatigue," *Eng Fract Mech*, vol. 185, pp. 210–226, Nov. 2017, doi: 10.1016/j.engfracmech.2017.05.021.
- [28] R. Fernández-Sousa, C. Betegón, and E. Martínez-Pañeda, "Cohesive zone modelling of hydrogen assisted fatigue crack growth: The role of trapping," *Int J Fatigue*, vol. 162, Sep. 2022, doi: 10.1016/j.ijfatigue.2022.106935.
- [29] A. H. M. Krom, R. W. J. Koers, and A. Bakker, "Hydrogen transport near a blunting crack tip," *J Mech Phys Solids*, vol. 36, pp. 888–860, 1998.
- [30] H. W. Lee, M. B. Djukic, and C. Basaran, "Modeling fatigue life and hydrogen embrittlement of bcc steel with unified mechanics theory," *Int J Hydrogen Energy*, vol. 48, no. 54, pp. 20773–20803, Jun. 2023, doi: 10.1016/j.ijhydene.2023.02.110.

- [31] Z. S. Hosseini *et al.*, “Mechanistic model for hydrogen accelerated fatigue crack growth in a low carbon steel,” *Int J Hydrogen Energy*, 2024, doi: 10.1016/j.ijhydene.2024.05.351.
- [32] X. Xing, W. Chen, and H. Zhang, “Prediction of crack propagation under cyclic loading based on hydrogen diffusion,” *Mater Lett*, vol. 152, pp. 86–89, Aug. 2015, doi: 10.1016/j.matlet.2015.03.045.
- [33] J. Yamabe, M. Yoshikawa, H. Matsunaga, and S. Matsuoka, “Effects of Hydrogen Pressure, Test Frequency and Test Temperature on Fatigue Crack Growth Properties of Low-carbon Steel in Gaseous Hydrogen,” in *Procedia Structural Integrity*, Elsevier B.V., 2016, pp. 525–532. doi: 10.1016/j.prostr.2016.06.068.
- [34] M. Yoshikawa, T. Matsuo, N. Tsutsumi, H. Matsunaga, and S. Matsuoka, “Effects of Hydrogen Gas Pressure and Test Frequency on Fatigue Crack Growth Properties of Low Carbon Steel in 0.1-90 MPa Hydrogen Gas,” *Transactions of the JSME (in Japanese)*, vol. 80, no. 817, pp. SMM0254–SMM0254, 2014, doi: 10.1299/transjsme.2014smm0254.
- [35] R.P. Wei and G.W. Simmons, “Environment Enhanced Fatigue Crack Growth in High-Strength Steels,” Mar. 1973.
- [36] P. Hotobut, “Fatigue crack growth model for a thin steel plate containing hydrogen,” *Int J Fatigue*, vol. 32, no. 12, pp. 1895–1903, Dec. 2010, doi: 10.1016/j.ijfatigue.2010.06.005.
- [37] J. Ronevich, M. Agnani, and C. San Marchi, “Consistency of fatigue crack growth behavior of pipeline and low-alloy pressure vessel steels in gaseous hydrogen,” *Int J Hydrogen Energy*, 2024, doi: 10.1016/j.ijhydene.2024.06.287.
- [38] A.J. McEvily and R.P. Wei, “Fracture Mechanics and Corrosion Fatigue,” 1972.
- [39] R.P. Wei and Gunchoo Shim, “Fracture Mechanics and Corrosion Fatigue,” 1981.
- [40] R. L. Amaro, R. M. White, C. P. Looney, E. S. Drexler, and A. J. Slifka, “Development of a Model for Hydrogen-Assisted Fatigue Crack Growth of Pipeline Steel1,” *Journal of Pressure Vessel Technology, Transactions of the ASME*, vol. 140, no. 2, Apr. 2018, doi: 10.1115/1.4038824.
- [41] R. P. Wei and G. W. Simmons, “Surface Reactions and Fatigue Crack Growth,” Aug. 1981.
- [42] J. P. Thomas and R. P. Wei, “Corrosion fatigue crack growth of steels in aqueous solutions I: Experimental results and modeling the effects of frequency and temperature,” 1992.
- [43] J. M. Barsom, “Corrosion-Fatigue Crack Propagation Below KISCC,” *Eng Fract Mech*, vol. 3, pp. 15–25, 1971.
- [44] H. G. Nelson and D. P. Williams, “Quantitative Observations of Hydrogen-Induced, Slow Crack Growth in a Low Alloy Steel,” Moffett Field, California, 1973.
- [45] X. Xing *et al.*, “Quantification of the temperature threshold of hydrogen embrittlement in X90 pipeline steel,” *Materials Science and Engineering: A*, vol. 800, Jan. 2021, doi: 10.1016/j.msea.2020.140118.
- [46] X. Xing, J. Zhou, S. Zhang, H. Zhang, Z. Li, and Z. Li, “Quantification of temperature dependence of hydrogen embrittlement in pipeline steel,” *Materials*, vol. 12, no. 4, Feb. 2019, doi: 10.3390/ma12040585.

- [47] G. Álvarez, L. B. Peral, C. Rodríguez, T. E. García, and F. J. Belzunce, “Hydrogen embrittlement of structural steels: Effect of the displacement rate on the fracture toughness of high-pressure hydrogen pre-charged samples,” *Int J Hydrogen Energy*, vol. 44, no. 29, pp. 15634–15643, Jun. 2019, doi: 10.1016/j.ijhydene.2019.03.279.
- [48] M. Eichinger, J. Pengg, S. Raab, and G. Mori, “On the hydrogen uptake of line pipe steels L80 and P110 under gaseous hydrogen charging up to 1000 bar and 200 °C,” *Int J Hydrogen Energy*, vol. 50, pp. 388–399, Jan. 2024, doi: 10.1016/j.ijhydene.2023.11.144.
- [49] J. Ronevich, M. Agnani, and C. San Marchi, “Consistency of fatigue crack growth behavior of pipeline and low-alloy pressure vessel steels in gaseous hydrogen,” *Int J Hydrogen Energy*, 2024, doi: 10.1016/j.ijhydene.2024.06.287.
- [50] F. D. León-Cázares, M. Agnani, J. Ronevich, and C. San Marchi, “Effects of hydrogen partial pressure on crack initiation and growth rate in vintage X52 steel,” *Int J Hydrogen Energy*, 2024, doi: 10.1016/j.ijhydene.2024.02.292.
- [51] L. E. Faucon, T. Boot, T. Riemslag, S. P. Scott, P. Liu, and V. Popovich, “Hydrogen-Accelerated Fatigue of API X60 Pipeline Steel and Its Weld,” *Metals (Basel)*, vol. 13, no. 3, Mar. 2023, doi: 10.3390/met13030563.
- [52] T. An, H. Peng, P. Bai, S. Zheng, X. Wen, and L. Zhang, “Influence of hydrogen pressure on fatigue properties of X80 pipeline steel,” *Int J Hydrogen Energy*, vol. 42, no. 23, pp. 15669–15678, Jun. 2017, doi: 10.1016/j.ijhydene.2017.05.047.
- [53] J. A. Ronevich, B. P. Somerday, and C. W. San Marchi, “Effects of microstructure banding on hydrogen assisted fatigue crack growth in X65 pipeline steels,” *Int J Fatigue*, vol. 82, pp. 497–504, Jan. 2016, doi: 10.1016/j.ijfatigue.2015.09.004.
- [54] A. J. Slifka *et al.*, “Fatigue crack growth of two pipeline steels in a pressurized hydrogen environment,” *Corros Sci*, vol. 78, pp. 313–321, Jan. 2014, doi: 10.1016/j.corsci.2013.10.014.
- [55] J. A. Ronevich, B. P. Somerday, and Z. Feng, “Hydrogen accelerated fatigue crack growth of friction stir welded X52 steel pipe,” *Int J Hydrogen Energy*, vol. 42, no. 7, pp. 4259–4268, Feb. 2017, doi: 10.1016/j.ijhydene.2016.10.153.
- [56] H. Matsunaga, O. Takakuwa, J. Yamabe, and S. Matsuoka, “Hydrogen-enhanced fatigue crack growth in steels and its frequency dependence,” *Philosophical Transactions of the Royal Society A: Mathematical, Physical and Engineering Sciences*, vol. 375, no. 2098, Jul. 2017, doi: 10.1098/rsta.2016.0412.
- [57] A. Zafra *et al.*, “Hydrogen-assisted fatigue crack growth: Pre-charging vs in-situ testing in gaseous environments,” *Materials Science and Engineering: A*, vol. 871, Apr. 2023, doi: 10.1016/j.msea.2023.144885.
- [58] S. Matsuoka, O. Takakuwa, S. Okazaki, M. Yoshikawa, J. Yamabe, and H. Matsunaga, “Peculiar temperature dependence of hydrogen-enhanced fatigue crack growth of low-carbon steel in gaseous hydrogen,” *Scr Mater*, vol. 154, pp. 101–105, Sep. 2018, doi: 10.1016/j.scriptamat.2018.05.035.
- [59] T. Matsuo, S. Matsuoka, and Y. Murakami, “Fatigue Crack Growth Properties of Quenched and Tempered Cr-Mo Steel in 0.7 MPa Hydrogen Gas”.

- [60] *E 647-08 Standard Test Method for Measurement of Fatigue Crack Growth Rate*. United States: ASTM International. [Online]. Available: www.astm.org,
- [61] A. Laureys, R. Depraetere, M. Cauwels, T. Depover, S. Hertelé, and K. Verbeken, "Use of existing steel pipeline infrastructure for gaseous hydrogen storage and transport: A review of factors affecting hydrogen induced degradation," May 01, 2022, *Elsevier B.V.* doi: 10.1016/j.jngse.2022.104534.
- [62] Y. S. Chen *et al.*, "Hydrogen trapping and embrittlement in metals – A review," *Int J Hydrogen Energy*, 2024, doi: 10.1016/j.ijhydene.2024.04.076.
- [63] R. O. Ritchie and Y. Murakami, "Effects of hydrogen on fatigue-crack propagation in steels," in *Gaseous HE of materials in energy technologies*, Woodhead Publishing Limited, 2012, ch. 11.
- [64] E. Amsterdam, J. W. E. Wiegman, M. Nawijn, and J. T. M. De Hosson, "The effect of crack length and maximum stress on the fatigue crack growth rates of engineering alloys," *Int J Fatigue*, vol. 161, Aug. 2022, doi: 10.1016/j.ijfatigue.2022.106919.
- [65] E. S. Drexler *et al.*, "Fatigue testing of pipeline welds and heat-affected zones in pressurized hydrogen gas," *J Res Natl Inst Stand Technol*, vol. 124, Apr. 2019, doi: 10.6028/jres.124.008.
- [66] J. A. Ronevich, C. R. D'Elia, and M. R. Hill, "Fatigue crack growth rates of X100 steel welds in high pressure hydrogen gas considering residual stress effects," *Eng Fract Mech*, vol. 194, pp. 42–51, May 2018, doi: 10.1016/j.engfracmech.2018.02.030.
- [67] A. Saxena and K. Nibur, "Fatigue Crack Growth Behaviour of High Strength Ferritic Steels in High Pressure Hydrogen," in *MATEC Web of Conferences*, EDP Sciences, May 2018. doi: 10.1051/mateconf/201816503008.
- [68] T. J. Marrow, P. J. Cotterill, and J. E. King, "Temperature Effects on the Mechanism of Time Dependent Hydrogen Assisted Fatigue Crack Propagation in Steels," *Acta metall, mater*, vol. 40, no. 8, pp. 2059–2068, 1992.
- [69] J. P. Petti and R. H. Dodds, "Ductile tearing and discrete void effects on cleavage fracture under small-scale yielding conditions," *Int J Solids Struct*, vol. 42, no. 13, pp. 3655–3676, Jun. 2005, doi: 10.1016/j.ijsolstr.2004.11.015.
- [70] Y. Murakami and S. Matsuoka, "Effect of hydrogen on fatigue crack growth of metals," *Eng Fract Mech*, vol. 77, no. 11, pp. 1926–1940, Jul. 2010, doi: 10.1016/j.engfracmech.2010.04.012.
- [71] W. Gerberich, "Modeling hydrogen induced damage mechanisms in metals," in *Gaseous Hydrogen Embrittlement of Materials in Energy Technologies: Mechanisms, Modelling and Future Developments*, Woodhead Publishing Limited, 2012, ch. 8, pp. 209–246. doi: 10.1533/9780857095374.2.209.
- [72] S. Wu, Brian C, and Y. Mai, "On the relationship between crack tip opening displacement at the initiation of a ductile tear in low carbon steel, hydrostatic stress, and void growth," *Int J Fract*, vol. 51, pp. 207–218, 1991.
- [73] J. Li, F. Guo, Z. Li, J. Wang, and M. Yan, "Influence of Sizes of Inclusions and Voids on Fracture Toughness of Ultra-High Strength Steel AerMetLOO," in *Sino-Swedish Structural Materials Symposium*, 2007.

- [74] J. R. Rice and D. A. Tracey, "On the Ductile Enlargement of Voids in Triaxial Stress Fields," *J. Mech. Phys. Solids*, vol. 17, pp. 201–217, 1969.
- [75] T. H. Courtney, *Mechanical Behavior of Materials*, Second. Waveland Press, 2000.
- [76] S. Taketomi, R. Matsumoto, and N. Miyazaki, "Atomistic study of the competitive relationship between edge dislocation motion and hydrogen diffusion in alpha iron," *J Mater Res*, vol. 26, no. 10, pp. 1269–1278, May 2011, doi: 10.1557/jmr.2011.106.
- [77] Y. Murakami, T. Kanezaki, and Y. Mine, "Hydrogen Effect against Hydrogen Embrittlement," *Metall Mater Trans A Phys Metall Mater Sci*, vol. 41, no. 10, pp. 2548–2562, Oct. 2010, doi: 10.1007/s11661-010-0275-6.
- [78] Y. Takahashi, J. Sakamoto, M. Tanaka, K. Higashida, and H. Noguchi, "Effect of hydrogen on dislocation structures around a mixed-mode fatigue crack tip in a single-crystalline iron-silicon alloy," *Scr Mater*, vol. 64, no. 8, pp. 721–724, Apr. 2011, doi: 10.1016/j.scriptamat.2010.12.032.
- [79] T. J. Marrow, C. A. Hipsley, and J. E. King, "Effect of Mean Stress on Hydrogen Assisted Fatigue Crack Propagation in Duplex Stainless Steel," *Acta metall, mater*, vol. 39, no. 6, pp. 1367–1376, 1991.
- [80] H. P. Kyriakopoulou *et al.*, "Investigation of hydrogen embrittlement susceptibility and fracture toughness drop after in situ hydrogen cathodic charging for an X65 pipeline steel," *Micromachines (Basel)*, vol. 11, no. 4, Apr. 2020, doi: 10.3390/M11040430.
- [81] A. A. Wells, "Crack Opening Displacements from Elastic-Plastic Analyses of Externally Notched Tension Bars," *Eng Fract Mech*, vol. 1, pp. 399–410, 1969.
- [82] E. Sey and Z. N. Farhat, "Evaluating the Effect of Hydrogen on the Tensile Properties of Cold-Finished Mild Steel," *Crystals (Basel)*, vol. 14, no. 6, Jun. 2024, doi: 10.3390/cryst14060529.
- [83] J. Qu *et al.*, "Hydrogen-assisted crack growth in the heat-affected zone of X80 steels during in situ hydrogen charging," *Materials*, vol. 12, no. 16, Aug. 2019, doi: 10.3390/ma12162575.